Enhancing the Biodistribution and Physicochemical Properties of Gold Nanoparticles by Modifying their Surface Characteristics

Doctoral Dissertation
Doctoral Program in Electrical, Electronics and Communications Engineering
(34th Cycle)

Enhancing the Biodistribution and Physicochemical Properties of Gold Nanoparticles by Modifying their Surface Characteristics

By

Rossana Terracciano

Supervisor(s):
Prof. Danilo Demarchi
Dr. Carly S. Filgueira

Doctoral Examination Committee:
Prof. Paolo Decuzzi, Istituto Italiano di Tecnologia
Prof. Bruna Corradetti, Baylor College of Medicine
Prof. Gabriella Olmo, Politecnico di Torino
Prof. Valentina Cauda, Politecnico di Torino
Prof. Gianni Ciofani, Istituto Italiano di Tecnologia

Politecnico di Torino
2022

Declaration

I hereby declare that the contents and organization of this dissertation constitute my own original work and does not compromise in any way the rights of third parties, including those relating to the security of personal data.

Rossana Terracciano

2022

* This dissertation is presented in partial fulfillment of the requirements for **Ph.D. degree** in the Graduate School of Politecnico di Torino (ScuDo).

This study, this thesis, this research is sincerely dedicated to my family, my friends, and people who still believe in science.

Acknowledgment

My deepest gratitude to my mentor, Prof. Danilo Demarchi, for all the great opportunities given to me in these past years together, for his support in any situation, and for being the most humane and thoughtful professor I have ever known. I would equally thank Dr. Carly S. Filgueira for mentoring me during my research period abroad, helping me grow both professionally and personally, and for guiding me through difficult choices. Their enthusiasm for science, critical eye, and wise advice have helped me to develop the essential skills of a successful researcher. With a truly humble heart, I will always be grateful for the trust placed in me from you both.

I would like to thank the MiNES team members in Torino for teaching me what teamwork truly means, inside and outside the lab. Thank you, Sangi, for introducing me to the PhD life and always treating me as a peer even though you were much more experienced. Thank you, Fabio, for starting this journey with me: PhD life is much easier with a labmate like you! Thank you, Paolo, for your kindness and your technical advice: you are truly the cleverest person I know. Thank you, Umberto, Irene, Yuri, Andrea Monga, and all the VLSI members for all the experiences shared together. I've never felt any difference in working in a male-exclusive team. I hope all women can say the same these days.

As well, I would like to thank all the amazing members of the Houston Methodist Research Institute (HMRI) and the Houston Methodist Hospital (HMH)

for their support and help during my research period abroad in Houston, TX. I would especially acknowledge the help and the support given by: Dr. Jianhua (James) Gu, HMRI, director of the SEM and AFM microscopy core; Dr. Xukui Wang and the Houston Methodist Research Institute Translational Imaging PreClinical Imaging (Small Animal) Core; the Comparative Medicine Program at Houston Methodist Research Institute (HMRI) for their support during the in vivo experiments; the staff of the MRI Core at the HMRI Translational Imaging Center, including Dr. Xiaowei Zou from Siemens Medical Solutions for advice on use of UHF MR; Mr. Daryl Schulz from HMRI Pre-Clinical Catheterization Laboratory; Matthew Vasquez and the Microscopy Core; the HMRI Research Pathology Core; Prof. Jason H. Hafner from Rice University; Dr. Prashant Dogra from Mathematics in Medicine Program, Houston Methodist Research Institute; Dr. Alessandro Grattoni and his amazing lab members, and all the members of the Department of Nanomedicine, HMRI. A special acknowledgment goes to the financial sponsors of the research projects included in this thesis: Golfers Against Cancer, Simmons Foundation, Houston Methodist Research Institute, Houston Methodist's Department of Orthopedics Pilot Project Initiative, Rice University, National Science Foundation, the George and Angelina Kostas Research Center for Cardiovascular Medicine, the Cockrell Foundation, and the National Institutes of Health.

This experience significantly enriched my knowledge and allowed me to make new friends in a new country. I thank my fellow lab-mates for the support, for the stimulating discussions, and all the excitement we have had in the last three years. Thank you, Yareli and Amber Lee for being the best co-workers I could ever want and always supporting and cheering me, even in my deepest-blue days. I'll never forget everything you did for me, and I'm sure our friendship will last forever. I also want to thank my Houstonian family: Mery, Simo, Fer, and Nico. We literally became a family, spending together holidays and quarantines, and you have been

everything to me in historically strange years of uncertainty and fear. Just thank you, guys.

Lastly, I would specially thank my parents, my brother, and my family all for all the sacrifices they did for helping me and supporting my studies, and for always believing in my capabilities. And, of course, thank you to my beloved Simone for his patience and encouragement, and for never giving up on me.

Thank y'all

Abstract

This work investigates new frontiers in Nanomedicine to overcome tumor heterogeneity by developing traceable theranostic platforms that can distribute site-specifically in areas of interest. This study was made possible due to the close collaboration between Politecnico di Torino, Turin, Italy, and the Department of Nanomedicine at the Houston Methodist Research Institute, Houston, Texas.

To date, heterogeneous distribution of drugs or treatment modalities within the tumor mass has been a crucial limiting factor for a vast range of theranostic applications. Understanding the interactions between a nanomaterial and the tumor microenvironment would help to overcome the challenges associated with poor distribution due to tumor heterogeneity as well as the clinical translation of nanotheranostic materials. The delivery of small molecules and anticancer agents to specific regions within solid tumors is limited by penetration depth and poor spatial drug distribution, hindering efficacy. Another major issue is biofouling, the unwanted adsorption of cells, proteins, or intracellular and extracellular bio-molecules that can spontaneously occur on metal nano-complexes. This phenomenon leads to a protein corona and destabilizes a colloidal solution, resulting in undesired macrophage-driven clearance, and consequently causing failed delivery of a targeted drug cargo.

In this thesis, surface passivation of metal nanomaterials, such as Gold Nanoparticles (GNPs), with various chemical functionalities results in observed behavioral differences in cellular uptake and intratumoral distribution. We show that when the nanoparticle surface chemistry is altered, dramatic changes occur in their penetration and localization in heterogenous solid tumors. Gold nanoparticles were synthesized, passivated with different molecules, and administered in vitro and in in vivo models of Non-Small Cells Lung Cancer. The main result and contribution of this work is that GNP surface passivation affects nanoparticle transport behavior within the cellular and tumor microenvironment. Controlled

delivery of GNPs passivated with different surface chemistries resulted in differences in intratumoral distribution as well as zonal delivery within the tumor. These results are useful for directing anticancer therapies to regions of biomarker overexpression.

We found changes in the surface functionalization of gold nanomaterials can alter their cytotoxicity or improve their biocompatibility. For instance, gold nanorods (GNRs), nanoparticles with tunable light absorption properties, have a controversial safety profile, limiting their clinical translation due to surfactant stabilization during synthesis. We explored changing the charge of the surfactant used to stabilize the GNRs, and the resulting effects on lung and cervical cancer cell viability. Altering the GNR surface charge using an anionic surfactant improved cell survival and reduced cytotoxicity when compared to cationic surfactants. Changing the surfactant net charge resulted in significant dose-dependent as well as time-dependent effects of nanorod treatment on cell viability.

Finally, plasmonic silica-gold core-shell nanoparticles, known as gold nanoshells (GNS) were investigated for their photothermal properties. We tested the ability of GNS to generate heat and create ablation lesions due to light excitation. GNS can be synthesized to exhibit strong optical resonances across the electromagnetic spectrum depending on their core-to-shell ratio. This optical absorption can be tuned to longer wavelengths, such as the near infrared. Importantly, as the particles are gold-coated, they are resistant to oxidation and remain biocompatible, allowing for their use clinically. Here, we show that light exposure of near-infrared sensitive (NIRS) gold nanoshells to their resonant wavelength (808 nm) reveals local heating to temperatures greater than 50 ºC, inducing cell death. Further, we show that under continuous exposure to light for over 1000 seconds, temperatures between 50-60 ºC can be maintained without continued rise. These results indicate the possibility to create photothermal ablation lesions via nanoparticle-induced heating in deep regions of target tissue.

Overall, the work presented in this thesis demonstrates that modifying the GNP surface chemistry changes their physicochemical properties, which can be exploited to enhance nanoparticle biodistribution in heterogeneous tissues, thereby making GNPs versatile and valuable tools for biomedical applications.

Keywords: *Gold Nanoparticles;Non-Small Cell Lung Cancer; Peritumoral; Cytotoxicity; Biodistribution; In Vivo; In Vitro; Theranostics; Computed Tomography Imaging; Surface Passivation; Inductively Coupled Plasma Optical Emission Spectrometry*

Contents

List of Figures

Chapter 1

Introduction to Gold Nanoparticles and the Role of their Physicochemical Properties

1.1 Introduction

This chapter aims to illustrate the research work conducted at the Houston Methodist Research Institute during my Ph.D. and to underline the logic of the research presented in this thesis. Dr. Filgueira's research laboratory studies nanotechnology-based platforms for long-term sustained release of therapies for both local and body-wide applications to prevent and treat chronic diseases. By engineering nanomaterials, and in particular nanoparticles, the obstacles of conventional therapeutic intervention can be surpassed through sustained release, targeted drug therapy, and local delivery to a specific site of action. In fact, local delivery of these nanoparticles improves the bioavailability of the therapeutic and reduces off-target adverse effects without altering their ability to act as diagnostic tools.

The scope of this Ph.D. thesis is to demonstrate that controlling the surface properties at the nanoscale can significantly improve upon their use as diagnostic materials as well as enhance treatment outcomes. To achieve this goal, we exploited the surface proprieties of metal nanoparticles, in particular colloidal gold in different sizes and shapes at the nanoscale. GNPs were chosen over other metals mainly for three reasons:

(i) the high chemical and physical stability, indicating the intrinsic biocompatibility of gold nanostructures
(ii) the multitude of optical properties related to surface plasmons
(iii) the ease of surface functionalization of GNPs with organic and biological molecules

In fact, GNPs have been demonstrated to be biocompatible and have unique optical properties, since they can generate a plasmonic effect when incident light interacts with their free electrons. Modifying their size and shape, researchers can obtain a unique surface plasmon resonance which can be useful in applications for cancer imaging, spectroscopic detection, and photothermal therapy.

Another important advantage of using GNPs is related to their ability to absorb X-rays. In fact, colloidal gold has been demonstrated to act as a contrast agent in experimental setups and encouraging results suggest that their use in the field of clinical diagnostics can overcome numerous obstacles associated with traditional iodine-based contrast agents. For instance, in clinical oncology, they allow for visualization of the tumor microenvironment using morphological imaging

techniques, such as computed tomography. Therefore, due to their high X-ray attenuation values, tissue structures, vasculature, and biodistribution can be better resolved, improving our ability diagnose as well as treat individuals.

In addition, modifying the physico-chemical properties of GNPs allows for improvements in their biocompatibility and uptake efficiency. The GNP surface can be functionalized through electrostatic and covalent interactions, generating different responses when placed in contact with malignant cells. In this thesis, modifications in surface passivation were exploited to improve nanoparticle biodistribution in vivo in tissues with high spatial heterogeneity, such as solid tumors. The main contribution to the scientific research is that in engineering the nanoparticle surface chemistry, we were able to direct particles toward specific zones of malignant tissues, obtaining minimal systemic exposure via intratumoral injections performed with an injection pump.

1.2 Physicochemical Properties of Gold Nanoparticles

In the context of medicine and biology, nanotechnology is described as the engineering of functional systems at the molecular scale, including materials and devices with a structure and function from nanometers (10^{-9} m) to micrometers (10^{-6} m) [1]. Nowadays, there is an increasing interest in nanoparticles fabricated from noble metals, such as silver [2], copper [3], or titanium [4]. However, colloidal gold is the most studied and used inorganic nanomaterial, mostly due to its unique physicochemical characteristics, including simple preparation, controllable size, biocompatibility, good acceptance of surface modifications or bioconjugation, and specific surface plasmon resonance (SPR) [5].

In particular, the SPR effect is an important physical feature of GNPs which occurs when the frequency of the oscillation of free electrons at the surface of the nanoparticle resonates with the frequency of the incoming light radiation, resulting in a plasmon band. These easily polarizable conduction electrons generate preferential interaction between GNPs with electromagnetic fields with the consequent generation of nonlinear optical phenomena. In fact, compared to other organic and inorganic chromophores, GNP diameters >2 nm produce a larger extinction cross-section, with the possibility to reach 100% light-to-heat conversion efficiency, as well as high photostability and the ability to amplify the electromagnetic field at nanometric distance from the metal surface [6].

The extinction coefficients of the SPR bands are extremely high (10^{11} M^{-1} cm^{-1}), and they can be several orders of magnitude greater than those of common organic dyes [7]. Depending on size and shape, type of solvent, surface ligand, core charge, temperature, and the proximity of other nanoparticles, GNPs offer absorption and scattering effects, manipulating the electron charge density on the particle surface (Figure 1.1). In the case of spherical GNPs with diameter sizes <50 nm, the SPR peak absorbance appears around 500–550 nm, and this characteristic contributes to their red color at macroscopic level [8]. For anisotropic nanoparticles, like gold nanorods (GNRs), two plasmon bands are observed due to the electron oscillation along the length (longitudinal plasmon band) and the width (transverse plasmon band), exhibiting plasmon bands with maxima ranging from 500 to 1600 nm, depending on the length/width ratio [9].

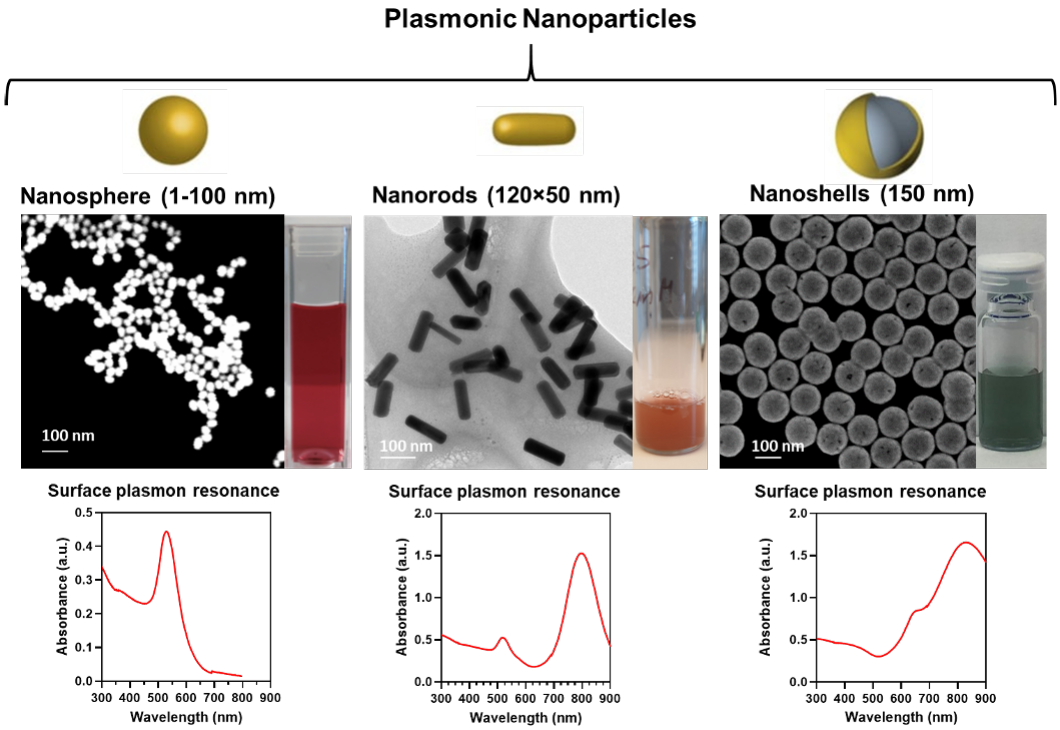

Figure 1.1 Plasmonic gold-based nanoparticles investigated in this thesis. Gold nanospheres in the diameter of ~40 nm, with surface plasmon resonance (SPR) peak at 530 nm; gold nanorods with ~120 nm in length and ~50 nm in width, with surface plasmon resonance (SPR) peak at 800 nm; gold nanoshells in the diameter of ~150 nm, with surface plasmon resonance (SPR) peak >800 nm. Microscopic pictures of the particles here presented are captured with scanning electron microscopy and transmission electron microscopy. For comparison, optical photos of each type of nanoparticle are reported, showing the color change in the visible light depending on their size and shape.

When plasmons occur in particles with sizes much smaller than photon wavelength, such in the case of GNPs (wavelength 500 nm >> diameter 50 nm) or GNRs (wavelength 500-1600 nm>>diameter 50-120 nm), they are non-propagating excitations classified as localized surface plasmons (LSPs) because the resulting plasmon oscillation is distributed over the whole particle volume [10]. LSPs can be changed by alterations in the refractive index around the particle such as by making chemical modifications to the GNP surface, through conjugation with thiolated ligands or adsorption of ions and small molecules. Therefore, nanoparticle surface modifications can generate a shift in the LSPs, (such as a red-shift or change in absorbance to a longer wavelength due to an increase in the refractive index). Changes in the LSP can be used to confirm successful surface modifications and for monitoring the stability of colloidal gold over time.

In addition, light absorption can be used in photothermal therapy, which is a non-invasive method for treating cancer. Here, light is absorbed by the GNPs and this leads to enhancement of heat, which can be exploited to destroy malignant or abnormal cells. After the release of free electrons from the GNP plasmon band by laser excitation, the heat generated in the crystalline network can be transferred to the environment by electron-electron scattering, electron-phonon coupling, and phonon-phonon reaction [11]. Lasers in two treatment windows ranging from 650 to 940 nm (NIR) and from 1000 to 1350 nm (IR) have been demonstrated to generate the least absorption in peripheral tissues, while generating less severe side effects [12]. Finally, light scattering can be used in imaging techniques such as computed tomography (CT). This property will be discussed more in details in the following section.

1.3 X-ray absorption properties of GNP and their use in biomedical imaging

Imaging techniques for noninvasive cell tracking are becoming crucial for elucidating the mechanisms of the distribution, migration, and kinetics of nanomaterials in medical imaging [13]. In fact, imaging techniques may allow for real-time monitoring of the location and concentration of particles inside the body, enhancing clinical outcomes [14]. In this regard, advanced techniques have been

investigated in the field of nanomedicine, combining clinical therapies and diagnostic imaging in a single treatment to guide personalized medicine [15].

In X-ray based imaging, contrast is based on the differences in the X-ray absorption of distinct tissues, meaning that small absorption differences among materials results in weak contrast, which produces low-quality images. The image intensity generated by X-ray attenuation obeys the Beer-Lambert law: $I = I_0 e^{-\mu x}$, where I is the transmitted X-ray intensity, I_0 is the incident intensity, x is the thickness of the matter, and μ is the mass attenuation coefficient, which increases when the atomic number increases and decreases when the X-ray energy source intensifies [16]. Therefore, a contrast media with a high atomic number generates superior X-ray attenuation when compared to other elements, producing useful images for diagnostics.

To intensify X-ray contrast, and thus increase image resolution, gas phase contrast agents or liquefied iodinated derivatives are normally used in standard clinical practices. However, standard contrast agents present several limitations, including poor contrast in over-weight patients, the need for characterization in several cases, and high osmolarity, which generates occasional renal or pre-renal toxicity [17]. Furthermore, the instantaneous distribution and rapid clearance of contrast agents allow very short time windows for CT imaging, especially for vascular applications [18].

GNPs have both a higher atomic number as well as high X-ray absorption, lending them as potential candidates to enhance imaging and delineate areas of interest for clinicians. GNPs can be used in contrast-enhanced computed tomography (CT) applications and importantly, have a higher X-ray absorption coefficient compared to standard iodinated contrast agents. In fact, at 100 keV, the X-ray absorption efficiency of GNPs (5.16 cm^2/g) is three times higher than that of iodinated agents (1.94 cm^2/g), as well as much higher than that of bones (0.186 cm^2/g) and soft tissues (0.169 cm^2/g) [19]. In addition, compared with low-molecular-weight iodine solutions, GNPs remain longer in circulation, prolonging imaging time. Therefore, GNP contrast media improves visualization, and GNPs have demonstrated to be effective in multifunctional applications for diagnostics and therapies, especially for combinatorial or multimodal cancer treatment [20], [21].

Recent progress towards nanomedicine-based CT imaging has been made by Ashton et al. using GNPs as a contrast agent for targeting the epidermal growth

factor receptor, which is expressed on the cell surface of most lung adenocarcinomas [22]. CT imaging performance was evaluated in vivo in mice subcutaneous tumors, showing high tumor accumulation and suggesting a possibility to better differentiate malignant lung cancers from benign lesions. Early diagnosis of hepatocellular carcinoma was achieved by Rand et al. using surface-modified gold nanoparticles in combination with X-ray imaging, distinguishing cells containing GNPs from cells without gold in X-ray scatter images and detecting in vivo tumors smaller than a few millimeters in size [23]. Similarly, GNPs approximately 30 nm in diameter [24] or smaller [25] have been injected intravenously and detected by X-ray imaging in vivo in computed tomography, specifically for hepatoma in the liver, generating visible images in both cases.

It has been shown that GNP size does not significantly affect their contrast generation with CT for sizes ranging from 4 to 60 nm [26]. Further when comparing spherical GNPs with GNRs, no significant variation in attenuation depending on particle size was observed, demonstrating that contrast enhancement is less dependent on size than on shape of the nanoparticles [27]. However, particle size affects biodistribution and organ accumulation: 15 nm or smaller particles have long blood circulation times, while larger GNP (>15 nm) were shown to accumulate in the liver and spleen more rapidly [28].

Non-invasive imaging techniques, especially those involving contrast-enhanced CT, enable a deep understanding of the internalization mechanisms of GNPs into tumor cells and an assessment of specific receptor binding. In this regard, Shamalov et al. longitudinally CT-tracked the migration of intravenously injected natural killer-cells labeled with GNPs, observing a cluster accumulation at the tumor site for up to 72 h [29]. Yu et al. reported an innovative labeling strategy based on temperature-responsive GNPs, using CT imaging to track transplanted human mesenchymal stem cells for 10 days and obtaining high cell labeling efficiency and extended intracellular retention duration [30].

Therefore, due to their strong X-ray attenuation, GNPs may offer improvements in the quality of clinical care and treatments, including predictive, preventive, and personalized medicine. However, it is important to assess their potential clinical implementation by studying their long-term biodistribution, intrabody stability, dose toxicity, and clearance while addressing concerns related to their excretion profile. In the next several chapters of this thesis, an effective protocol to quantify the biodistribution of GNPs within cells and tissue in pre-

clinical research will be presented and the usage of GNPs in different applications will be discussed.

1.4 Importance of Surface Functionalization of Gold Nanoparticles

Chemical synthesis of GNPs generally involves capping agents such as sodium citrate, ascorbic acid, sodium borohydride or sodium hydride to provide stability in a pH-neutral solution through electrostatic repulsion and to overcome van der Waals forces to avoid agglomeration in solution [31]. However, persistent problems related with aggregation upon pH change and nonspecific adsorption of serum proteins to the GNP surface have been reported [32]. This phenomenon can lead to conformational changes of serum proteins and enzymes, resulting in toxicity [33]. Indeed, a direct interaction between the GNP surface with cells can damage the integrity of membrane structure, which in some cases results in leakages. Another possible effect related to particle stability is their rapid removal by the reticuloendothelial system once they are introduced into the body [34]. In addition, GNP surface charge and surface hydrophobicity both play an important role in cytotoxicity, DNA damage, and ROS production, with potential toxic consequences dictating immune responses [35]. Therefore, for their use in clinical applications, long-term storage of GNPs in solution requires a high degree of stability to prevent their agglomeration, which in turn, will increase their blood circulation time.

To address some of these challenges, the GNP surface can be functionalized with a diverse variety of organic and inorganic molecules. Surface functionalization of GNPs can be achieved via non-covalent and covalent bonds. Non-covalent interactions, such as hydrogen bonding, electrostatic, or van der Waals forces, are relatively simple to achieve and can be used in different applications [36]. Electrostatic interactions occur when an equal number of oppositely charged ions present in the liquid dispersion media border the GNP surface, generating an overall electro-neutral double layer. This electrostatic repulsion prevents the agglomeration of nanoparticles in the solution phase and can be further modified by controlling significant variables, such as pH, concentration, and temperature. Steric stabilization is obtained using stabilizing agents, such as hydroxyl groups, surfactants, and different oligomers/polymers, which obstruct the free GNP movement during synthesis reactions, generating a protective layer at the outer surface of the nanoparticles. Finally, surface stabilization can be also manipulated

using polyelectrolytes as a polymeric surfactant, which generates an electric double layer around the particles with their end chains extended and polar head group near the particle surface [37]. Although non-covalent bonds are easier to maintain in colloidal media, pH and ionic strength affect the stabilization of nanoparticles as well as their potential for agglomeration and oxidation processes [38].

Multiple linker molecules can be used to form covalent bonds between ligands and the GNP surface, which provide functional groups (ex: −COO–, −NH3+, −CHO, and so on) or charges that can be exploited for bioconjugation or ligand exchange [39]. For ligand exchange, the new ligand molecule must have a stronger affinity to the inorganic core in order to quickly and effectively replace the original surfactant molecule. For instance, functionalization of citrate-capped GNPs is relatively easy, due to the weakness of the Au–citrate interaction. This interaction is electrostatic in nature and can be substituted with stronger ligands, such as sulfur-containing ligands, obtaining a direct conjugation to form thiol-protected GNPs [40].

The high affinity of GNPs to bind thiols, amines, and polymers provides a convenient way to introduce reactive functional groups that can be utilized for targeting specific regions of tissue. Antibodies, peptides, aptamers, and carbohydrates, offer means to conjugate therapeutic agents, such as drugs, radionuclides, photosensitizers, siRNA and genes to the nanoparticle for drug delivery applications [41]. In particular, thiol groups demonstrate the highest affinity to noble metal surfaces, such as gold (200 kJ mol^{-1}), creating a strong covalent bond, which better stabilizes the nanoparticles to prevent aggregation at high salt concentrations or acidic pH [42].

Efficacy of the Au–S bond for chemical conjugation to aid in cancer detection and treatment has been tested in vitro with different cancer cell lines. For instance, Gao et al. conjugated GNPs to epidermal growth factor receptor antibodies using thiol ligands, demonstrating the ability to target cancer cells evaluated with dark field microscopy [43]. Zhang et al. utilized the thiol group of glutathione to passivate GNPs for the detection of human cervical carcinoma cells via transmission electron microscopy and confocal laser scanning microscopy [44]. Ye et al. synthesized retinoic acid-poly(ethylene glycol)-thiol gold nanoparticles, which were not only selectively delivered to cervical carcinoma cells but also showed growth inhibition 12 and 24 h after incubation [45]. Furthermore, the use of thiol chemistry to modify GNPs with different therapeutics has been used to demonstrate targeted drug delivery in several in vivo studies. For instance,

doxorubicin-loaded paramagnetic gold nanoparticles were successfully retained throughout the tumor, showing improved therapeutic anticancer activity and low systemic toxicity, compared to that of free doxorubicin in immunogenic murine squamous cancer [46] and in Ehrlich ascites carcinoma [47]. Additionally, paclitaxel-conjugated GNPs were shown to improve circulation times due to their high stability in vivo, targeting and releasing the drug inside tumor cells, while increasing tumor cell killing efficiency in hepatoma solidity cells [48].

Functional groups conjugated on the surface of nanoparticles can affect their circulation time and major excretion route, producing differences in blood kinetics, organ distribution, and elimination. For instance, when injected intravenously in mice, the GNP deposition rate at an organ site after 24h was found to be different, depending on their functional groups, whereby PEG-coated GNPs accumulated in the mesenteric lymph node, kidney, brain, and testis, while COOH-GNPs accumulated in the liver, and NH_2-GNPs in the spleen, lung, and heart [49]. Many other research works have studied the tissue distribution of GNPs after intravenous injection in animal models [50],[51],[52]. However, intravenous injection of nanomedicines presents several drawbacks, such as off-target effects. Therefore, the advantages of local administration of nanotherapeutics over systemic delivery and how surface functionalization can affect the local distribution of nanomaterials will be discussed in the next several chapters of this thesis.

Investigating the effects of surface functionalization will improve our ability to produce stable GNPs in multi-environmental conditions, as well as help determine the optimum surface coverage and stabilizing agent to reduce immunotoxicity [53]. While GNPs are generally shown to be noncytotoxic, further functionalization must be rigorously tested to better improve their long-term safety and stability. Further studies are also needed to understand how GNP biodistribution and pharmacokinetics can be modulated to enhance accumulation in target tissues and organs. The research conducted in this thesis takes into account these considerations and aims to investigate how GNP surface passivation can improve our ability to distribute and retain a nanotherapeutic within a target tissue.

1.5 Thesis outline

The progression of this thesis to evaluate metallic nanoparticles and how their properties can be exploited for biomedical and theranostic applications, which

develops across several steps and chapters. The thesis starts by introducing gold as a nanoparticle substrate and discussing its physical properties as well as chemical properties for surface attachment (Chapter 1). In Chapter 2 we demonstrate gold nanoparticle (GNP) synthesis and characterization and show that spherical GNPs with diameters in the range of 40-50 nm have superior X-ray properties compared to standard iodinate contrast agents and that this property can be utilized for enhanced CT imaging in vivo. The reader will find application of these results in Chapter 3, in which an in vivo investigation of biodistribution and retention of intratumorally (IT) injected GNPs capped with a protein (bovine serum albumin, BSA), known to bind to metal complexes, is reported for study in a murine model of lung cancer.

Additionally, in Chapter 3 we focus attention on how the GNP surface modification with Bovine Serum Albumin results in a more homogeneous and uniform tumoral distribution and how changing the pH of the colloidal solution with surface stabilizing agents can also generate an effect on intratumoral particle distribution (section 3.3). An effective protocol is presented to inject GNPs locally using an injection pump which offers an alternative and more efficient methodology compared to manual intratumoral injection [54].

In Chapter 4, this methodology is investigated in more detail, discovering a zonal diffusion pattern of the particles inside the tumor dependent on the GNP surface properties and functionalization. A mathematical model describing the spatiotemporal dynamics of free and bound GNPs while interacting with the ECM and cancer cells with partial differential equations was developed and validated on experimental data.

Chapter 5 is a natural extension of the results previously obtained, investigating the GNP zonal diffusion pattern in the case of ligand-mediated targeting to tumor cells. GNP were functionalized with hyaluronic acid which binds specific receptors overexpressed on mammalian malignant cells. Ligand-mediated targeting was demonstrated over time, resulting in a significant major escape of unfunctionalized GNPs from the tumor site to other organs (such as the liver) compared to those functionalized with hyaluronan [55].

In Chapter 6 we shift attention to discussion on how particle surface functionalization can affect cytotoxicity, a major problem that has hampered the clinical translation of metallic gold nanorods (GNRs). In fact, gold nanorods (GNRs) present a controversial safety profile because of surfactant stabilization

during their synthesis. Our results suggest that altering the GNR surface charge to negative values using anionic surfactant generates less cytotoxicity than cationic surfactants in in vitro models of lung and cervical cancer [56].

Finally, Chapter 7 will investigate surface functionalized gold nanoshells (GNSs), metallic core-shell nanoparticles with high X-ray absorption and photothermal properties, for their potential use cardiac arrhythmia treatment as a novel means to photothermally ablate myocardial tissue [57].

This thesis ends with a summary chapter, which will focus on the impact of the results generated by this PhD thesis as well as the future challenges that need to be addressed to further advance clinical translation of metallic gold nanoparticles.

Chapter 2

Intratumoral Gold Nanoparticles-Enhanced CT Imaging: An in Vivo Investigation of Biodistribution and Retention

2.1 Introduction

Non-small cell lung cancer (NSCLC) ranks among the most common type of lung cancer, accounting for ~85% of all lung cancer diagnoses, with 5-year cause-specific survival rates ranging from 13% to 32% and local failure rates of 42% to 49% when treated with conventional radiotherapy alone [58]. The engagement to reduce the radiation dose and damage to healthy tissues without losing efficacy in cancer therapy have focused the research on exploiting gold nanoparticle (GNP) properties in enhancing radiation effects via physical, chemical, and biological interactions with ionizing radiation [59]. However, challenges concerning in vivo efficacy still limit the clinical translation of GNP radiosensitizers mainly due to the lack of colloidal stability, clearance, and possible long-term toxicity [60]. Therefore, the ability to predict and determine GNP in vivo biodistribution will provide further information about the preferred uptake pathways for achieving precise dose deposition as well as a better understanding of mechanisms behind radiosensitization [61]. To quantify the biodistribution of GNPs within cells and tissue, several imaging techniques can be employed due to the physical properties of GNPs that allow them to act as imaging agents [62], [63]. This study focuses on Computed Tomography (CT) as an imaging modality to provide insight into the GNP local biodistribution in Lewis Lung Carcinoma (LLC) tumor-bearing mice based on CT attenuation levels. CT is an inexpensive diagnostic imaging system routinely used in practice with a high capability of deeply tissue permeation and density resolution which allows for 3-dimensional (3D) reconstructions of X-ray images. CT contrast agents are commonly administered to improve the contrast among tissues with similar or lower attenuation values by increasing the signal-to-noise ratio without additional radiation doses to the patient. Nevertheless, different drawbacks in the use of iodine-based contrast agents such as renal toxicity, deficiency in the targeting process, and insufficient circulation time as well as amplification in DNA damage during CT scans, restrict their application [64].

Several studies confirm GNPs as excellent contrast agents for CT imaging and multimodalities [28], [65], [66]. So far, CT image-guided cancer treatments using radio-enhancing GNPs has not been thoroughly investigated in preclinical NSCLC models. The main contribution of this study is to give a better understanding of the in vivo IT distribution and retention of citrate-capped and BSA-capped GNPs using CT imaging.

2.2 Experimental

2.2.1 GNPs Synthesis and characterization

Multi-faceted GNPs (Figure 2.1A) are synthesized using an adapted protocol by Turkevich et al. [67] to tune the particle size to a value of approximately 40 nm. Briefly, 1 g of gold chloride ($AuCl_3$, purity > 99.99%) is added to 100 mL of Milli-Q water and filtered through a 0.22 μm nylon filter, and 1 g of citric acid ($C_6H_8O_7$) was dissolved in 100 mL of Milli-Q under stirring.

Respectively, 4.8 mL of the 1% (w/v) citric acid solution and 7 mL of 1% (w/v) gold chloride premade reagents are added to 600 mL of boiling Milli-Q water. The synthesis is complete when the color has changed from black to dark red. The GNPs are characterized with UV-Vis Spectroscopy and electron microscopy (SEM, TEM). Dynamic Light Scattering (DLS) was used to rapidly and qualitatively size the particles and obtain a polydispersity index (PDI). Zeta Potential was also measured (Malvern).

The resulting particles yielded a surface plasmon peak at ~530 nm with a hydrodynamic diameter of 43.89 ± 15.45 nm (Figure 2.1B). The particle diameter extracted from SEM and TEM images is 39.1 ± 15.0 nm, which is in accordance with the value obtained with DLS (< 11% error). The particle solutions yield Z-potentials of -40.0 ± 6.0 mV.

2.2.2 BSA capping and characterization

The GNP surface is then modified by passive absorption of Bovine Serum Albumin (BSA) to increase colloidal stability and biocompatibility. To perform BSA-capping on the GNP surface, lyophilized BSA in a concentration of 2% (w/v) is added to the solution of colloidal gold already prepared and characterized. The mixture is stirred vigorously until complete dissolution of BSA. The absorption of BSA on the particle surface is evaluated by analyzing the UV-Vis spectrum of the solution. A positive passivation of the particles is confirmed by a red-shift in the gold SPR peak at 535 nm and the presence of a BSA absorption peak at 280 nm.

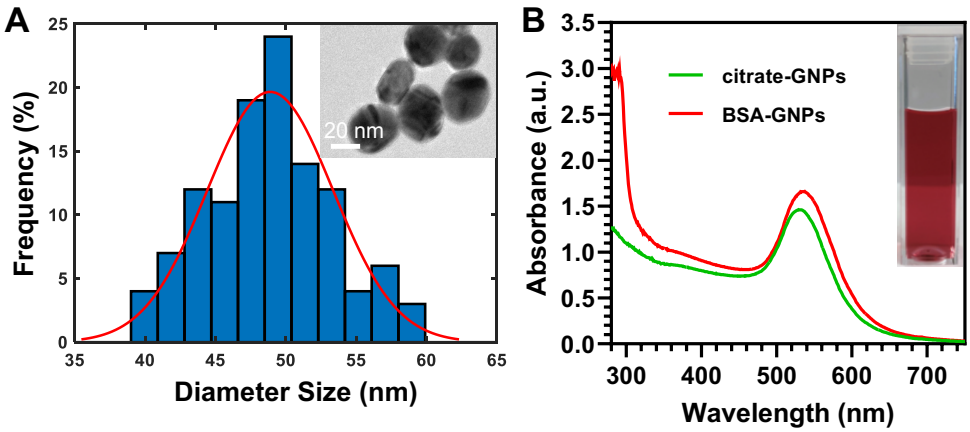

C

	hydrodynamic diameter (nm)	surface zeta-potential (mV)
citrate-GNPs	43.89 ± 15.45	-40.0 ± 6.0
BSA-GNPs	96.40 ± 19.83	2.29 ± 5.29

Figure 2.1 Size distribution (n>100) and TEM image of citrate-GNPs (A). Average particle size: 39.1 ± 15.0 nm. Absorbance spectra of citrate-capped GNPs and BSA-GNPs with absorbance maxima occurring at 530nm and 535nm, respectively (B). A direct comparison between hydrodynamic diameter and surface zeta-potential for the citrate-GNPs and BSA-GNPs.

2.2.3 CT phantom imaging

In order to prepare the samples for clinical CT phantom imaging, GNP solutions in concentrations ranging from 0 to 10mg/mL are aliquoted in 100 µL tubes and scanned with a Siemens Inveon High-Resolution CT to assess the CT contrast properties (Figure 2.2). The phantom experiment was carried out using CT parameters with slice thickness of 105 µm, in plane resolution of 105 µm, tube voltage at 80 kV, tube current at 500 µA, exposure time of 240 ms, and by placing the samples directly on the animal bed.

X-ray attenuation intensity was determined in Hounsfield unit (HU) by processing the digital CT images (DICOM files) using 3DSlicer and selecting a 3D reconstructed region of interest (ROI) for each sample and then recording the mean attenuation value and plotting as a function of gold and/or iodine concentration in mg/mL.

As expected, an increase of CT attenuation occurred when the mass concentration of the GNPs increased. Both citrate-GNPs and BSA-GNPs absorb more X-rays than Omnipaque350 (a standard iodine-based CT contrast agent) as shown in Figure 2.3. The range of CT values for LLC-LUC solid tumor 8 days after cell inoculation is included in the graph for comparison.

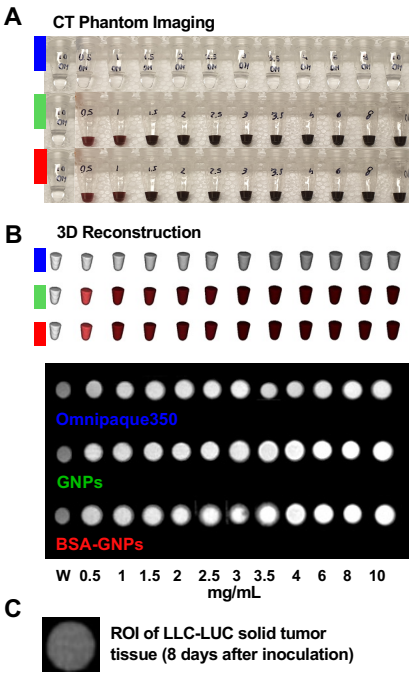

Figure 2.2 CT contrast properties of ~40 nm citrate and BSA-capped GNPs Compared with those of Omnipaque350. Photos of the phantom dilution series from 0 (water) to 10 mg/mL concentrations for Omnipaque350 (blue), citrate-GNPs (green), and 2% (w/v) BSA-capped GNPs (red) (A). Representative 3D volume rendered CT images and sample phantom images from Siemens Inveon High Resolution CT scanner (B). For a better understanding and comparison is reported a ROI of the LLC tumor 8 days after cell inoculation and immediately before GNP injection (C).

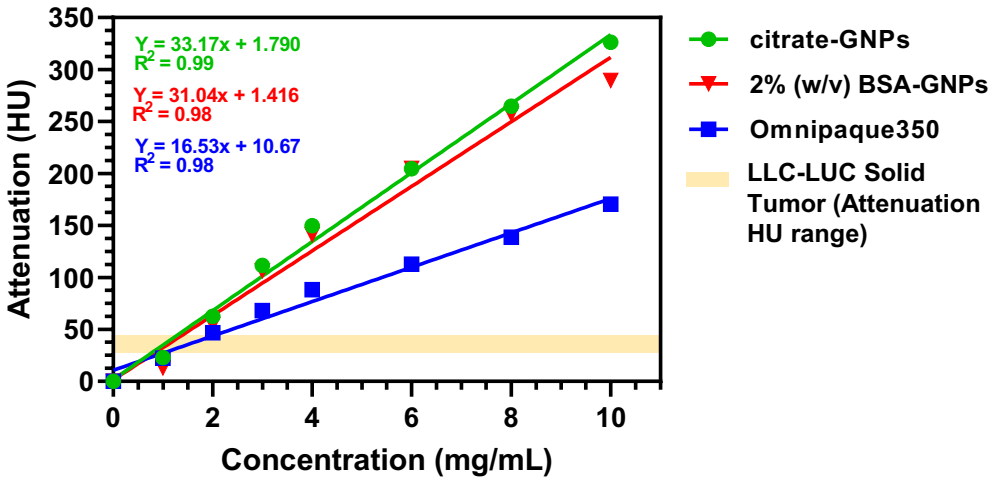

Figure 2.3 X-ray attenuation changes in Hounsfield Units (HU) versus concentration for citrate and BSA-capped GNPs compared with those of Omnipaque350. Data are reported in terms of mean value of the 3D reconstructed voxel attenuations and standard deviations. To trace the thresholds for choosing the optimal concentration to inject, the LLC tumor tissue density range 8 days after cell inoculation and immediately before GNPs injection is reported (yellow range).

2.2.4 In vivo CT imaging

High-resolution CT imaging is then exploited to compare the biodistribution of citrate and BSA-capped GNPs in a LLC murine model of NSCLC. *In vivo* imaging experiments were performed using six-week-old female C57/BL6 mice, purchased from Taconic Bioscence (Rensselaer, NY, USA).

The mice received an injection of $2x10^6$ LLC cells in the right flank subcutaneously once their weight reached an average of 18.4 g. After approximately 10 days post-injection, the volumes of tumor nodules appeared spherical and 100 mm^3 in volume. The mice were anesthetized using isoflurane, and 100 µL of citrate or BSA-capped GNPs were injected IT (3.5 mg/mL of gold). CT images pre-injection were recorded as a baseline for the biodistribution analysis. All the CT imaging was performed using a Siemens Inveon Multi-Modality (MM) System controlled with the Inveon Acquisition Workplace (IAW). In vivo experiment was carried out using CT parameters with slice thickness of 103.25 µm, in plane resolution of 103.25 µm, tube voltage at 80 kV, tube current at 500 µA, and exposure time of 240 ms.

The mice were imaged at different time intervals (day 0 pre-injection, day 0 post-injection, day 3 post-injection, day 6 post-injection, day 9 post-injection, and day 10 post-injection). The CT images were acquired and reconstructed with 3DSlicer software.

2.3 Data Analysis

Figure 2.4 shows the 3D renderings of three significant timepoints during the ten day post-injection time period. Although both citrate and BSA-capped GNPs exhibited excellent biocompatibility and sustained retention post IT injection, the citrate-GNPs were observed to stably cluster *in situ* over the ten days, while the BSA-GNPs were less likely to locally agglomerate within the tumor (Figure 2.4B, Figure 2.4C). Therefore, the BSA helps to facilitate the biodistribution of the GNPs in the tumor area, preventing the formation of clusters.

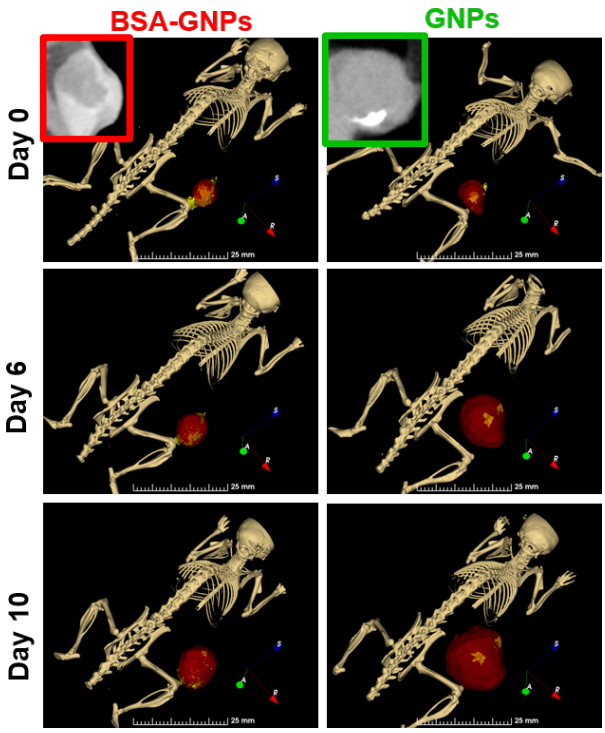

Figure 2.4 Representative 3D volumes rendered CT images at day 0 immediately after IT injections of 100µL BSA-capped GNPs (red) and citrate-GNPs solutions (green), day 6 and day 10 after IT injection. All the images are displayed at window width of 1500 HU and window level 700 to cover bone, metal and tumor tissue attenuations. The voxel size of the images is 105µm. The grayscale look up table is then shown in a more natural-like

color and GNPs are displayed in yellow. Insets show CT slices of mice bearing tumors, cropped specifically in the tumor region immediately after BSA-GNPs injection (red) and citrate GNPs (green), where the clustering process is more evident.

This evidence is also supported by Figure 2.5, which shows the differences in particle distribution volume within the tumor tissue. On day 0, the 3D reconstructed volume of the citrate-GNPs from the attenuation values extracted from the CT images is four times smaller than those created by the BSA-GNPs injection. 72h after particle injection, both the citrate and BSA-capped GNPs follow the same constant trend in volume until the tenth day.

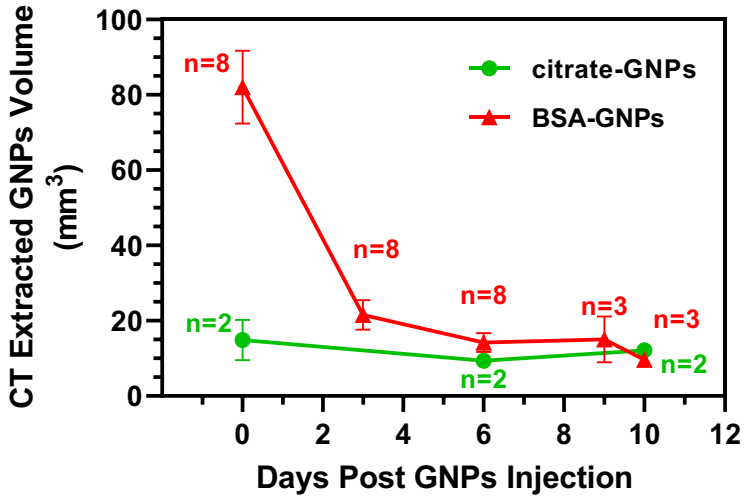

Figure 2.5 3D reconstructed volumes (mm3) of the GNPs from the attenuation values extracted from the CT images over the imaging timepoints.

In order to better understand the IT biodistribution pattern over time and eventually the clearance of the particles, we quantified the contrast in several organs at different time points. Figure 2.6 represents the CT values of attenuation (HU) of the heart, brain, kidneys, liver, intestine, tumor and bladder, extracted from circular ROIs selected on the CT images at the different time points after administration of citrate and BSA-capped GNPs. Due to the presence of clusters in the case of injections of citrate-GNPs, the analysis is divided into sub-measures for the tumor:

1. GNPs Intra-cluster (IC) to indicate the ROI inside the tumor and inside the cluster of GNPs
2. GNPs Extra-cluster (EC) to indicate the ROI inside the tumor and outside the cluster of GNPs.

As seen in Figure 2.6A, citrate-GNPs clusters are well enclosed in the tumor and remain there even after 10 days. The extra-cluster tumor area doesn't show the presence of particles over time. The absence of citrate-GNPs over time in this area indicates a biodistribution capability of the particles under the limits of detection. The CT attenuation results here suggest that the citrate-GNPs are not excreted in 10 days. This conclusion is further deduced because when compared to the baseline, no visible attenuation increments are distinguishable in other organs over time.

Conversely, the CT results from the images of BSA-GNPs-injected mice confirm contrast enhancement in the tumor ROI at the first time point (immediately after injection of BSA-GNP) with attenuation values of 354 HU, ~8% higher than the baseline (325 HU). Furthermore, the contrast remains stable over the subsequent 3 days, while at day 10, comes back to baseline levels. Despite the high accumulation in the intestine and partial changes in the other organs (heart, brain, kidneys, liver and bladder), the results suggest that the particles could be excreted after 10 days. Heart, brain, kidneys and liver all returned to baseline levels after 10 days, while the CT signals of the intestine increased gradually, indicating bile excretion of the particles. Accumulation in the bladder is still present after 10 days. This could indicate a nearly complete excretion of the particles from the body after 10 days.

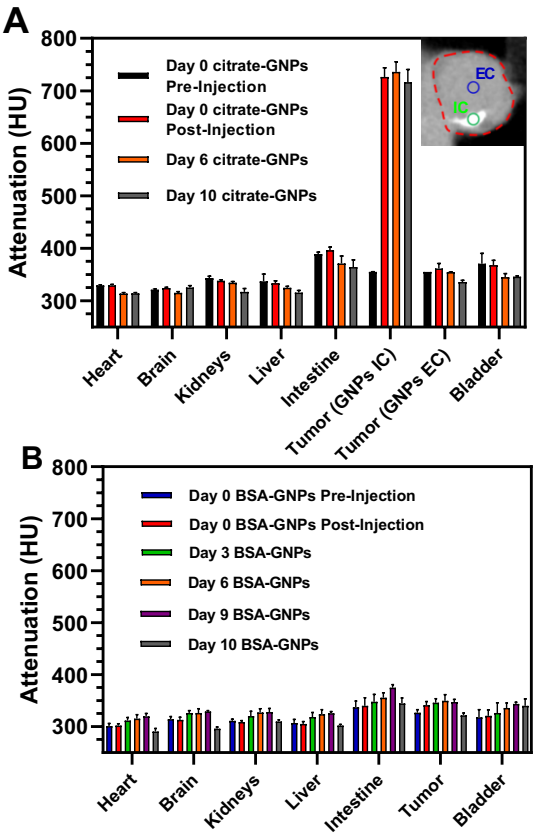

Figure 2.6 The CT attenuation values (HU) of various organs at different time points after administration of (A) citrate-GNPs and (B) BSA-GNPs. The analysis for citrate-GNPs divides the tumor ROIs in GNPs Intracluster (IC) and GNPs Extracluster (EC).

Despite their good biodistribution capabilities, a point of discussion is the lack of *in vivo* contrast enhancement of the BSA-GNPs when compared to the citrate-GNPs (~50% and ~8%, respectively). It becomes clear that a better and more immediate distribution in the tumor environment compromises CT contrast properties. Hence, the importance of calibrating the CT attenuation of the GNPs before *in vivo* injection for tracing a safe threshold and leveraging the CT-contrast proprieties of the particles.

2.4 Conclusion

In conclusion, the permanence of the GNPs into the tumor after ten days suggests the significance of GNPs as a potential theranostic agent. Further, the more homogeneous and uniform IT distribution of the BSA-GNPs may offer further advantages for surface passivation.

Chapter 3

Effects of Surface Protein Adsorption on the Distribution and Retention of Intratumorally Administered Gold Nanoparticles

3.1 Introduction

Theranostic nanomedicine for cancer management offers innovative strategies to non-invasively detect and diagnose the disease at its earliest premalignant state and to provide specific therapy against its progression and reoccurrence [68], [69]. However, one of the most significant challenges associated with the translation of theranostic nanomedicine to the clinic is the interaction between the nanomaterial and the tumor microenvironment [70]. In particular, when nanoparticles enter a biological system, their interaction with proteins can lead to the formation of a protein-corona adsorbed on their surface via electrostatic, hydrophobic, and van der Waals forces [71], which can alter particle stability [72], [73], dispersibility [74], [75], biodistribution [76], pharmacokinetics [77]–[79], and the toxicity profile [80]–[82].

Due to their unique optical properties [83]–[85], combined with their high biocompatibility and lack of toxicity [86]–[88], gold nanoparticles (GNPs) have demonstrated success among nanotheranostic cancer-related applications [89]. In addition to solid gold particles of various shapes and dimensions (nanobelts [90], nanowires [91], nanostars [92], etc.), core-shell gold coated particles[93]–[95] have also been rationally designed for application in cancer therapies [96], [97]. However, successful *in vivo* outcomes of the use of GNPs are strongly dependent on the interactions between the protein corona layer and the surrounding cells [98], [99]. Understanding GNP-protein interactions is crucial for the development, manufacturing, and translation of GNP-based nanotheranostics [100], [101]. An extensive body of literature has shown the effects of surface chemistry and size of spherical GNPs on the protein corona with the intent to control opsonization on GNPs [102]–[104].

The protein corona formed around the particle when administered *in vivo* is composed of a complex range of adsorbed proteins, such as albumin, immunoglobulin, glycoproteins, and apolipoproteins [105], which are proteins of lower affinity and higher-abundance that bind initially, while over time, are replaced by higher affinity proteins, such as fibrinogen or lysozyme [106]. There are mainly two layers of proteins: an inner layer of irreversibly bonded proteins interacting directly with the GNP surface which is called the *hard corona*, and an outer layer of proteins linked through weak protein–protein interactions, called the *soft corona* [107]. Displacement of the hydration layer which leads to the formation

of the overall particle corona is a complex, dynamic, and competitive process to stabilize the GNPs in a physiological environment [108]. In this configuration, epitopes which are normally buried in the interior sites of proteins can be exposed outwards from the soft corona layer of the particle [109], making GNPs recognizable for phagocytes [67], and consequently producing rapid clearance of the nanoparticles from plasma as well as accumulation in the liver and spleen [111]. Understanding how to control the physiological properties of GNPs can help mediate processes such as cellular uptake [112], immunological response [113], toxicity [114], circulation time [115], and transport from one organ to another, as well as their clearance [116]. While many studies focus on the protein content of blood and harnessing the enhanced permeability and retention effect (EPR) for particle accumulation near the tumor after systemic administration, similar principles related to the protein absorption can be considered for intratumoral injection since other biological compartments of the body, such as the interstitial fluid of tumors, also contain a high protein content [117] that can effect particle behavior. Therefore, the mechanisms studied related to formation of a protein corona from the hematic system can also be applied for other fluids.

In this study, we aim to evaluate the influence of protein surface adsorption on GNP *in vivo* biodistribution and retention after intratumoral injection. To study our nanoparticle conjugates, we used a Non-Small Cell Lung Cancer (NSCLC) murine model because its heterogeneity involves not only cancer cells but also tumor-infiltrating cells as well as the surrounding microenvironment [118]. Lung cancers and other solid tumors also contain stromal cells, such as fibroblasts and endothelial cells. Further, LLC tumors are considered highly heterogeneous as they contain subpopulations of cells of widely differing metastatic potential [119]. Tumor heterogeneity is an important cause of therapy resistance due to non-uniform drug distribution [120]. We hypothesize that by controlling the adsorption of proteins on the GNP surface, we can modulate the zonal distribution of the particles in the tumor. We previously demonstrated that our spherical GNPs have a significant radio-sensitization nature *in vitro* [121], inducing DNA damage in Lewis Lung Carcinoma (LLC) cells as well as excellent properties as contrast agents for Computed Tomography (CT) *in vivo* [122]. However, these preliminary studies didn't consider the hypothesis that surface protein adsorption can affect intratumoral distribution and retention of the particles. Therefore, we exploit CT imaging as non-invasive pre-clinical method to monitor and quantify the biodistribution of functionalized GNPs and highlight the differences in terms of spatial heterogeneity modulated by surface passivation.

3.2 Material and Methods

3.2.1 Synthesis of Gold Nanoparticles

Spherical GNPs were fabricated using citric acid (Sigma, St. Louis, MO, USA, C3674) rapidly combined with gold (III) chloride (Sigma, St. Louis, MO, USA, 379948). To achieve particle synthesis, an Erlenmeyer flask containing 600 μL of MilliQ water was allowed to boil using a heating mantle. After 30 s of refluxing in the flask, 4.8 mL of 0.039 M aqueous citrate was combined using a serological pipette. While continuing to boil, 7 mL of 0.033 M gold (III) chloride was next added in a single continuous motion, and the solution was left undisturbed as the color gradually transition from yellow to black to the final dark red. After room temperature equilibration, the pH of the solution was measured (pH = 3.5), and the sample stored for further use. This protocol results in the synthesis of citrate-stabilized GNPs in the size range of 30-40 nm. The average mean size and error per batch was measured by obtaining electron microscopy images of the sample and importing the images into Matlab for analysis (see section 2.3). The pH of the solution was adjusted up to 6 using drop-by-drop addition of a 1 M NaOH solution. GNPs (pH = 6) were centrifuged at 1500 x g for 5 minutes with an Eppendorf Centrifuge 5810R (Hamburg, Germany) using Amicon Ultra-15 100K filters purchased from Sigma-Aldrich (St. Louis, MO, USA, UFC910008). The filtrate solution, the water filtered from centrifugation, was stored for future dilutions and functionalization. Particles were concentrated up to 10 mg/mL, and stored at 4°C.

3.2.2. Surface Passivation of Gold Nanoparticles

We selected Bovine Serum Albumin (BSA, molecular weight 66.5 kDa) as a protein model since it is a soluble constituent of blood plasma and, therefore, it can be considered suitable for *in vivo* investigations. BSA powder (Sigma, St. Louis, MO, USA, A4503) was dissolved in the filtered water after particle centrifugation to obtain a 1 mg/mL solution. Only freshly prepared BSA solutions were used in these experiments and pH was monitored and maintained. Different volumes taken from this initial stock solution were added to the concentrated GNPs and allowed to incubate for 1h at room temperature for surface passivation (See Section 2.4.1). The solution was stored at 4°C.

3.2.3 Characterization and Physicochemical Properties of Gold Nanoparticles

Fabricated GNPs were characterized with spectroscopy using a UV/Vis Scanning Spectrophotometer (DU 730, Beckman Coulter, Inc., Brea, CA, USA). Typically, the UV−Vis spectrum of spherical non-aggregated GNPs has a band around 530 nm, due to the surface plasmon resonance (SPR), plus an absorption edge at shorter wavelengths due to inter-band transitions of d-band electrons. Dynamic light scattering (DLS) offered an analytical means to determine the particle size and polydispersity index (PDI), and Zeta Potential measurements were obtained using a Zetasizer Nano ZS (Malvern Panalytical, MA, USA). For DLS, the sample at a concentration below 1 mg/ml and at a volume of 1 mL was placed in a four-sided cuvette and measured at 25 °C. For this technique, the Brownian motion is measured and related to particle size by illuminating the particles with a laser and analyzing the intensity fluctuations in the scattered light to report a mean size. For Zeta Potential, 1 mL of particle sample was placed in a four-sided cuvette capped by the universal dip cell ZEN1002. For this technique, the instrument determines the electrophoretic mobility by performing an electrophoresis experiment on the sample and measures the velocity of the particles using Laser Doppler Velocimetry. Particles were imaged with a FEI Nova NanoSEM 230 (FEI Co., Hillsboro, Oregon, USA) under STEM mode with the vacuum set to 15 KV for both bright and dark field and measured using Matlab (v9.9.0.1467703, R2020b, The MathWorks, Inc., Natick, Massachusetts). Surface-enhanced Raman scattering (SERS) spectra of 3 μM BSA-GNPs were obtained using a custom Raman microspectrometer [123] with a 785 nm wavelength light source to calculate Raman shift values and tentative band assignments due to particle passivation. The sample was measured in a capillary tube where the beam spot was focused through an objective 50 μm past the glass/solution interface. An unenhanced Raman spectrum of BSA solution was recorded and subtracted from the BSA-GNPs SERS spectrum to remove any unenhanced Raman contributions.

GNP solutions in concentrations in the range 0 - 10mg/mL were aliquoted into microcentrifuge tubes and imaged using a Siemens Inveon High-Resolution micro-CT to assess their CT contrast properties and compare with a standard contrast agent (Omnipaque™ iohexol for injection 350 mg I/mL, GE Healthcare, USA). To avoid concentration gradients that can be created by larger particle sediments, samples were vortexed immediately before imaging. The CT parameters were a slice thickness of 105 μm, in plane resolution of 105 μm, tube voltage at 80 kV, tube

current at 500 μA, and exposure time of 240 ms. X-ray attenuation intensity was calculated in Hounsfield unit (HU) by processing the digital CT images (DICOM files) using 3DSlicer [124]. Quantification analysis was performed using 3DSlicer and selecting a 3D reconstructed region of interest (ROI) for each sample and then recording the mean attenuation value and plotting as a function of gold and/or iodine concentration in mg/mL. Weber contrast was calculated using the Equation 3.1:

$$W_c = \frac{I - I_T}{I_T} * 100 \quad (3.1)$$

where I is the attenuation value (HU) of a tumor ROI after GNPs/contrast injection and I_T is the attenuation value (HU) of the tumor baseline. GNP concentration was determined applying the Beer-Lambert Law on the SPR peak calculated by UV-Vis spectroscopy, assuming that the particles are spherical. Concentrations were also confirmed by ICP-OES.

3.2.4 BSA Adsorption on Gold Nanoparticles

The interaction of proteins with GNPs depends on variables, such as the chemistry of the adsorbed material and the medium components [58]. In this section, we investigate the nature and concentration of the BSA to be adsorbed, and its relationship with the pH of the immobilization medium.

3.2.5 Preparation of BSA-GNP Conjugates at Different pH Values

As the pH of the medium increases, the sorption properties of the GNPs change, generating a transition of monolayer protein immobilization to multilayers. Sotnikov *et al.* [125] demonstrate that pH of the immobilization medium can effect protein adsorption on GNPs: as the pH is modified from 4–5 to 8–10, an increase occurs in the maximum amount of adsorbed protein molecules on a GNP surface, likely due to this protein immobilization layer transition. In alkaline solutions, however, the GNP surface is not fully saturated, so that interactions can occur between the BSA-GNPs and other proteins in the body which can alter the protein corona structure, consequently also changing the proprieties of the particles.

However, our interests are more focused towards application in a slightly acidic environment, such as the tumor environment [126]. To determine saturation of the GNPs surface and protein layer, the GNP solution was adjusted to a desired pH, as described above. BSA solution was then added to the centrifuged GNP solutions to reach a final concentration ranging from 0.5 to 15 μM. pH values for these studies were maintained at 4.7, 6, 7, and 8.5. All experiments were conducted at ambient room temperature.

3.2.5 Adsorption Model

The adsorption model adopted here follows the work from Dominguez-Medina et al.[127] and Röcker et al.[128]. We approximated a BSA molecule as an equilateral triangular prism with height 3.4 nm, and the GNP, as a sphere with hydrodynamic radius (R) obtained by DLS measurement before surface passivation. Therefore, an increase in height below 2 times 3.4 nm corresponds to no more than single layer adsorption of BSA on the spherical GNP surface. The dependence of the hydrodynamic radius r([BSA]) on the number of protein molecules bound to a spherical GNP, assuming that the protein-coated nanoparticle can still be approximated by a sphere, is expressed by the following formula from [127] (Equation 3.2):

$$r([BSA]) = R \sqrt[3]{1 + \frac{V^{BSA}}{V^{GNP}} \frac{N}{1 + (\frac{K}{[BSA]})^{n}}} \tag{3.2}$$

where N represents the average number of protein molecules bound to the nanoparticles at a specific BSA concentration in the solution, n is the Hill coefficient (unitless), and K (mol/L) is the dissociation coefficient, which quantifies the strength of the protein–nanoparticle interaction, V^{GNP} is the volume of the uncoated particles (L), V^{BSA} is the molecular volume (L) of the bound protein (BSA). The experiment was performed by adding BSA solutions in different concentrations to the GNPs. The concentration of gold was kept constant, while the BSA concentration was variable. No aggregation or flocculation occurred (confirmed by UV-VIS spectroscopy). DLS measurements were performed on each sample in triplicate, and the hydrodynamic radius (Z-average divided by 2) was calculated. Data were analyzed by fitting an adsorption isotherm over the

considered range of BSA concentrations using the modified Langmuir model (Equation 3.2) and standard Langmuir model (Equation 3.2, n = 1). Data fitting was performed with Matlab (lsqnonlin, v9.9.0.1467703, R2020b, The MathWorks, Inc., Natick, Massachusetts).

3.2.6 Characterization in Various Media

To investigate changes in the effect of BSA adsorption on the GNP protein corona, particles were dispersed in media representing different sources of protein. We tested the particles dispersed in either 600 μM BSA enriched PBS, plasma obtained from healthy porcine (Male Castrated Yucatan Minipig, ~38 kg, S&S Farms, Ramona, California, USA), and Fetal Bovine Serum (FBS) (ATCC, Manassas, VA, USA, 30-2020). To obtain plasma, whole blood was collected in EDTA-treated tubes and centrifuged for 15 minutes at 2,000 x g. We performed DLS measurements to calculate the hydrodynamic diameter and UV-Vis spectroscopy as described in section 3.2.3.

3.2.6 Cellular Uptake of GNPs and Cytotoxicity In Vitro

Since each nanoparticle formulation is unique, accurate toxicity testing is needed for any proposed contrast agent in both preclinical research and potential clinical translation. To evaluate potential cytotoxicity as well as cellular internalization of the GNPs, Lewis Lung Carcinoma cells (LLC) were used as murine model of NSCLC. We performed MTT and trypan blue assays to estimate particle toxicity, and ICP-OES to quantify the gold content uptaken by the cells. Scanning transmission electron microscopy (STEM) was also used to confirm cellular uptake of GNPs as well as provide insight into the mechanisms of particle internalization.

3.2.7 Maintenance and LLC Subculture

Murine Lewis lung carcinoma (LLC) cells were purchased from ATCC® (American Type Culture Collection, Manassas, VA, USA) and cultured in either T-

75 or T-175 flasks. Cells were passaged for subcultured by first aspirating the culture medium with a pipette, rinsing with 1x phosphate buffered saline (PBS, Thermo Fisher Scientific, Waltham, MA, USA, SH30256FS), aspirating off the PBS, then rinsing with 0.25% trypsin - 0.53 mM EDTA solution (Thermo Fisher Scientific, Waltham, MA, USA, 25-200-056) and the neutralized with complete growth media consisting of Dulbecco's Modified Eagle's Medium (DMEM, ATCC®, Manassas, VA, USA) with 10% fetal bovine serum (FBS, USDA approved, ATCC®, Manassas, VA, USA), and 1% Penicillin-Streptomycin (10,000 U/mL, Thermo Fisher Scientific, Waltham, MA, USA). Cells were modified to be luciferase expressing (LLC-Luc) as previously described[121] through use of plasmid pLenti PGK V5-LUC Neo [129] (Addgene, Cambridge, MA, USA) which was packaged in lentiviral particles and performed at the Baylor College of Medicine (BCM) vector core facility. For the luciferase-expressing cells, 1% Geneticin (Thermo Fisher Scientific, Waltham, MA, USA) was added to the media to maintain culture. Cells were maintained in a HERAcell 150i CO2 incubator (Thermo Fisher Scientific, Waltham, MA, USA) set to 37 °C and 5% humidity.

3.2.8 Trypan Blue Assay

At a concentration density of $3x10^5$ cells/well LLC-Luc cells were seeded into 6-well plates containing 4 mL of complete media. Cells in each well were treated by adding from a solution of ~4 mg [Au]/mL, 50 μL of either citrate or BSA-GNPs (3 μM BSA). Each treatment was performed in triplicate wells and after treatment the plates were incubated. After 24 h incubation at 37 °C and 5% humidity, the wells were washed three times with 1x PBS and detached using 0.5 mL per well of 0.25% trypsin–0.53 mM EDTA solution. Cells where then resuspended with 1 mL of complete media and 10 μL of the samples were treated with 10 μL of Trypan Blue to determine cell count and viability using a Countess™ II FL Automated Cell Counter (Invitrogen). The remaining cells were centrifuged at 100G for 5 min, the supernatant removed, and used for ICP-OES quantification of gold content. Cells were monitored during GNP treatment using optical microscopy (Nikon Eclipse Ts2 Microscope, Nikon Instruments Inc., Melville, NY, USA).

3.2.9 Quantification of Intracellular Gold Content using ICP-OES

ICP-OES is a common technique for quantification of the cellular uptake of metal NPs since it offers high selectivity for elemental analysis. Measurements were performed on a Varian Agilent 720-es ICP spectrometer (Agilent, Santa Clara, CA, USA). Calibration curves for gold were obtained from a calibration standard (Au 1000 mg/mL in 10% HCl, Perkin Elmer) diluted in 1% trace metal grade nitric acid (Thermo Fisher Scientific, Waltham, MA, USA, A509) and 10% HCl (Thermo Fisher Scientific, Waltham, MA, USA, A508). Yttrium (Sigma Aldrich, St. Louis, MO, USA, Cat#01357) was used as internal standard for all ICP-OES measurements. Wavelengths of 242.794 nm and 267.594 nm were used to measure gold emission. Using the ICP-OES software (ICP Expert II), the gold concentration at each wavelength was calculated from the obtained calibration curve, and the measurements were averaged from both wavelengths. The reported concentrations were obtained by dividing the gold content obtained from ICP-OES by the total number of cells after 24h of particle incubation. 1mL aqua-regia solution (nitric acid and hydrochloric acid in a molar ratio of 1:3) was added to the vial containing the pellet of the cells. The solution was placed on a hot plate (T = 60 °C) in a chemical fume hood for digestion of the cellular matrix. After complete digestion, the solution was resuspended in 10 mL of standard diluent (10% HCl, 1% Nitric Acid) and filtered using 0.6 μm filters (MilliporeSigma™ Stericup Quick Release-GP Sterile Vacuum Filtration System).

3.2.10 MTT Assay for Cytotoxicity

The MTT (3-(4, 5-dimethylthiazolyl-2)-2, 5-diphenyltetrazolium bromide) Cell Proliferation Assay is used to quantify changes in the rate of cell proliferation by reduction of tetrazolium salts and spectrophotometric measurements. LLC-Luc cells were seeded at a concentration of $4x10^4$ cells/well into 96-well plates and incubated overnight for adhesion. Cells were treated with different concentrations (1.5μg [Au]/well and 5μg [Au]/well) of particles (in a volume of 10 μL) and incubated for 24h. After particle incubation, 10 μL of MTT Reagent (ATCC®, American Type Culture Collection, Manassas, VA, USA) was added to each well including control wells (consisting of either media alone, media with GNPs, or cells with media without GNPs) and incubated at 37°C for 2 to 4h (until a purple precipitate was visible under the microscope). Then 100 μL of Detergent Reagent (ATCC®, American Type Culture Collection, Manassas, VA, USA) was added to

each well (including controls) and stored at room temperature in the dark for 2 to 4h. Absorbance readings were performed at 570 nm and at 690 nm using a Synergy™ H4 Hybrid Microplate Reader (BioTek Instruments, Inc., Winooski, VT, USA).

3.2.11 Scanning Transmission Electron Microscopy (STEM) to Confirm GNP Uptake

The cells treated as described in Section 3.2.7 were fixed by resuspending the pellet after centrifugation in 1 mL of 4% paraformaldehyde (Electron Microscopy Sciences, Hatfield, PA, USA). Three washes of 0.1 M PBS were performed on the samples for 10 min each. After the cells were fixed, samples were treated for 2 h at room temperature with 2% osmium tetroxide (OsO_4) in cacodylate buffer. The samples were then washed again three times for 10 min in 0.1 M PBS followed by dehydration using a series of graded ethanol (30%, 50%, 70%, 90%) for 10 min each. The final washes used 90% acetone for 10 min and 100% acetone for 15 min repeated three times. To achieve resin embedding, the steps included: 2 h pre-inclusion in resin / 100% acetone (1:1), overnight pre-inclusion in resin / 100% acetone (2:1), 3 h pre-inclusion in 100% resin and finally, embedding in 100% resin using flat molds. To achieve complete polymerization, the samples were incubated in a 60°C oven for 48 h and sectioned using a diamond knife to generate 100 nm ultrathin sections. These ultrathin sections were mounted on copper grids (200 mesh) (Ted Pella, Inc., Redding, CA, USA), stained with uranyl acetate and lead citrate, and imaged in a bright field setting at STEM mode and a vacuum of 15 KV with a FEI Nova NanoSEM 230 (FEI Co., Hillsboro, Oregon, USA).

3.2.12 C57BL/6 Mice and LLC Model

In vivo experiments were performed using six-week-old female C57BL/6 mice, purchased from Taconic Biosciences (Rensselaer, NY, USA). All experiments conducted on the mice were approved by the Institutional Animal Care and Use Committee (IACUC) at the Houston Methodist Research Institute and were performed according to the principles of the NIH Guide for the Care and Use of Laboratory Animals, the provisions of the Animal Welfare Act, PHS Animal Welfare Policy, and the policies of the Houston Methodist Research Institute.

Housing and care were provided in accordance with the regulations of the Animal Welfare Act and recommendations of the Guide for the Care and Use of Laboratory. Under the effects of sedation, subcutaneous injection of $2x10^6$ of LLC-Luc cells was performed into the right flank, when the mice weight was around 20 g. Intra-tumoral (IT) injections of either saline (control group, n = 4), citrate-GNPs (50 µL, 4 mg/mL (low dose) for n = 8 mice or 15 mg/mL (high dose) for n=3 mice, pH = 6) or BSA-capped GNPs (50 µL, 4 mg/mL (low dose) for n = 8 mice or 15 mg/mL (high dose) for n = 3 mice, pH = 6, 3 µM BSA) occurred once the tumor volume reached around 100 mm^3. All injections were performed after anesthetizing the animals with isoflurane. Injections were performed either manually or automatically using a syringe pump (KD Scientific Inc., Holliston, MA, USA) set to 0.43 µL/s. Animals were monitored daily to ensure good body condition, adequate food/water, and clean cages. CT imaging was performed pre-injection (as a baseline for the biodistribution analysis) as well as immediately post-injection, and on days 3, 6, and 9 post-injection. CT imaging was achieved using a Siemens Inveon Multi-Modality (MM) System controlled with the Inveon Acquisition Workplace (IAW), with slice thickness of 103.25 µm, in plane resolution of 103.25 µm, tube voltage at 80 kV, tube current at 500 µA, and exposure time of 240 ms. Tumor volumes (V) in mm^3 were calculated through daily measurements of the tumor axes using digital calipers and the following formula in Equation 3.3:

$$V = \frac{D * d * d}{2} \tag{3.3}$$

where D and d represent respectively the major and the minor axis of the tumor measured in mm. Study endpoint was determined as 19 days post tumor cell injection OR tumor volume greater than 2 cm^3, tumor interfering with normal physiological function, surgical complications, or other symptoms as outlined in the HMRI Guidelines and Policies for Determination of Humane Endpoints and Tumor Monitoring Policy as well as recommendation of the CMP veterinary staff.

3.2.13 Determination of Au in Organs and Blood

Mouse tumors, livers, kidneys, spleens, and lungs, were harvested upon euthanasia, 9 days after low dose particle injection (n = 8/group) and mouse tumors, livers, kidneys, spleens, lungs, hearts, brains and blood were harvested 3, 6, or 9

days after high dose particle injection (n = 3/group) and were weighed and flash frozen at –80 °C. Organs and blood were then dissolved in 2 mL of fresh aqua regia, heated at 60°C for 1h, and left under the hood until the samples were completely dissolved. After complete digestion, the solution was resuspended in the standard diluent (10% HCl, 1% Nitric Acid) to 10 mL and filtered using 0.6 μm filters (MilliporeSigma™ Stericup Quick Release-GP Sterile Vacuum Filtration System). Gold concentration was determined using a Varian Agilent 720-es ICP-OES spectrometer (Agilent, Santa Clara, CA, USA).

3.2.14 Statistical Analysis

GraphPad Prism 8 (version 8.3.0; GraphPad Software, Inc., San Diego, CA, USA) was used for statistical analyses. Mean ± s.e.m. values were calculated for all results. One-way analysis of variance (ANOVA) with Tukey's multiple comparisons test was used to assess statistical significance.

3.3 Results

3.3.1 GNP Characterization and Physicochemical (Charge, Size, Functionalization, X-ray Attenuation) Properties

Spherical GNPs were synthesized and measured with electronic microscopy to have a particle diameter of 36 ± 5 nm for the citrate-GNPs and 41 ± 8 nm for the BSA-coated GNPs (mean ± SD). Since the optical properties of spherical GNPs are dependent on particle diameter, we chose this particle size as it produced a strong SPR peak. While smaller particles might diffuse more easily and faster, the SPR band for GNPs with size smaller than 10 nm is largely damped [83]. Finally, it should be noted that the CT contrast properties are not dependent on particle size [28]. Histograms of both particle types are shown in Figure 3.1A. Unfunctionalized and BSA functionalized particles appeared similar in color, spherical and well rounded, and with low polydispersity (insets of Figure 3.1A). The hydrodynamic diameters of the GNPs as measured by DLS, were within error of the core diameters estimated from STEM. GNP surface charges were found to be negative as expected. Both sample types displayed similar optical absorption spectra (Figure 3.1B) in the UV-VIS. The 4 nm red shift of the SPR peak (from 530 nm to 534 nm) and

representative SERS spectrum of BSA with gold nanoparticles (Figure 3.1C) confirm protein surface passivation. Assigned band positions are in accordance with previous studies [130]. CT phantom imaging was performed to demonstrate the high X-ray attenuation properties of the particles. As shown in Figure 3.1D, the change in the attenuation levels expressed by the percentage variation in the Weber contrast compared to the tumor background linearly correlates with GNP concentration. Both citrate-GNPs and BSA-GNPs present significant greater attenuation values compared to a standard contrast agent (Omnipaque350) for concentration above 3 mg [Au]/mL (**p<0.005, ****p<0.0001). No significance was highlighted between the citrate-GNPs and BSA-GNPs.

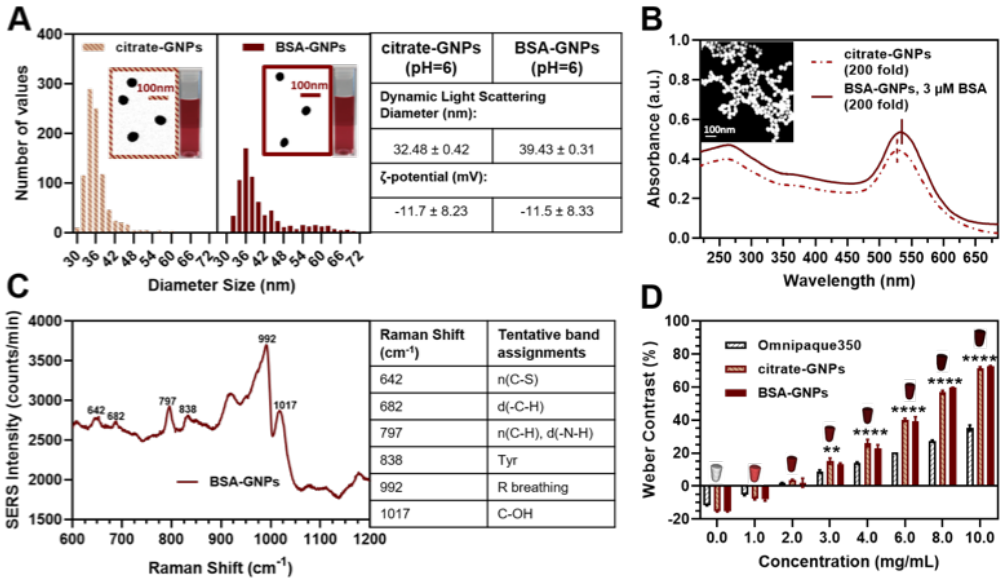

Figure 3.1 GNP surface passivation and characterization. (A) Distribution analysis, size and charge: histograms (n>700) for citrate-GNPs and GNPs functionalized with BSA (BSA-GNPs) calculated using a MATLAB algorithm based on STEM images. Insert table shows DLS diameter and ζ-potential. (B) Absorbance spectrum of citrate-GNPs (dashed line) and BSA-GNPs (solid line) as well as their size and shape captured by scanning electron microscopy (SEM) (inset represents citrate-GNPs). (C) Surface-enhanced Raman scattering (SERS) spectrum of BSA-GNPs and table of Raman shift values and tentative band assignments. (D) Weber contrast calculated based on computed tomography (CT) phantom and tumor background. Citrate-GNPs and BSA-GNPs present higher X-ray attenuation properties compared to a standard contrast agent (Omnipaque350). Significant differences between GNPs (citrate-GNPs and BSA-GNPs) and standard contrast agent for concentration above 3 mg/mL (** $p < 0.005$, **** $p < 0.0001$). Number of repetitions for each experiment: 3.

3.3.2 BSA Adsorption Models on GNPs

After the citrate-reduction synthesis, GNPs can have acidic or slightly acidic pH (in the range of 3–6) depending on relative concentrations and particle size [131]. Without any pH modifications, our particle solution pH is 3.5. Figure 3.2 shows the adsorption isotherms obtained fitting the hydrodynamic radii, experimentally determined with DLS as a function of BSA concentration and pH. BSA adsorption saturates according to the predicted model. The dotted lines (black and gray) in Figure 3.2B-E respectively represent the Langmuir model for adsorption (with Hill's coefficient n = 1) and the modified Langmuir model (where n < 1) for anti-cooperative binding, which indicates strong repulsive forces between free and bound BSA molecules that increase in number as more binding sites on the surface become occupied. The adsorption isotherm for 35 nm GNPs at pH 4.7, 6.0, and 7.0 follows an anti-cooperative binding model, while at pH = 8.5, follows a cooperative binding model. Adsorption beyond a monolayer is predicted to be negligible for GNPs at pH 4.7, 6.0, and 7.0.

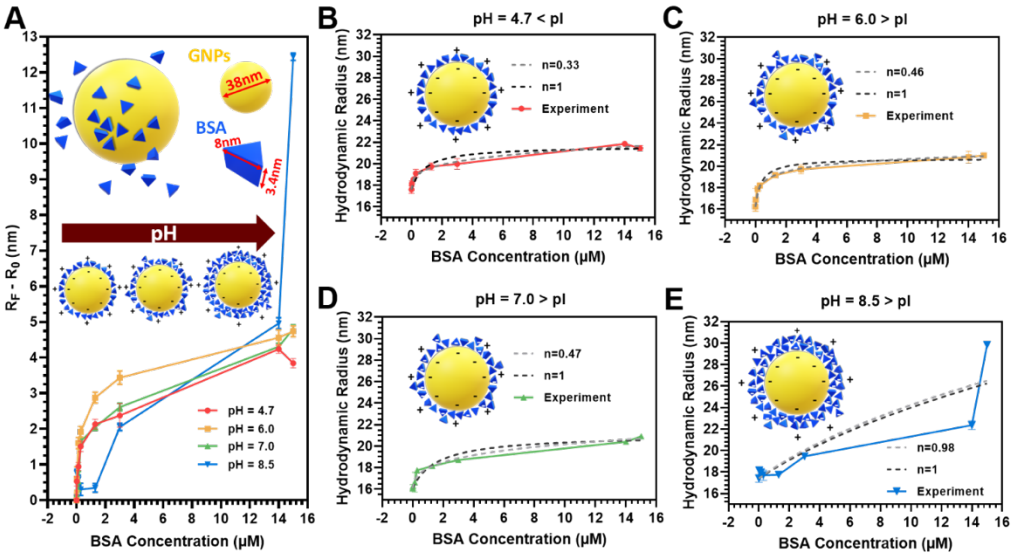

Figure 3.2 Adsorption isotherms (T = 25 °C) showing hydrodynamic radii experimentally determined with Dynamic Light Scattering as a function of BSA concentration and pH. (A) Adsorption of BSA on the GNP surface at different pH values above and below the Isoelectric Point (pI) of BSA (pI = 5). The y-axis in (A) was calculated by subtracting the hydrodynamic radius of the citrate-GNPs (R0) at their respective pH from the hydrodynamic radius of each adsorption point experimentally determined (RF). Data is fit using the Langmuir model and results are reported for (B) pH = 4.7, (C) pH = 6.0, (D) pH = 7.0, and (E) pH = 8.5. Isotherms with returned best fit Hill coefficient where n is variable (gray dashed line) or non-cooperative binding model where n = 1 (dashed

black line). The adsorption isotherms for 35 nm GNPs at pH 4.7, 6.0, and 7.0 follow an anti-cooperative binding model, while at pH 8.5 follow a cooperative binding model. Number of repetitions for each experiment: 3.

We also monitored the citrate-GNP and BSA-GNP particles (3 μM) visually and spectroscopically as well as changes in the hydrodynamic diameter when resuspended in either water, a solution of 600 μM BSA enriched PBS (which corresponds to the average physiological level of proteins), plasma, or FBS (Figure 3.3) to mimic a simulated physiological environment. We observed (Figure 3.3A) no macroaggregation or flocculation phenomena, as well as no visible change in color, when dispersing the particles in a source of protein as a function of surface functionalization at these pH values. We also found that the hydrodynamic diameter of the particles (Figure 3.3B) increased when the particles were dispersed in media containing an external source of protein, whereby the increasing trend in size went from water to BSA enriched PBS to FBS and finally to plasma. Interestingly, in the plasma, the sizes were larger for the BSA-GNPs than the citrate-GNPs indicating that proteins from the plasma were likely adding layers to the corona rather than displacing the BSA. The DLS data is complemented by the UV-Vis spectra (Figure 3.3C-F) of the particles in various media. There is an observed SPR shift from 530 to 535 nm when the particles are coated with BSA in water (Figure 3.3C) and this shift remains apparent in all three protein-rich media (Figure 3.3E-F) even for the citrate-GNPs, indicating that they become passivated with protein from the media under these conditions. We decided to maintain GNPs at pH = 6.0 for the in vivo experiments, because they are stable in a simulated physiological environment and their pH is closer to the extracellular pH of the tumor environment, which is slightly acidic (6.0 – 7.4) because of the extra secretion of lactic acid and CO_2 by the tumor cells [132].

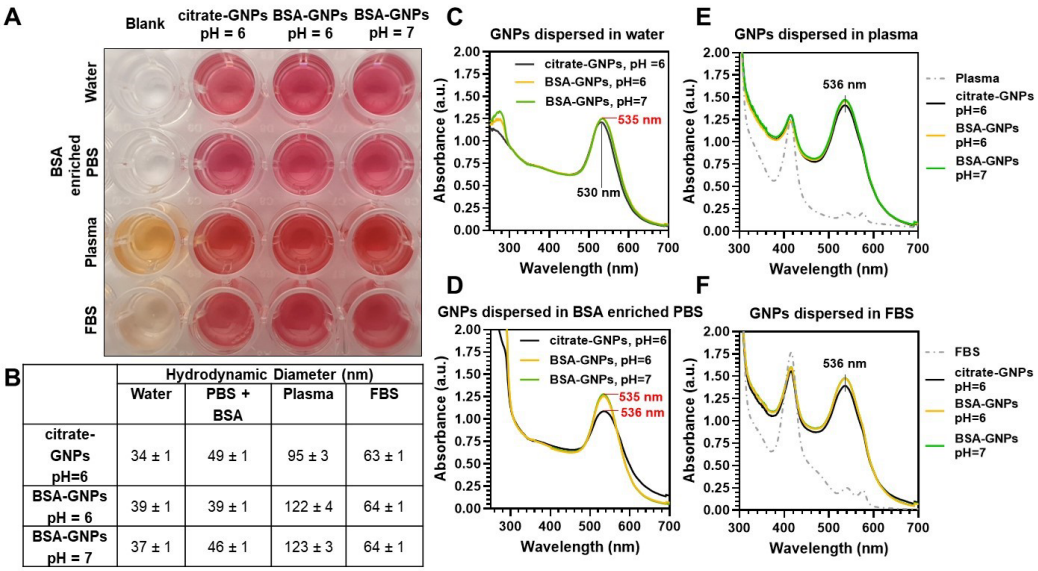

B

	Hydrodynamic Diameter (nm)			
	Water	PBS + BSA	Plasma	FBS
citrate-GNPs pH=6	34 ± 1	49 ± 1	95 ± 3	63 ± 1
BSA-GNPs pH = 6	39 ± 1	39 ± 1	122 ± 4	64 ± 1
BSA-GNPs pH = 7	37 ± 1	46 ± 1	123 ± 3	64 ± 1

Figure 3.3 Optical photo, hydrodynamic diameter, and UV-Vis spectra of GNPs as a function of surface functionalization and immobilization media. (A) Photographic image showing wells containing citrate-GNPs (pH = 6) and BSA-GNPs (3 μM, pH = 6 or pH = 7) dispersed in water, 600 μM BSA enriched PBS, plasma, and FBS. (B) DLS measurements show changes in hydrodynamic diameter as a function of surface functionalization and dispersion media at these pH values. (C-F) UV-Vis extinction spectra of citrate-GNPs and BSA-GNPs dispersed in (C) water, (D) 600 μM BSA enriched PBS, (E) plasma, and (F) FBS. Number of repetitions for each experiment: 3.

3.3.3 In Vitro Uptake of GNPs

In vitro assessments with optical microscopy of the LLC-Luc cells incubated with citrate-GNPs and BSA-GNPs after 24h showed aggregation of the citrate-GNPs (Figure 3.4Ai), while the BSA-GNPs remained stable and micro-clusters of the particles were not visible (Figure 3.4Aii). The intracellular content of gold after incubation of the LLC-Luc cells with citrate-GNPs and BSA-GNPs for 24h was clearly visible with electronic microscopy (Figure 3.4A-iii-iv). The inset of Figure 3.4Aiii shows particle internalization by macropinocytosis, in which the particles are taken into an endocytic vesicle in a nonspecific bulk fluid uptake. We noticed that the BSA-GNPs are internalized in larger vesicles (1-2 μm), while in the case of citrate-GNPs, macropinocytosis is accompanied by the presence of particles uptaken by endosomes in different stages of maturation (early endosome, late endosome and lysosome). This is not surprising as GNPs have been found to undergo both endocytosis and exocytosis patterns into cells [133]. Analysis of

MTT and Trypan blue assays after 24h of particle incubation shows that a high concentration of functionalized and unfunctionalized nanoparticles does not impact cytotoxicity (Figure 3.4B). The lack of any noticeable toxicity from citrate-GNPs and BSA-GNPs or cell proliferation suppression compared to untreated cells provides evidence for safe application in vivo both with functionalized and unfunctionalized particles. ICP-OES was used to quantify the Au mass in the LLC-Luc cells. Figure 3.4C shows Au concentration per cell. No statistical significance is highlighted between groups, although the citrate-GNP content is higher than the BSA-GNP content in LLC-Luc cells. This result can be partially explained by the saturated protein corona formed in the case of BSA-GNPs, which decreases the uptake efficacy of GNPs by cells. However, whether are significantly time dependent or cell type dependent are issues that need to be addressed in future studies.

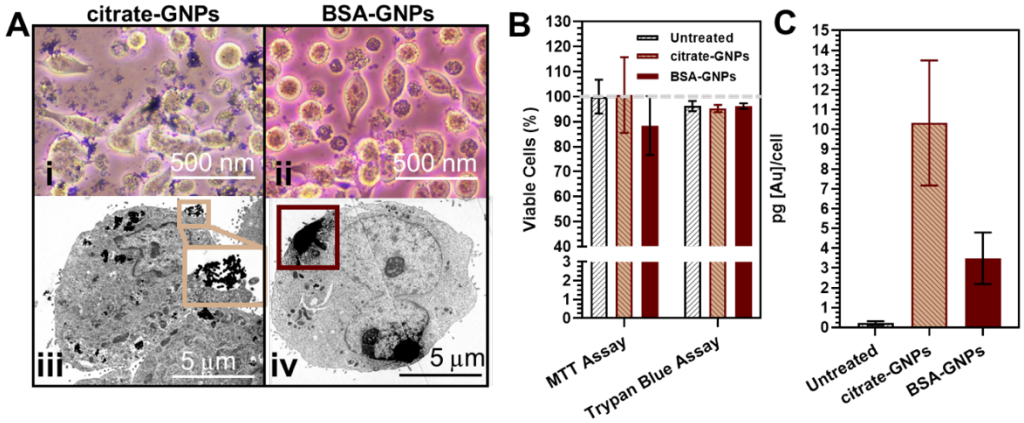

Figure 3.4 Evaluation of particle uptake and viability with LLC-Luc cells. (A) Optical microscopy (i-ii) and STEM (iii-iv) images of cells treated and incubated for 24h. (B) MTT and Trypan Blue assays for cells treated and incubated for 24 h. No significant differences between groups. (C) Quantification of GNPs internalized in LLC-Luc by ICP-OES after 24h. In (B) and (C) cells were treated and incubated in triplicate wells and data are plotted as the mean with s.e.m. Dashed line represents 100% cell viability. Number of repetitions for each experiment: 3.

3.3.4 Manual Intratumoral Injection of Low Dose GNPs

Representative CT images acquired from follow-up scans after manual low dose (50 µL of 4 mg/mL) GNP injection are shown in Figure 3.5A and indicate that the injected nanoparticles produce strong CT contrast. 9 days post injection, we

were still able to locate particles in the tumor volume. We quantified the intratumoral contrast at different time points (Figure 3.5B) as well as the volume of the visible particles diffused in the tumor area (Figure 3.5C). Mean attenuation values were calculated in Hounsfield Units (HU) within the GNP volume over time. Sustained strong CT contrast highlighted a significant difference between the BSA-GNPs when compared to both the control group (saline) and citrate-GNPs (*$p < 0.05$, **$p < 0.005$). This result is consistent with the increase in BSA-GNP volume over time in Figure 3.5C: the more the BSA-GNPs diffuse throughout the tissues, the less they attenuate the X-rays. Citrate-GNP volume is constant over time, confirming the preliminary results we previously obtained [122]: citrate-GNPs do not diffuse over time intratumorally, but instead form a single cluster of particles. Overall, a heterogenic intratumoral distribution pattern was found for both citrate-GNPs and BSA-GNPs. However, we can't exclude those particles may be forcefully spread out by the tissue as the tumor grows. The BSA-GNPs particles accumulated mostly in the tumor periphery, even though smaller depositions were found throughout the whole tumor region. Elemental Analysis performed with ICP-OES (Figure 3.5D) also confirms the presence of the particles in the tumor 9 days post-injection. Significant differences are highlighted between the saline and BSA-GNP groups (***$p < 0.0005$, Tukey's multiple comparisons test) and the citrate-GNP and BSA-GNP groups (**$p < 0.005$, Tukey's multiple comparisons test). This outcome validates the hypothesis that the protein corona of GNPs influences intratumoral distribution and retention of nanoparticles. We also performed elemental analysis for the spleen, kidneys, liver, and lungs of the mice 9 days post GNP injection. Although both particle types were administered through intratumoral injection, we surprisingly saw evidence of gold content in these other organs, however, no statistical significance was determined.

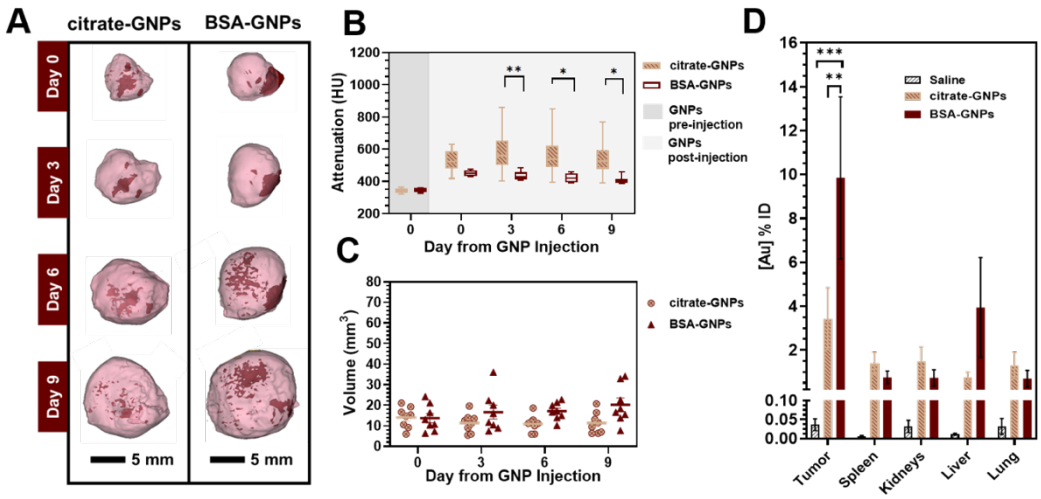

Figure 3.5 microCT and ICP-OES results both confirm that particles remain in the tumor 9 days post-injection. (A) Representative 3D volume renderings of microCT images of concentrated GNPs manually intratumorally injected into solid LLC-Luc tumors grown on the right flank of C57BL/6 mice (9 days follow up). Images are rendered at a window level of 1090 HU with 930 HU window width. With this color look up table, solid tumors are shown in pink (40% transparency) and contrast arising from the injected GNPs is shown in dark red (GNP clusters). Images are displayed with a voxel size of 100 µm. (B) Mean attenuation values in Hounsfield Units (HU) calculated within the GNP cluster volume over time using CT follow-up images. Significant difference of BSA-GNPs vs saline group and citrate-GNPs over time (*$p < 0.05$, **$p < 0.005$ Tukey's multiple comparisons test). (C) GNP cluster volume over time calculated using CT follow-up images. (D) Biodistribution of citrate-GNPs and BSA-GNPs in digested organs 9 days post-injection (n = 8 mice per group) using ICP-OES. Saline injections were performed on 4 mice as a negative control group (black bars). A two-way ANOVA test was done to compare the interactions between each group. Significant difference of BSA-GNPs vs saline group and citrate-GNPs (**$p < 0.005$, ***$p < 0.0005$ Tukey's multiple comparisons test).

3.3.5 Automatic Syringe Pump Intratumoral Injection of High Dose GNPs

Ex vivo photographs of tumors taken after sacrificing the mice on days 3, 6, and 9 post-injection (Figure 3.6A) and representative CT images (Figure 3.6B) with corresponding mean attenuation values (Figure 3.6C) acquired from follow-up scans after automatic high dose (50 µL of 15 mg/mL) GNP injection allow for comparison of intratumoral distribution. Data reported here are consistent with the results shown in Figure 3.5, the higher dose citrate-GNPs also appear more as a single central cluster of particles, while the BSA-GNPs are more diffuse around the tumor edge. Figure 3.6D shows the volume of GNPs quantified intratumorally for both treatment groups over time. When compared with Figure 3.5C, where we

observe less than 25 mm^3 in volume (equating to less than 50% of the injected volume in the tumor), under these conditions the volume is around 50 mm^3 (equating to close to 100% of the injected dose). Also, the gold quantified in the solid tumors from ICP-OES analyses show close to 100% for both treatment groups. We did notice a drop in the percent of gold accumulated in the tumors of two BSA-GNP injected mice: one from day 3 and one from the day 6 group. In most of the other organs and blood analyzed, the quantity of gold measured was negligible except for the liver, lung, and spleen of these same two mice. Overall, we attribute the greater percent gold quantification in the tumors through both CT and ICP-OES shown in Figure 3.6 due to the use of the injection pump and a more concentrated sample.

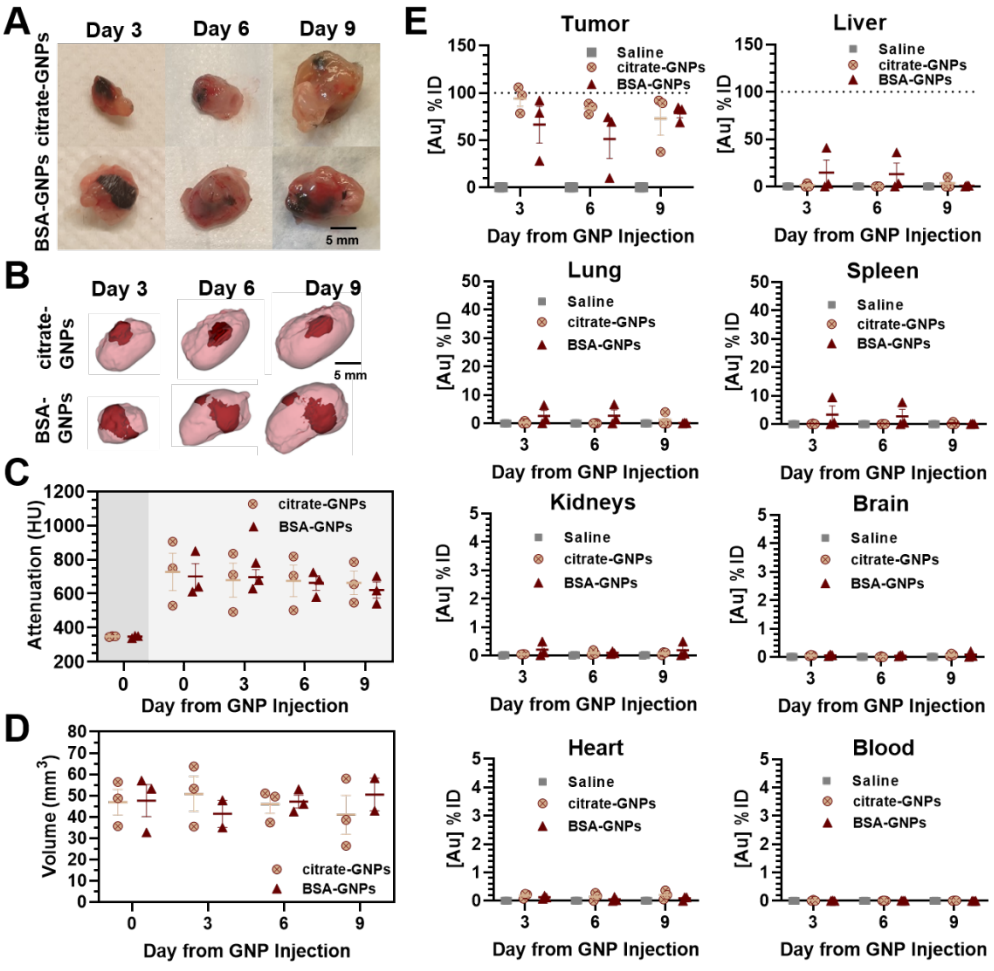

Figure 3.6 MicroCT and ICP-OES demonstrate particle distribution at different time points after high-dose intratumoral injection using an injection pump. (A) Ex vivo LLC solid tumors at different sacrifice time points. (B) 3D renderings of the intratumoral

biodistribution of citrate-GNPs and BSA-GNPs from microCT images. Residual intratumoral GNPs are rendered in dark red, tumor tissue is rendered in pink (40% transparency). (C) Mean attenuation values in Hounsfield Units (HU) calculated within the GNP cluster volume over time using CT follow-up images (GNP pre-injection: dark gray area, GNP post-injection: dark gray area). (D) GNP cluster volume over time calculated using CT follow-up images. (E) Biodistribution of citrate-GNPs and BSA-GNPs in digested tumors, organs (liver, lung, spleen, kidneys, brain, heart), and blood over time (n = 3 mice per group) using ICP-OES. Saline injections were performed on 3 mice as a negative control group. All data in the figure are reported as mean ± s.e.m. Dashed lines represent 100% of the injected dose.

3.4 Discussion

We demonstrated the fabrication and characterization of citrate-stabilized and BSA surface passivated GNPs, assessed their cellular uptake and lack of cytotoxicity in vitro, and evaluated their biodistribution and retention in an in vivo murine model of NSCLC. Recent studies have demonstrated the significant effects of albumin on the physicochemical properties of nanoparticles which inhibits plasma protein adsorption and decreases blood clearance time [134], [135]. However, there still remains a lack of knowledge regarding how the surface chemistry of GNPs can influence particle distribution within a tumor microenvironment. Evaluating and providing better understanding the effects of surface passivation may help advance their clinical translation as theranostic tools.

Several works have studied protein corona formation after intravenous injection of particles [80], [136]. The advantage of direct administration of nanomaterials into the bloodstream is related to their rapid distribution throughout the vasculature. However, this feature can also result in a rapid clearance by organs, such as the kidneys and liver or the reticuloendothelial system. In this study, we overcome this limitation through intratumoral injection. This approach enables administration of highly concentrated nanoformulations. With this strategy, we were able to demonstrate that the particles are retained intratumorally for 9 days, without significant accumulation in other organs.

Although intratumoral injections enable direct delivery of the nanomaterial into the interstitium of cancerous tissue, the interstitial tumoral pressure is higher than healthy tissue. This elevated interstitial fluid pressure gradient generally pushes the injected formulation out of the tumor and produces higher leakage of the drug into the surrounding tissue. Identifying the intra-tumoral distribution of nanoparticles is

clinically relevant because it can help determine the success of nanomedicine-based therapy and has often been considered a physical mechanism of drug resistance.

It is now known that both chemical and biological components play roles in the radiosensitization process in addition to physical processes,[61] therefore, it is expected that the observed different distribution patterns dependent on the particle functionalization would effect radiosensitization. These effects may be due to aspects such as the quantity and distance of nearby particles and the percent uptake and location of the particles inside or near various cell types undergoing different phases of replication. For example, it is generally understood that cells that are dividing quickly and are highly active metabolically are more radiosensitive. Therefore, protein surface modification that results in higher particle distribution in high turnover cells would likely further enhance radiosensitization effects which may prove useful in future clinical application.

In vivo results from this study show that the intratumoral biodistribution of GNPs is dependent on surface passivation and can result in significant heterogeneity throughout the tumor microenvironment. Predominately perfusion of BSA-GNPs occurs throughout the tumor periphery with reduce deposition covering the entire tumor volume. While some of this could be attributed to off centered injection or the fact that tumor growth will further spread out the particle distribution, we attribute the majority of this response to the abnormal and heterogeneous vascular structure of the LLC tumor, suggesting perfusion rather than permeability of the GNPs as the limiting factor for tumor accumulation. Despite perivascular accumulation, we demonstrate that BSA surface passivation can affect the intratumoral distribution and retention of GNPs.

3.5 Conclusions

In summary, we investigated whether protein surface adsorption can influence GNP biodistribution in a NSCLC animal model by applying high-resolution preclinical CT imaging. By controlling protein absorption on the GNP surface, we obtained a significant difference in the intratumoral distribution and retention of the particles, as demonstrated through quantitative CT and ICP-OES analysis. Moreover, our investigations revealed that surface passivation of GNPs controls the mechanism of cellular uptake in vitro. Further evaluation will expand our

knowledge in how to better control the surface passivation of GNPs and prove useful for clinical translation of nanoparticle-based therapies.

Chapter 4

Zonal Intratumoral Delivery of Nanoparticles Guided by Surface Functionalization

4.1 Introduction

Overcoming challenges associated with therapeutic and nanoparticle tumor uptake and tissue penetration is critical for establishing effective cancer therapies. Accompanying systemic administration, challenges include off-target effects and associated toxicities. Intratumoral delivery has emerged as a means to enhance delivery locally and directly into the tumor microenvironment (TME), thereby limiting systemic toxicity while permitting lower dosages [137], [138], [139, p.] Significant research is dedicated toward enhancing delivery to the TME and bypassing systemic administration, yet reproducible means to target zones within the TME itself have not been identified. As the TME is notoriously heterogeneous, this creates challenges in homogeneous therapeutic distribution. Current strategies to enhance nanoparticle diffusion into tissue with abnormal vasculature, such as solid tumors, include increasing vasculature permeability through approaches such as preconditioning with local hyperthermia to elevate intratumoral interstitial fluid flow [57], [140] delivery of transient anti-angiogenic therapies to temporarily increase blood flow [141] and administration of anti-vascular endothelial growth factor receptor antibody to improve tissue perfusion [142]. While both morphologic and functional vasculature normalization have shown to temporarily improve agent perfusion to facilitate intratumoral delivery, remodeling processes occur that, ultimately, reduce vessel permeability and impair nanoparticle transport inside the tumor [143].

As only a fraction of an injected dose reaches the TME through the vasculature due to high interstitial fluid pressure [144] supporting methodologies are needed to achieve tumor uptake and retention. Strategies to enhance particle accumulation into specific tumor regions include magnetic nanoparticles directed by external magnets [114], [115] ultrasound-mediated delivery to induce mechanical membrane stretching and pore formation [147] tumor recruitment of nanoparticle-containing monocytes and macrophages [148] and pH-responsive surface coatings which improve retention upon entering an acidic TME [149], [150]. However, challenges related to scale-up and resource-efficiency limit their use [151]. These techniques also depend on additional external environmental or internal factors, such as chemoattractive gradients needed to recruit nanoparticle-loaded monocytes or metabolic shifts to direct nanoparticle accumulation.

Regarding Gold Nanoparticles (GNPs), those ranging from 40-50 nm in diameter have been reported to accumulate predominantly (>80%) in the spleen and liver after systemic injection, with only a negligible fraction (~1%) localized inside

the tumor. This reduced dose within the tumor, attributed to their sequestration by the reticuloendothelial system, results in suboptimal nanoparticle uptake and heterogeneous GNP spatial distribution that significantly diminishes therapeutic and diagnostic efficacy [152], [153]. Loco-regional administration of nanotherapeutics mitigates many issues related to dose reduction following systemic exposure, overcoming important biological barriers to absorption in solid tumors such as stiffening of the extracellular matrix (ECM) and increased interstitial pressure [154], [155]. Despite the limitations of intratumoral injection, such as the inability to directly target inaccessible metastatic lesions [156] and deep-seated tumors [157] these challenges can be resolved through initiation of a host immune response and abscopal effect[158] to induce regression of distant untreated lesions [159]. Local, intratumoral delivery provides direct access to organized tertiary lymphoid structures within the tumor, [157] subsequently targeting lymphocytes and other immune cells that travel through lymphatic vessels. Understanding how loco-regional agents accumulate after intratumoral injection within the TME could advance our ability to molecular engineer them such that they distribute with higher concentrations at regions of enriched biomarkers or immune cells.

In addition to administration method, the intratumoral GNP distribution profile is strongly dependent upon their physicochemical properties; especially size, surface charge, surface functionalization, and shape [160]–[163]. We previously demonstrated the importance of surface passivation to control GNP distribution in a murine model of lung cancer [54], [55], [164]. However, a thorough understanding of these properties for customize nanoparticle design to achieve desired intratumoral pharmacokinetics and spatiotemporal distribution profiles could be the holy grail of cancer nanomedicine, promising to advance drug delivery and optimize outcomes.

In this work, we demonstrate controlled spatial delivery of intratumorally injected GNP (zonal delivery) by leveraging different surface chemistries while minimizing variables in administration through injection with a syringe pump set at constant dispense volume and flow rate. We experimentally observed differences in intratumoral distribution patterns of GNPs coated with three different chemical moieties (citrate, phosphothioethanol PTE, and polyethylene glycol PEG). To mechanistically characterize differences in GNP intratumoral distribution patterns, studies are complemented with mathematical modeling [165]–[167] of particle transport following intratumoral injection that considers particle reactivity over time.

Nanoparticle transport modeling has traditionally focused on tumoral delivery following systemic injection [165], [167] rather than local. To this end, Mahesh et al. modeled nanoparticle tumoral transport following intratumoral injection using a convection-diffusion equation, and studied effects of nanoparticle size, injection site, and vascular normalization on intratumoral distribution [168]. They incorporated interstitial fluid flow to obtain interstitial fluid pressure and velocity profiles in the tumor to investigate transvascular clearance of nanoparticles from the tumor interstitium. However, their model does not include nanoparticle interaction with cellular components and ECM of the tumor. Similarly, Klapproth et al. developed a physiologically-based pharmacokinetic model to study whole-body distribution of superparamagnetic iron oxide nanoparticles following intratumoral injection and compared results to intravenous injection [169]. Their model is limited to temporal evolution of nanoparticle concentration inside the tumor and other organs and does not study nanoparticle spatial distribution profiles. Here, we hypothesized that upon intratumoral injection, nanoparticle transport in the tumor interstitium is strongly governed by nanoparticle interaction with cancerous cells and ECM components, which in turn is affected by differences in surface chemistries, leading to distinct intratumoral GNP distribution patterns. To test our hypothesis, we modeled GNP transport following intratumoral injection using reaction-diffusion equations, which simulate spatiotemporal evolution of GNPs inside the tumor. We chose a macroscopic scale continuum approach adapted from our previous work involving transport modeling of hydrogel-embedded nanoparticles injected intratumorally into glioblastoma tumors [170]. Integration of mathematical modeling with in vivo experimentation allows us to quantitatively characterize the nanoparticle biodistribution intratumorally towards the establishment of zonal-directed drug delivery within a tumor. These exciting results provide a foundation for the development of region-specific cargo delivery that can advance our ability to modulate various processes driving cancer progression as well as provide control over the retention and distribution of agents toward their specific surface target within the TME.

4.2 Methods

4.2.1 Animal Model

All experiments conducted on the animals were approved for study (protocol # IS00005178 approved 6 May 2019 and protocol # IS00005819 approved 26 March

2021) by the Institutional Animal Care and Use Committee (IACUC) at the Houston Methodist Research Institute and were performed according to the principles of the NIH Guide for the Care and Use of Laboratory Animals, the provisions of the Animal Welfare Act, PHS Animal Welfare Policy, and the policies of the Houston Methodist Research Institute. Housing and care were provided in accordance with the regulations of the Animal Welfare Act and recommendations of the Guide for the Care and Use of Laboratory Animals. Six-week-old female C57BL/6 mice (Taconic Biosciences) (n=60) were used in this study. Two million Lewis Lung Carcinoma (LLC) cells were suspended in 100 μL of PBS (Cytiva) and injected subcutaneously into the right flank of the mice with an average weight of 18.28 ± 1.68 g. Tumors were grown for 8 days to ~200 mm^3 before GNP treatment.

4.2.2 Chemicals and Reagents

All chemicals were used without further purification. Deionized water was provided by a Millipore Milli-Q Integral 10 Water Purification System (Millipore Sigma).

ICP-OES Chemicals. Acids (HNO_3, HCl) were purchased as trace metal grade (ThermoFisher Scientific). The gold pure standard solution (Au 1000 μg/mL in 10% HCl and 1% HNO_3) was purchased from Perkin Elmer. Yttrium (1000 mg/L) was used as internal standard and purchased from Sigma-Aldrich. Seven standards were prepared to generate a calibration curve for Au content (100 μg [Au]/L, 250 μg [Au]/L, 500 μg [Au]/L, 1000 μg [Au]/L, 2500 μg [Au]/L, 5000 μg [Au]/L, and 10000 μg [Au]/L), as dilutions from the gold pure standard solution. All measurements were performed on triplicate samples (or more when indicated) using a Varian 720-es ICP spectrometer (Agilent). All elemental analyses were performed using the ICP Expert II software (Agilent) by averaging the signal from the 242.794 nm and 267.594 nm emission lines. Each of the samples were filtered using 0.22 μm filters (MilliporeSigma) prior to ICP-OES measurement.

4.2.3 Nanoparticle Synthesis and Characterization

Gold nanoparticles were prepared as previously described[54], [164]. Briefly, gold nanoparticles (~35 nm in diameter) were synthesized by boiling 4.8 mL of 0.039 M aqueous citrate (Sigma-Aldrich) and 7 mL of 0.033 M gold (III) chloride (Sigma-Aldrich) in 600 mL of deionized water until a transition in color from yellow to black occurred, and the colloidal solution appeared dark red. After GNP

synthesis, the pH of the solution was measured to be 3.6. 1 M NaOH solution (Fisher Scientific) was added dropwise to the solution to adjust the pH to 6.0. GNPs were centrifuged at 1500*g* for 5 min in Amicon Ultra-15 100K filters (Sigma-Aldrich). Nanoparticle concentration was measured by ICP-OES and ultraviolet visible (UV−vis) spectroscopy and nanoparticle size was determined by dynamic light scattering (DLS) and scanning transmission electron microscopy (sTEM).

4.2.4 Surface functionalization of concentrated GNPs with PTE

Concentrated GNPs were conjugated to phosphothioethanol (PTE) using thiol chemistry. 1,2-dipalmitoyl-sn-glycero-3-phosphothioethanol (Sodium Salt) also known as 1,2-dihexadecanoyl-sn-glycero-3-phosphothioethanol (sodium salt) (730 Da, 16:0 PTE; Avanti Polar Lipids) was dissolved in 200 proof ethanol (ThermoFisher). The PTE solution (1.45 mg/mL, 118 μL) was added to the GNP solution (18.56 mg/mL, 500 μL) at a ratio of 1 PTE molecule/nm^2 and incubated for 1 h at room temperature to let the ethanol evaporate completely. Once completely evaporated, the ethanol was replaced with the same volume of deionized water (118 μL).

4.2.5 Surface functionalization of concentrated GNPs with PEG

Concentrated GNPs were conjugated to polyethylene glycol (PEG) using thiol chemistry. Poly(ethylene glycol) methyl ether thiol (6000 Da, mPEG-SH; Sigma-Aldrich) was dissolved in deionized water at a concentration of 1.2 mg/mL. The mPEG-SH solution (1.2 mg/mL, 118 μL) was added to the GNP solution (18.56 mg/mL, 500 μL) at a ratio of 1 PEG molecule/nm^2 and incubated for 1 h at room temperature. We estimate a grafting of ~7,750 PEG chains per particle, using a reported grafting density (σ) of 1.55 chains per nm^2 obtained from a multi-Lorentzian-splitting algorithm and proton NMR analytical approach [171].

4.2.6 In Vitro Cytotoxicity and GNP Uptake

LLC and HeLa cells were obtained from the American Type Culture Collection (ATCC). Cell subculturing and GNP-based treatment and procedures have been

previously described[54], [164]. For each cell line, we investigated three groups of GNP treatment (citrate-GNPs, PTE-GNPs, and PEG-GNPs) with two different treatment doses (15 μg [Au]/mL per well and 50 μg [Au]/mL per well). The amount of GNPs internalized by each of these cell lines as well as cell viability after particle treatment were measured in triplicate wells.

MTT Assay for cytotoxicity. Briefly, cells were seeded (4×10^4 cells/well) into 96-well plates (Thermo Fisher Scientific) and allowed to attach overnight. Cells were treated with each of the nanoformulations and incubated for 24 h. 10 μL of MTT Reagent (ATCC) was added to each well and the plate incubated for 2 h or until a purple precipitate appeared. Then, 100 μL of Detergent Reagent for MTT (ATCC) was added to each well to solubilize the purple precipitate for 4 h prior to absorbance measurements at 570 nm and 690 nm using a Synergy™ H4 Hybrid Microplate Reader (BioTek Instruments, Inc.).

ICP-OES quantification of GNP uptake. Briefly, cells were seeded (3×10^5 cells/well) into 6-well plates (Thermo Fisher Scientific) and allowed to attach overnight. Cells were treated with each of the nanoformulations and incubated for 24 h. Cells were washed with sterile 1x PBS (Cytiva), detached with 0.25% trypsin-0.53 mM EDTA solution (Thermo Fisher Scientific), neutralized with complete media, counted with an automated cell counter (Invitrogen) using a solution of 0.4% Trypan Blue (Thermo Fisher Scientific), and pelleted. All collected pellets were digested for 1 h in a 1 mL solution of aqua-regia (1:3 HNO_3 to HCl) and then diluted in 2 mL of acidic solution (10% HCl, 1% HNO_3) for ICP-OES.

sTEM assessments of GNP intracellular internalization. Sample preparation and procedures for electron microscopy were previously reported[172]. Images were obtained using the bright field setting in sTEM mode (FEI Nova NanoSEM 230) under a vacuum of 15 kV.

4.2.7 In Vivo GNP biodistribution

Mice received intratumoral injections of citrate-GNPs, PTE-GNPs, or PEG-GNPs (50 μL, 15 mg [Au]/mL, n = 20 mice/group), once their tumor volumes reached ~200 mm^3. To minimize the possible errors due to the challenges of consistent intratumoral administration and to assure maximum reproducibility, all

injections were performed with an automatic syringe pump (KD Scientific Inc., 0.43 μL/s) while the animals were maintained under anesthesia with isoflurane.

In vivo imaging and intratumoral GNP tracking. In vivo imaging was performed with micro-Computed Tomography (μCT) using a Siemens Inveon Multi-Modality System and an Inveon Acquisition Workplace. Imaging parameters were the following: slice thickness, 103.25 μm; in-plane resolution, 103.25 μm; tube voltage, 80 kV; tube current, 500 μA; exposure time, 240 ms. Baseline images were acquired pre-injection and immediately after injection. Follow-up imaging occurred on days 3 (n = 3 mice/group), 6 (n = 3 mice/group), and 9 (n = 3 mice/group) post-injection of each treatment. Imaging analysis was performed with 3D Slicer (v4.11) on this dataset of acquired images.

Intratumoral GNP content and biodistribution. Biodistribution of the GNPs was determined after intratumoral injection in a mouse model of lung cancer by quantifying the amount of gold in the solid tumor as well as in different organs (liver, spleen, lung, heart, kidneys, brain) and blood using ICP-OES. Mice sacrifice and tissue collection occurred 3 (n = 8 mice/group), 6 (n = 8 mice/group), and 9 (n = 4 mice/group) days post-injection. Blood was collected via cardiac puncture immediately after death and tissues were weighed, flash frozen in liquid nitrogen, and stored at −80 °C for further analysis. For elemental analysis, the whole tissue was digested, except certain tumors on day 3 (n = 4 mice/group) and day 6 (n = 4 mice/group) that were further sub-sectioned. From each of these tumors, 4 dissections were obtained (medial periphery, medial core, lateral periphery, and lateral core), following the previously described approach[55]. Samples were digested as previously described[54]. Briefly, each tissue or blood sample was kept for 1 h in 2 mL of fresh aqua regia at 60 °C until complete digestion, and then diluted in 8 mL of acidic solution (10% HCl, 1% HNO_3). The gold content of each sample was measured and normalized to the injected dose (ID) of the GNPs and expressed as percentage of the ID.

Histopathology. At day 9 post-injection, harvested tumors were fixed in 10% formalin, paraffin embedded, and sectioned. Each section was stained with hematoxylin and eosin (H&E) to evaluate the effects of nanoparticle treatment type on intratumoral zonal distribution. All samples were examined using a bright field microscope (EVOS Cell Imaging System Models, Thermo Fisher Scientific).

4.2.8 Model development

Following intratumoral injection, GNPs in the tumor interstitium diffuse away from the site of injection, while interacting with the ECM and cancer cells. Thus, a fraction of the injected mass of GNPs continues to bind with cancer cells and components of the ECM, while the remaining unbound fraction continues to diffuse away. We describe the spatiotemporal dynamics of the free and bound GNPs with the following partial differential equations (PDEs).

Equation 4.1 for concentration of free GNPs ($\boldsymbol{C_{NP}^{f}(\underline{x}, t)}$):

$$\frac{\partial C_{\mathrm{NP}}^{f}(\underline{x},t)}{\partial t} = \overbrace{D_{\mathrm{NP}} \cdot \nabla^2 C_{\mathrm{NP}}^{f}(\underline{x}, t)}^{\text{Diffusion}} - \overbrace{I(\underline{x}, t)}^{\text{Interaction}} \qquad (4.1)$$

where D_{NP} represents the diffusivity of NPs in tumor interstitium and $I(\underline{x}, t)$ is the NP interaction term that describes the collective rate of interaction of GNPs with cancer cells and components of the ECM and is characterized as a Michaelis-Menten process, such that $I(\underline{x}, t) = I_{\max} \cdot \frac{C_{\mathrm{NP}}^{f}(\underline{x},t)}{K_m + C_{\mathrm{NP}}^{f}(\underline{x},t)}$. Here, $I_{\max}$ is the maximal rate of reaction and K_m is the Michaelis-Menten constant. Note that in our parsimonious model we have ignored advection as a transport mechanism of GNPs due to the occurrence of high interstitial fluid pressure in solid tumors [173].

Equation 4.2 for concentration of bound GNPs ($\boldsymbol{C_{NP}^{b}(\underline{x}, t)}$):

$$\frac{\partial C_{\mathrm{NP}}^{b}(\underline{x},t)}{\partial t} = \overbrace{I(\underline{x}, t)}^{\text{Interaction}} \qquad (4.2)$$

We assume that GNPs once bound cannot unbind, hence the equation for bound NPs only contains the previously defined interaction term.

Numerical solution. To solve the above PDEs, we used a numerical approach known as the finite difference method, for which we assumed a two-dimensional square lattice grid discretized into square elements to calculate the diffusion and interaction of GNPs at discrete time points. The 2D domain has a side $l = 2$ cm and is discretized into 400x400 elements, with each element of side $\Delta = 50$ μm. The tumor is assumed to be a 2D circle located at the center of the domain and has a radius $R_{\mathrm{tum}} = 0.5$ cm. For simplicity, we assume the tumor to be static, i.e., it does not evolve over time. At every time step, the concentration of free and bound GNPs

at a given grid element (i, j) is estimated by the following expressions based on the explicit method:

$$C_{i,j}^{f,\mathrm{t+dt}} = C_{i,j}^{f,\mathrm{t}} + \left(D_{\mathrm{NP}} \frac{\left(C_{i+1,j}^{f,\mathrm{t}} + C_{i-1,j}^{f,\mathrm{t}} + C_{i,j+1}^{f,\mathrm{t}} + C_{i,j-1}^{f,\mathrm{t}} - 4C_{i,j}^{f,\mathrm{t}}\right)}{\Delta^2} - I_{\max} \frac{C_{i,j}^{f,\mathrm{t}}}{K_m + C_{i,j}^{f,\mathrm{t}}} \right) dt \quad (4.3)$$

$$C_{i,j}^{b,\mathrm{t+dt}} = C_{i,j}^{b,\mathrm{t}} + I_{\max} \frac{C_{i,j}^{f,\mathrm{t}}}{K_m + C_{i,j}^{f,\mathrm{t}}} \cdot dt \quad (4.4)$$

where subscripts i and j represent row and column number of a given grid element, respectively, and superscripts f and b indicate free and bound GNPs, respectively. We imposed a Neumann boundary condition at the tumor periphery such that $\frac{\partial C}{\partial x} = 0$, i.e. no flux occurs at the tumor boundary. For the initial conditions, we assumed a concentration of free GNPs C_0 at the site of injection (at a distance $\frac{R_{\mathrm{tum}}}{2}$ from the center of the tumor on its equator), and zero concentration everywhere else. All the simulations were performed in MATLAB R2020b.

Model parameter estimation. One of the key model parameters that we discuss here is referred to as the Damköhler number (D_a), which is a dimensionless number defined as the ratio of rate of reaction to the rate of diffusion of GNPs, such that $D_a = \frac{I_{\max}}{D_{\mathrm{NP}}/R_{\mathrm{tum}}^2}$. It is worth noting that D_a is implicitly divided by a unit concentration to make D_a dimensionless. Since the gold core of the various GNPs investigated in this study have a comparable size (ϕ_{NP}~30 nm), we assumed the same rate of particle diffusion among groups (given that rate of diffusion is a function of particle size as per the Stokes-Einstein equation). However, we hypothesized that due to the difference in surface chemistry of GNPs, the rate of reaction across groups will vary. Hence, to simulate GNPs with different rates of reaction (or $I_{\max}$), we use different D_a numbers. Specifically, we model three different scenarios to compare the simulations to the three types of GNPs investigated in this study, such that $D_a = 0.1$ for highly reactive GNPs, $D_a = 0.01$ for moderately reactive GNPs, and $D_a = 10^{-5}$ for weakly reactive GNPs.

4.2.9 Data and Statistical Analysis

Experimental results are presented as a mean of three replicates (n = 3) ± standard error of the mean (s.e.m). Data were evaluated using a nonparametric two-

way analysis of variance (ANOVA). Subsequent analysis occurred in terms of a Tukey's multiple comparison posthoc test (GraphPad Prism 9 software, USA). Data was considered significant when *$p < 0.05$, **$p < 0.01$, ***$p < 0.001$, and ****$p < 0.0001$.

4.3 Results and Discussion

4.3.1 In vitro uptake of GNPs is governed by their surface chemistry

We synthesized spherical GNPs using the citrate reduction method[174] and surface functionalized them with either lipid bilayers (PTE) or polyether monolayers (PEG), two biocompatible coatings commonly used to mimic biological membranes[175], [176] and improve nanoparticle stealth[177]. 1,2-Dipalmitoyl-sn-glycero-3-phosphothioethanol (16:0 PTE) offers a phospholipid backbone structure with two alkane chain tails but with a modification of the headgroup to include a S–H functionality which allows for stabilizing solid gold particles with a biologically active species. We selected GNPs because they can be visualized both in vitro using electron microscopy[178] and in vivo using micro computed tomography[179] due to their superior x-ray absorption proprieties [180]. Figure 4.1 shows GNPs natively stabilized with citrate or surface passivated with either PTE or PEG using conjugated thiol linkers. The synthesis and characterization of these native nanomaterials have been previously described in detail [54], [121], [164]. Surface chemistry modifications were achieved as described in the methods section 4.2. The resultant solutions appeared deep red in color and contained monodisperse spherical nanoparticles with hydrodynamic diameters of 39.77 ± 2.06 nm, 51.66 ± 0.58 nm, and 56.80 ± 0.55 nm for citrate-GNPs, PTE-GNPs, and PEG-GNPs, respectively. All three surface passivations resulted in negatively charged particles with an observed 3-5 nm shift of their localized surface plasmon resonance due to passivation with either PTE or PEG. All three nanoformulations also displayed concentration dependent x-ray attenuation with signal intensities stronger than that of a standard iodine-based contrast agent, Omnipaque350.

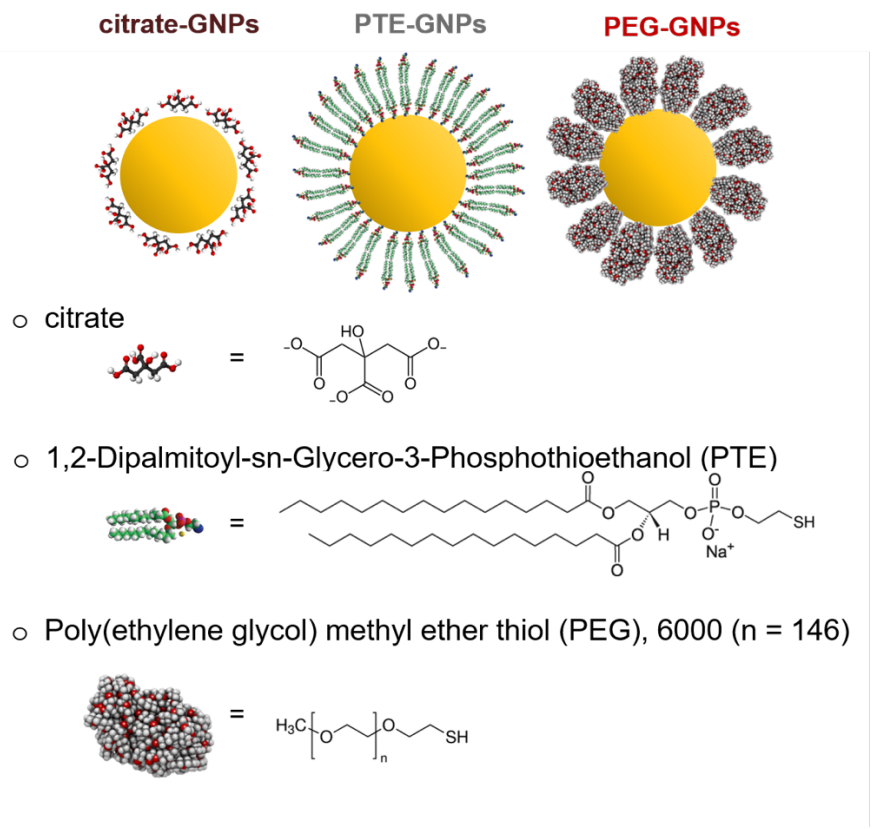

Figure 4.1 Gold nanoparticles (GNPs) surface stabilized natively with citrate and surface passivated with poly(ethylene glycol) methyl ether thiol (PEG) and 1,2-dipalmitoyl-sn-glycero-3-phosphothioethanol (PTE) using conjugated thiol linkers.

In order to determine if the modified surface chemistry of the GNPs affected particle uptake within cancer cells, we performed visualization studies using scanning transmission election microscopy along with elemental analysis to quantify differences in cellular gold content. Cancer cells from established murine (LLC) and human (HeLa) models were treated with each nanoformulation and cultured for 24 hours prior to processing. Citrate passivated particles were more greatly internalized within LLC cells as demonstrated by the large endocytic vesicles containing dark clusters, while particles passivated with PTE and PEG were found to a lesser degree (Figure 4.2A). Evidence of visualization correlated with elemental analysis where the intracellular gold content from citrate-GNPs was similar in both HeLa and LLC cell lines and significantly (**$p < 0.005$) greater than that of the PTE-GNPs and PEG-GNPs (Figure 4.2B,D). Interestingly, PTE-GNPs were more toxic on HeLa cells than LLC cells when compared with their nascent particles (citrate) and PEGylated forms (Figure 4.2C,E). No dose-dependent cytotoxic effect was highlighted in any cell line.

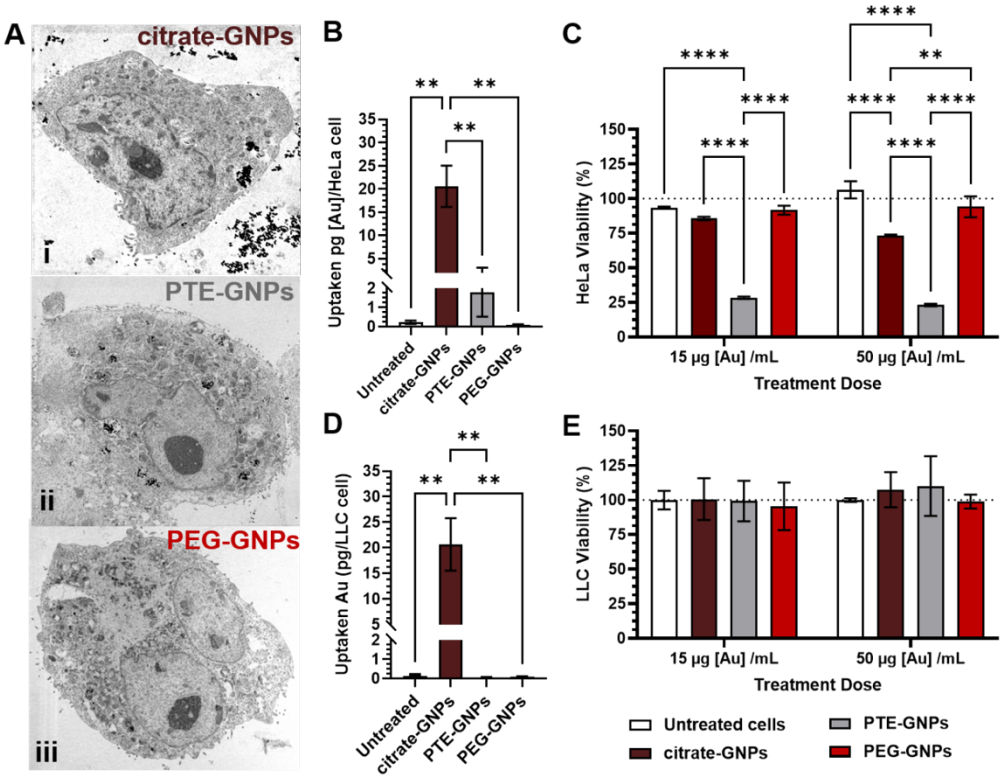

Figure 4.2 GNP uptake is a function of surface passivation which affects cell viability in a cell line dependent manner. (A) Representative scanning transmission election microscopy images of LLC cells demonstrating uptake of (i) citrate-GNPs, (ii) PTE-GNPs, and (iii) PEG-GNPs. Elemental analysis performed with ICP-OES on (B) HeLa and (D) LLC cell pellets 24 h after treatment. MTT assays for (C) HeLa and (E) LLC cells treated and incubated for 24h with nascent and surface functionalized GNPs. (**$p < 0.005$ and ****$p < 0.0001$ by two-way ANOVA using Tukey's multiple comparisons test). All data in the figure are reported as mean ± s.e.m in triplicate.

4.3.2 GNP diffusion patterns are dependent on surface chemistry

Tumors were induced in mice through subcutaneous injection of LLC cells on their flank (see methods) and once the tumor volumes reached ~200 mm^3, baseline images from the tumor bearing animals were obtained with µCT. The animals were intratumorally administered either citrate, PTE, or PEG coated gold nanoparticles via syringe pump, and then imaged again with µCT immediately post-administration (Day 0) as well as on days 3, 6, and 9. Following controlled intratumoral injection, we observed via CT imaging that the citrate-GNPs

consistently agglomerated as single clusters, a phenomenon also reported by our group after manual injection [54], while the PTE-GNPs and PEG-GNPs diffused predominantly in the tumor periphery. In vivo results demonstrated remarkable differences in the intratumoral diffusion of the GNPs depending on the surface passivation. The results are supported by gross inspection of the particles localized to different regions of the tumor (Figure 4.3A), quantification of the amount of intratumoral gold over time with inductively coupled plasma - optical emission spectrometry (ICP-OES) (Figure 4.3B) and tracking GNP localization within the solid tumor using μCT (Figure 4.3C). Interestingly, each surface functionalization presents a different pattern of intratumoral diffusion. In Figure 2D, x-ray attenuation of the nanoparticle treated tumors are reported over time and compared with the tumor baseline signal. Attenuation levels of the tumors after GNP injection demonstrate significant changes between the PTE and PEG passivation 3- and 6-days post-injection (*p = 0.01, *p = 0.03). When comparing with the nascent particles, PTE-GNPs displayed x-ray attenuation similar in intensity, while PEG-GNP attenuation values were significantly lower 6- and 9-days post-injection (#p = 0.03, #p = 0.04). Despite this decrease, the PEG-GNPs still displayed an x-ray attenuation signal ~35% greater than the tumor background 9-days post-injection, demonstrating the capability of these particles to be tracked over time due to their high x-ray absorption properties. Experimental results from elemental analysis (Figure 4.3B) and CT attenuation (Figure 4.3D) significantly correlate using Pearson correlation analysis (p = 0.004). Accumulation of nascent and functionalized GNPs in other organs over time is shown in the Supporting Information. The highest concentration of GNPs was found in both the liver and spleen which offer a high number of extravasation sites. However, less than 10% of the ID was found in these organs without any significant differences between both treatment groups and days. This result confirms the advantages of loco-regional administration in preventing unwanted accumulation of our nanotherapeutic in non-specific sites.

4.3.3 Intratumoral transport modeling of GNPs

Experimental results highlighting the different GNP zonal distributions dependent on particle surface passivation were confirmed through a parsimonious mathematical model of GNP transport following intratumoral injection, adapted from our previous work [170]. Since citrate coated GNPs have the smallest diameter, this nanoformulation can be expected to have the highest diffusivity (as per Stokes-Einstein equation) and thus, the highest intratumoral coverage area. However, as observed in Figure 4.3A,C, the intratumoral coverage area of the

citrate coated GNPs was the lowest, which led us to hypothesize that surface functionalization-induced interaction of NPs with the tumor microenvironment competes with the effects of size-dependent diffusion on NP transport. Thus, the mathematical model was based on reaction-diffusion equations to investigate the relative effect of NP diffusivity and reactivity on the spatiotemporal evolution of GNPs inside the tumor. To characterize the relative strength of reactivity and diffusivity of GNPs, we defined a dimensionless parameter referred to as the Damköhler number (D_a) and tuned it to reproduce the experimental observations qualitatively.

To complement the experimental in vivo timeline (Figure 4.3A,C), snapshots of the tumor mathematical model simulations are presented at days 3, 6, and 9 post-injection (Figure 4.3E). The area coverage of NPs in the tumor domain is indirectly proportional to their Damköhler number (D_a). This indirect relationship suggests that GNPs with a greater rate of reaction to the tumor microenvironment tend to travel the least distance from the site of injection. The simulation results are in good qualitative agreement with the experimental observations for the GNPs, indicating that citrate coated GNPs remain more localized near the site of injection due to their high reactivity ($D_a = 0.1$), unlike the less reactive PTE- ($D_a = 0.01$) and PEG-coated GNPs ($D_a = 10^{-5}$) which distribute more widely across the tumor interstitium, with PEGylated GNPs showing the greatest coverage area. We further confirm this interpretation by quantifying the concentration kinetics of bound and free (unbound) GNPs in the simulations. As shown in Figure 4.3F**,** the concentration of bound GNPs (red curves) around the site of injection (off-centered and set at a distance $\frac{R_{\mathrm{tum}}}{2}$ from the center of the tumor on its equator) follows the order $D_a = 0.1 > D_a = 0.01 > D_a = 10^{-5}$, while the reverse is the case for free GNP concentration (blue curves). The average concentration of unbound GNPs across the tumor diameter tends to decrease over time, with the highest change observed for the highly reactive citrate-GNPs. This indicates that less reactive GNPs can stay as freely diffusing for a longer period, thereby allowing such particles to diffuse farther away from the site of injection in a larger quantity, eventually leading to a more homogeneous particle distribution across the tumor diameter. It can thus be inferred from these numerical experiments that more reactive GNPs tend to distribute less across the tumor interstitium compared to less reactive GNPs, which tend to diffuse more.

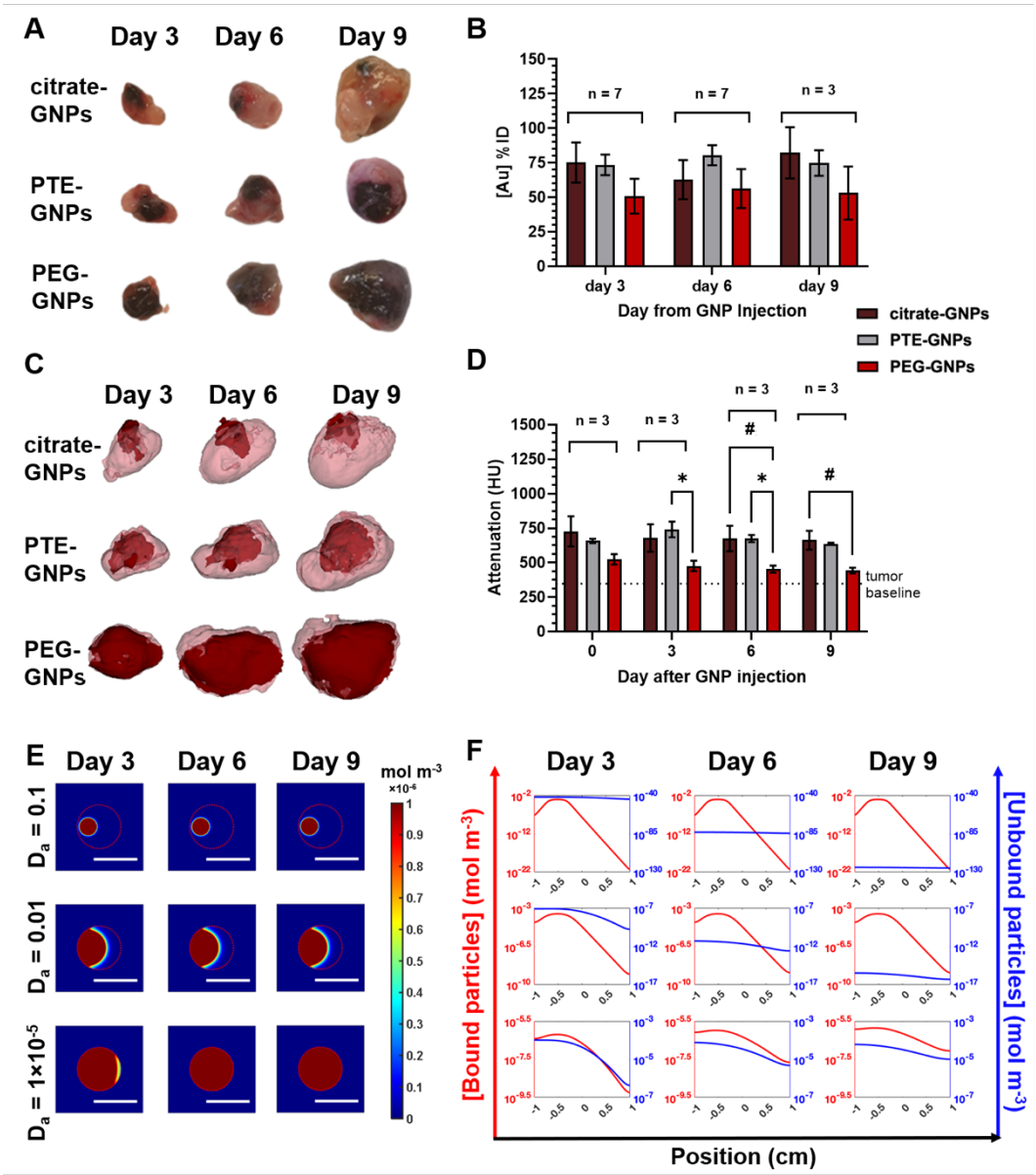

Figure 4.3 GNP intratumoral biodistribution is dependent on surface passivation. (A) Photos of ex vivo tumors harvested 3, 6, and 9 days post-injection show gross evidence of differences in particle distribution. (B) Intratumoral gold quantified with elemental analysis (ICP-OES) 3, 6, and 9 days post-injection. (C) 3D reconstructions of tumors (pink) and particle distribution renderings (red) from μCT. (D) Intratumoral x-ray attenuation in Hounsfield units (HU) show contrast enhancement after injection on days 0, 3, 6, and 9 when compared with tumor baseline (pre-injection) imaging (dashed line, *p <0.05, #p<0.05). Pearson correlation was calculated between (B) ICP-OES and (D) μCT data, identifying agreement between results (††p < 0.005). (E) Snapshots of the tumor model simulations taken at day 3, 6, and 9 post-injection show spatial distribution of the total GNPs (free + bound) for particles with Da values of 0.1, 0.01, and $1x10^{-5}$. These three

values were featured as they qualitatively matched the experimental distribution patterns for the citrate, PTE, and PEG functionalized particles shown in A and C. The dashed white circle demarcates the tumor boundary. Color bar denotes NP concentration (mol m-3). Scale bar = 1 cm. (F) Simulation quantification, where the graphs show the concentration of GNPs across the tumor diameter with -1 being the left edge of the tumor boundary and +1 being the right edge, obtained from model simulations. Red line indicates the concentration of NPs that are bound while the blue line is the concentration of freely diffusing (unbound) NPs in the tumor. Note that the y-axes are in log scale.

4.3.4 GNPs accumulate in different intratumoral zones depending on their surface chemistry

To better quantify GNP zonal accumulation intratumorally, we performed local elemental analysis, sectioning and digesting each section of each tumor separately. As shown in Figure 4.4, we chose to cut the tumors in 4 regions and quantify the gold (n = 4 tumors) 3 and 6 days post-injection. Interestingly, the data not only confirms differences between groups treated with functionalized and nascent particles but also demonstrates that PTE- and PEG-GNPs accumulate to a greater degree in the lateral periphery over 3 days when compared with the citrate-GNPs.

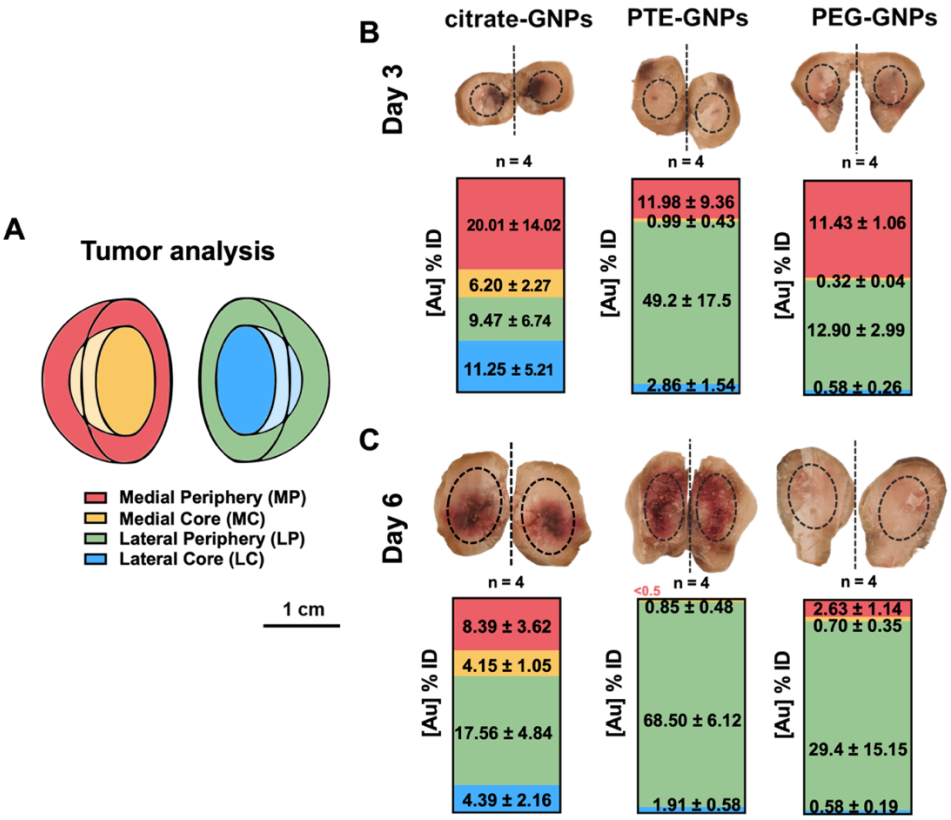

Figure 4.4 Intratumoral quantification of particle zonal accumulation. (A) Schematic of methodology whereby the tumor was sectioned into 4 regions. Quantification of gold performed with elemental analysis on n = 4 tumors (B) 3 and (C) 6 days post-injection. Not visible areas in the boxes represent values of gold <0.5 %.

4.3.5 The histopathological profile of GNP intratumoral diffusion is dependent on particle surface chemistry

The consistently observed zonal distribution pattern delineated between nanoformulation groups was also highlighted by histopathology (Figure 4.5). Solid tumor nodules were identified in the mice both visually and with µCT (Figure 4.5A-D), harvested and photographed (Figure 4.5E-H) and stained with hematoxylin and eosin (H&E, Figure 4.5I-L). For comparison across the different treatment groups, we show a representative 2D central slice at 20x magnification which revealed dense tumor growth within the fibroadipose tissue. The tumors consist of numerous

irregular nuclei with frequent mitotic figures. In the untreated group, the tumors were highly viable and mitotically active with only rare small foci of apoptosis. The treatment groups showed a border zone (Figure 4.5J-K white arrow) with distinct areas of viable tumor bordering areas of tumor necrosis (smaller foci). Interestingly, the patterns of necrosis in the treated animals were similar to the GNP diffusion patterns. The citrate-GNPs were primarily aggregated in the tumor center along with observed necrosis, the PTE-GNPs consisted of multiple clusters throughout similar to the necrosis pattern, and the PEG-GNPs concentrated at the tumor periphery where necrosis was found along with extension of the particles into the surrounding soft tissues. Surprisingly, while all the nanoformulations originate from the same material, only the PEG-GNPs traveled across the tumor boundary and into the surrounding stromal cells, demonstrating access to a secondary target region. While most researchers focus on outside-in drug delivery and overcoming the stromal boundary to penetrate into the tumor, these results show an inside-out directed delivery into the surrounding stromal cells, which supports and maintains the integrity of the tumor mass, thereby making it an important region to target.

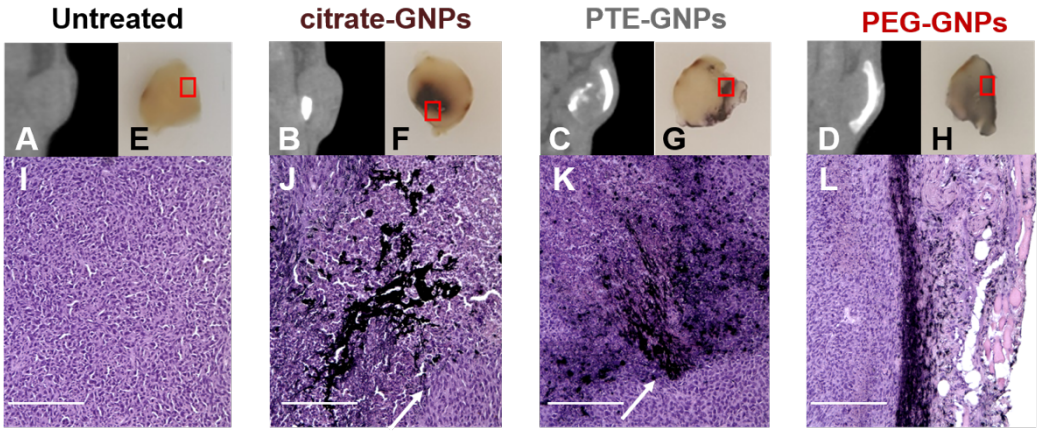

Figure 4.5 Effects of GNP treatment type on intratumoral zonal distribution. Groups include untreated, citrate-GNPs, PTE-GNPs, and PEG-GNPs treated tumor bearing mice. (A-D) In vivo CT slices of the tumors grown on the mouse flank, (E-H) ex vivo photos of the excised tumors sliced on a plane close to the injection point, and (I-L) H&E stain of the tumors (red boxes in E-H represent the area shown with 20x magnification in I-L, white arrows in J-K represent border zone between viable and necrotic tumor). Scale bar represents 200 μm.

4.4 Conclusions

We investigated GNP interactions with the tumor microenvironment for nascent particles as well as particles surface passivated with lipid bilayers (PTE) and polyether monolayers (PEG). We discovered in vivo different zone-specific patterns of particle accumulation in the tumor dependent on surface functionalization using a murine model of lung cancer. To better identify an underlying mechanism of how surface functionalization affects particle distribution after local injection, we modeled their intratumoral transport with reaction-diffusion equations and, ultimately, predicted the spatiotemporal evolution of GNPs. Using our parsimonious modeling approach, we demonstrated the mechanistic basis for the effect of surface functionalization on intratumoral GNP transport that has implications for drug delivery and treatment outcome. While the model assumed simplifications such as a non-growing tumor and the absence of advection, these assumptions do not necessarily impact the qualitative nature of our results. Importantly, we demonstrate that the characterization of GNPs using the Damköhler number (D_a) can be a valuable means to understand the impact of GNP properties on their transport behavior. While D_a values were arbitrarily chosen as a proof of concept in the current study, future in vitro experiments can provide the necessary values of reaction rates to calculate D_a and prospectively predict the expected intratumoral behavior of GNPs.

For the field of cancer nanomedicine, there are several fundamental and applied research directions that can be considered. From an applied perspective, a mathematical framework that allows for particle distribution predictions based on surface properties could revolutionize the current methods of personalized medicine. Several applications have been identified in the last decade for gold nanoparticles in cancer treatment. They can be used as cargo for chemotherapeutics, mediators for photothermal therapy, and as contrast agents for imaging, helping to track tumor size and determine molecular signatures. However, these applications have been limited by the poor and heterogeneous accumulation of GNPs within tumor tissues. For this reason, mathematical simulations and in silico approaches may help optimize a combination of surface properties to better intratumorally deliver a nanotherapeutic to a targeted region of the tumor.

We used reaction-diffusion equations to model the intratumoral transport of nanoparticles and observed that the transport behavior of particles with high reactivity (greater Damköhler number) resulted in greater distribution across the tumor, while those with low reactivity remained localized. Using a reproducible

intratumoral delivery approach (constant injection rate), we experimentally observed that changes in particle surface passivation affected transport behavior and resulted in remarkably different distribution patterns within the TME as assessed through different modalities (imaging, elemental analysis, and histology). Overall, the PEG functionalized GNPs consistently diffused in the tumor periphery and resulted in the greatest tumoral surface coverage, permeating beyond the cancer cells and into the stroma. As the stroma is known to play a role in promoting tumor development and metastasis, permeation into this region allows for access across the tumor-stroma barrier for therapeutic targeting. Finally, since the stroma (typically not targeted by standard anticancer therapies) can induce therapeutic resistance, its role in disease progression should not be overlooked, and identifying methods to target and deliver drugs into this region as well as other zones within the TME would offer a more comprehensive and integrative treatment approach.

Chapter 5

Hyaluronate-Thiol Passivation Enhances Gold Nanoparticle Peritumoral Distribution When Administered Intratumorally in Lung Cancer

5.1 Introduction

Tumor targetability and site-specific release are considered the most critical factors in cancer diagnostics and therapy. To date, local chemotherapeutic and immunotherapeutic drug delivery has demonstrated superior efficacy and safety compared to systemic administration in murine models of cancer [181]–[183]. When a drug is retained within the tumor microenvironment (TME) at high concentrations, its local therapeutic effect is enhanced and any off-target side effects due to systemic exposure are minimized [184]–[186]. Unfortunately, local intratumoral injection of free anticancer agents into solid tumors can be compromised by their leaky vasculature [187] and elevated interstitial fluid pressure [188], which leads to rapid escape of the drug from the tumor confinement and can contribute to reduced sensitivity to therapy [189], [190] or primary resistance [191].

To overcome these challenges, more investigations are needed to identify novel successful strategies for site-directed drug localization within a solid tumor to target and understand the body's response toward the introduced material [192]. In this context, gold nanoparticles (GNPs) have been investigated as anti-cancer drug cargo carriers, whereby their anti-angiogenic and photothermal properties can be used to potentialize drug action [193], [194], and their diffusive nature exploited for multimodal synergistic diagnosis and therapy [195], [196]. However, uniform intratumoral distribution of these particles with tumor site-specificity and retained accumulation has not yet been achieved according to some recent pre-clinical studies [197], [198].

Evaluating the tumoral distribution of a drug or particle-drug conjugate is an important variable that is often neglected, as most drugs are assumed to distribute homogeneously into a tumor [199]. In previous studies, we demonstrate that GNP cellular uptake [56], [200], as well as intratumoral distribution and retention [201], [202], is strongly influenced by surface chemistry. We have shown that when GNPs are surface passivated with a bovine serum albumin (BSA) protein layer, internalization of the particles into cancer cells occurs through larger vesicle formation with reduced gold content per cell, and when injected intratumorally in a murine lung cancer model, the BSA passivated particles diffuse more overtime throughout the tumor tissue [201]. BSA modification shields the metal core and prevents unwanted non-specific adsorption of other agents onto the particles.

However, while BSA is inexpensive, easily accessible, and provides a model substrate, its passivation is non-uniform, there is a possibility for other proteins to overcoat the BSA, and it does not bind with high specificity to a receptor target expressed on cancer cells [203]. Compared to passive targeting, active targeting of GNPs is a promising strategy for nanoparticle-mediated drug delivery since it relies on a biological interaction between ligands on the GNP surface and receptors on the targeted cancer cell [204]. Nevertheless, when the GNP surface is functionalized with targeting ligands, such as proteins, peptides, polysaccharides, apatmers, or small molecules, the consequences of the corona must be considered. In fact, non-specific interactions between engineered nanomaterials and the biological microenvironment of the tumor lead to unwanted adsorption of molecules which can mask or displace the conjugated ligands on the GNP surface. Further, uncontrolled or unmonitored changes in nanoscale structure, chemical composition, or molecular conformation may dramatically affect physiological response to a pharmaceutical or nanoscale device [205]. In a biological context, this effect is identified as *biofouling,* and it leads to the loss of targeting affinity of GNPs or in a worst-case scenario, redirects the complexes to other undesired sites [206], [207]. Therefore, innovative anti-biofouling strategies must be investigated when a novel diagnostic and/or therapeutic approach is proposed for cancer applications.

In this study, we investigate the effects of GNP surface passivation with hyaluronate on particle intratumoral distribution in solid lung carcinoma. Hyaluronate or hyaluronic acid (HA) is a negatively charged, non-sulfated, linear biopolymer composed of alternatingly linked saccharide units of glucuronic acid and N-acetylglucosamine [208]. HA is a naturally produced biocompatible material since it is an essential component of the extracellular matrix [209]. It is found abundantly in skin [210], cartilage [211], synovial fluid [212], and interstitial fluids [213], and is naturally biodegradable. To date, it is used in clinical settings as an injectable hydrogel [214] and biological scaffold [215] in different tissue engineering applications, such as for dermatological fillers and osteoarthritis treatment [216].

HA is the principle ligand of the Cluster of Differentiation 44 (CD44) receptor, which is a glycoprotein expressed at low levels on the surface of hematopoietic and epithelial mammalian cells [217], but overexpressed in many tumor cells, including several non-small cell lung cancers [218]. Moreover, HA is a versatile compound since it offers multiple sites for chemical modification, and it has been previously reported to prevent undesired protein corona formation on the nanomaterial's surface [219]. In fact, if chemically modified with a thiol (-SH) functional group,

forming a hyaluronate-thiol complex (HA-SH), it can covalently bind to the surface of the GNPs, improving upon their stealth behavior as well as their targeting specificity for CD44 receptors [220].

The aforementioned characteristics as well as its high viscoelasticity and potential for chemical modifications to the backbone structure, all make HA an ideal candidate for anti-cancer applications involving engineered gold-based nanomaterials [221]. Many research works present different synthesis processes of HA-GNP complexes [222] as well as their in vitro testing as drug carriers for photothermal cytotoxic drug release in cancer cells [223]. We identified certain studies involving pre-clinical cancer models, however the HA coated GNPs are only administered systemically, and biodistribution is not evaluated [224]–[227]. Only a few studies assess HA-GNP distribution in various pre-clinical models, such as the porcine eye, as HA is a widely used excipient in ocular drug delivery, and rodent skin, as HA has the ability to stimulate fibrin development in the wound healing process. For instance, Apaolaza et al. [228] immobilized low molecular weight HA (5 kDa) on the surface of GNPs and visually observed that HA passivation promoted enhanced particle distribution across the vitreous matrix and ocular tissues after local injection in *ex vivo* porcine eyes. Sonntag et al. [229] also conjugated thiolated HA to GNPs of various sizes (5, 60, 80, and 120 nm) and quantified their distribution in the anterior chamber of the eye in an ex vivo porcine model. The authors found that the HA coating prevented aggregation of NPs inside the trabecular meshwork and yielded reduced gold content in off-target tissues in the anterior eye, such as the cornea, lens, iris, and ciliary body. Mendes et al. [230] performed a visual analysis of the wound area contraction in the skin of rats after daily topical application of GNPs electrostatically functionalized with HA followed by laser irradiation for 7 days, demonstrating a decrease in inflammatory infiltrate and an increase in wound contraction post-photobiomodulation treatment. While these studies all illustrate that HA coated GNPs can show improved tissue targeting and efficacy, to our knowledge, there is no single pre-clinical study which evaluates and quantifies the intratumoral distribution of HA-GNPs. Therefore, after confirming successful surface modification and demonstrating their anti-biofouling properties in plasma and cancerous cells, we exploit elemental analysis to quantify site-specific HA-GNP accumulation in different tumor regions following local particle administration in vivo. As the TME is notoriously complex and solid tumors can be considered “abnormal organs” composed of multiple cell types [231], identifying nanoparticle localization within particular tumor zones could be used to improve drug delivery to specific cell types that direct and influence cancer growth and progression.

5.2 Materials and Methods

5.2.1 Gold Nanoparticles Synthesis

GNPs synthesis was achieved by combining 7 mL of 0.033 M gold (III) chloride (Sigma, St. Louis, MO, USA, 379948) and 4.8 mL of 0.039 M aqueous citrate (Sigma, St. Louis, MO, USA, C3674) into an Erlenmeyer flask containing 600 mL of boiling Milli-Q water, following a previously reported approach [200]. The dark-red colloidal solution obtained from this process was allowed to equilibrate to room temperature for 24 h. Once cooled, the pH of the solution was measured using a benchtop pH meter (Accumet AE150, Fisher Scientific, Hampton, NH, USA). After synthesis, the GNPs have a native acidic pH due to their stabilization with citric acid (pH = 3.6). We previously demonstrated that in this condition, the particles lose their stability when immersed in biological media [201]. To increase particle stability, the pH of the solution was adjusted to 6.0 through dropwise addition of a 1 M NaOH solution. The GNPs were concentrated and washed by centrifuging 15 mL of the solution (pH = 6.0) at 1500 × g for 5 min in Amicon Ultra-15 100K filters (Sigma-Aldrich, St. Louis, MO, USA, UFC910008) using an Eppendorf Centrifuge 5810R (Hamburg, Germany), and the pellet was then resuspended in 1 mL Milli-Q water at pH = 6.0. This process was performed to remove any excess citrate that may impair the hyaluronate-thiol surface functionalization. Prior to centrifugation, the stability of the colloidal gold was assessed through visual inspection of the solution along with UV-VIS spectroscopy.

5.2.2 Surface Passivation of the Gold Nanoparticles with Hyaluronate-Thiol

For surface passivation of the GNPs with hyaluronate-thiol, HA-SH powder 10 kDa (Nanosoft Polymers Winston-Salem, NC, USA, Lot#246561003) was used in this study, following the protocol described by Lee et al. [232]. HA-SH solution (5 mg/mL) was prepared by mixing 5 mg of HA-SH powder in 1 mL Milli-Q water until complete dissolution. Next, 0.004 mL of the HA-SH solution was added to 1 mL of the washed GNP solution (obtained as described in section 5.2.1) and the solution vortexed. UV-VIS spectra were acquired after 1 and 24 h to check particle

stability and assess changes in the surface plasmon resonance (SPR). The solution was stored at room temperature.

5.2.3 GNP Characterization

After synthesis, HA-GNP stability was assessed though visual inspection (whereby no macro-aggregation or flocculation was observed, as well as no changes in the dark-red color of the solution). The optical properties as well as the morphology of the HA-GNPs were evaluated using UV-VIS spectroscopy and scanning electron microscopy (SEM). Particle morphology was assessed using a FEI Nova NanoSEM 230 (FEI Co., Hillsboro, Oregon, USA). Changes in surface chemistry and opsonization/antifouling properties were evaluated with dynamic light scattering and ζ-potential.

5.2.4 Ultraviolet-Visible (UV-VIS) Spectroscopy

For all the samples, absorbance spectra were obtained on a Beckman-Coulter UV-VIS (200–1000 nm) spectrophotometer (DU 730, Beckman Coulter, Inc., Brea, CA, USA). Low concentrations of sample (< 1 mg/mL) were used in 1 mL volumes by combining a 1:1 ratio of particles in Milli-Q at pH 6.0 with either PBS (1× phosphate buffered saline at pH 7.4, Thermo Fisher Scientific, Waltham, MA, USA, SH30256FS) or plasma (at a measured pH 7.4), following a blank measurement with Milli-Q water.

5.2.5 Dynamic Light Scattering (DLS) and ζ-Potential

To confirm passivation, assess surface charge, and test colloidal stability as well as the antifouling properties of the GNPs in a biological medium, dynamic light scattering and ζ-potential measurements were conducted on the samples prepared as described in 5.2.4. Particle size (hydrodynamic diameter), polydispersity index (PDI), and surface charge (ζ-potential) after synthesis and passivation with HA was performed in Milli-Q water, PBS, and blood plasma using a Zetasizer Nano ZS (Malvern Panalytical, MA, USA). Particle size was measured using a standard cubic cuvette, while surface charge (ζ-potential) was obtained

using a dip cell ZEN1002. In both analyses, low sample concentration (< 1 mg/mL) was used in a 1 mL volume. All of the measurements were conducted at room temperature. Whole blood from healthy porcine (Male Castrated Domestic Pigs, ~66 kg, Oak Hill Genetics, Ewing, IL, USA) following an approved protocol by the Institutional Animal Care and Use Committee (IACUC) at the Houston Methodist Research Institute (IS00005819 approved 26 March 2021) was collected in Buffer K2 EDTA blood collection tubes (BD Vacutainer, Franklin Lakes, NJ, USA, 367861) and centrifuged for at least 15 min at 1200 × g.

5.2.5 Cell Line and Passaging

HeLa cells derived from human cervical cancer (ATCC®, Manassas, VA, USA, ATCC® CCL-2) were grown in T-75 flasks using Eagle's minimum essential medium (EMEM) supplemented with 10% fetal bovine serum (FBS, USDA approved, ATCC®, Manassas, VA, USA) and incubated at 37 °C and 5% humidity in a HERAcell 150i CO2 incubator (Thermo Fisher Scientific, Waltham, MA, USA). To expand and passage the cell line, the cells were first washed with sterile 1x PBS and then 0.25% trypsin-0.53 mM EDTA solution (Thermo Fisher Scientific, Waltham, MA, USA, 25-200-056) was added to the flask in a sterile field to dissociate the cells from the flask and each other. After placing in the cell culture incubator for 5 minutes, the cell suspension was neutralized with complete growth media. The suspension was then centrifuged at 130 × g for 5 min, the supernatant discarded, and the pellet containing living cells resuspended in at least 1 mL of complete growth media. Final cell concentration was obtained using a Countess™ II FL Automated Cell Counter (Invitrogen, Carlsbad, CA, USA).

5.2.6 MTT Assay for Cell Viability due to Metabolic Activity

Viability related to cell proliferation and metabolic activity after nanoparticle treatment was evaluated through reduction of 3-(4,5-dimethylthiazolyl-2)-2,5-diphenyltetrazolium bromide (MTT) to the blue product formazan, assessed using spectroscopy. HeLa cells were seeded into 96-well plates (Corning™ Costar™ 96-Well, Cell Culture-Treated, Flat-Bottom Microplate, Thermo Fisher Scientific, Waltham, MA, USA, 15250061) at a concentration density of $1x10^5$ cells/mL and allowed to incubate for 24 h. It has been previously shown that the administration method of coated GNPs in cell culture can affect particle interaction with cells, such

as macrophages, while colloidal stability is independent of administration method, and pre-mixing the GNP solution in complete cell culture media prior to cell exposure is the best method tested to date [233]. Therefore, after the cell attachment incubation period, conditioned media was replaced with fresh complete media in which the GNP treatment was pre-mixed to avoid unwanted particle deposition. Triplicate wells containing only media and each of the GNP test treatments (wells without cells) were used as controls to remove any background signal. Two different GNP treatment concentrations were investigated: 15 μg [Au]/mL per well and 50 μg [Au]/mL per well. After 24 h of HeLa cell incubation with each of the GNP treatments, 10 μL of MTT Reagent (ATCC®, American Type Culture Collection, Manassas, VA, USA) was added and mixed to each well, including the wells without cells, and the samples placed back in the cell culture incubator for approximately 2 hours. Once the purple precipitate was clearly visible under the microscope (Nikon ECLIPSE Ts2 Inverted Microscope, Nikon Instruments Inc., Melville, NY, USA), 100 μL of Detergent Reagent (ATCC®, American Type Culture Collection, Manassas, VA, USA) was added at room temperature to each well to dissolve the formazan and create a homogeneous dark colored solution. Absorbance of this solution in each well was measured using a Synergy™ H4 Hybrid Microplate Reader (BioTek Instruments, Inc., Winooski, VT, USA) at 570 nm and 690 nm.

5.2.7 Trypan Blue Assay for Cell Viability

Viability related to cell membrane integrity was performed using a Trypan blue assay. Trypan blue enters the cells with compromised membranes and stains the dead cells blue. The total number of viable and dead cells were obtained after each GNP treatment (citrate-GNPs or HA-GNPs) and compared with a negative control (untreated cells). To perform this assay, HeLa cells were seeded in 6-well plates (Corning™ Costar™ Clear 6-Well Plate, Thermo Fisher Scientific, Waltham, MA, USA, 07201588) at a concentration density of $1x10^5$ cells/mL per well and placed in the cell culture incubator for attachment and growth for 24 h. The media was then replaced with fresh complete media in which the GNP treatments (50 μg [Au]/mL per well) were pre-mixed to avoid unwanted particle deposition. Each treatment (citrate-GNPs at 50 μg [Au]/mL per well, HA-GNPs at 50 μg [Au]/mL per well, or media replacement without GNP) was administered to triplicate wells, and the samples placed in the cell culture incubator for 24 h. After incubation, 0.4% Trypan Blue Solution (Thermo Fisher Scientific, Waltham, MA, USA, 15250061)

was used to differentiate between living and dead cells (1% of the cell volume collected from each well was evaluated) and the cells counted using a Countess™ II FL Automated Cell Counter (Invitrogen, Carlsbad, CA, USA). The pellet (99% of the cell volume collected from each well) was used for inductively coupled plasma optical emission spectrometry (ICP-OES) analysis.

5.2.8 Elemental Analysis to Quantify Intracellular GNP Uptake

Inductively coupled plasma optical emission spectrometry (ICP-OES) was used for all of the elemental analysis performed in this study. Standard curves for calibration of Au content were created using 7 different standard concentrations: 100 μg [Au]/L, 250 μg [Au]/L, 500 μg [Au]/L, 1000 μg [Au]/L, 2500 μg [Au]/L, 5000 μg [Au]/L, and 10000 μg [Au]/L. Each standard was prepared by serial diluting a gold standard (Au 1000 μg/mL, Perkin Elmer, Waltham, MA, USA, N9303759) in an acidic solution containing 10% trace metal grade hydrochloric acid (HCl, Thermo Fisher Scientific, Waltham, MA, USA) and 1% trace metal grade nitric acid (HNO_3, Thermo Fisher Scientific, Waltham, MA, USA).

To quantify the cellular uptake of the HA-GNPs and compare with the uptake of the native particles, cell pellets (as described in section 5.2.7) were digested in a chemical fume hood using a 1 mL solution of aqua-regia (1:3 nitric acid to hydrochloric acid) for 1 h and then diluted in acidic solution (10% HCl, 1% HNO_3). To avoid any clogs in the tubing systems of the ICP-OES hardware, each sample was filtered prior to analysis using 0.6 μm filters (MilliporeSigma™, Burlington, MA, USA, Steriflip Quick Release-GP Sterile Vacuum Filtration System). All measurements were performed on triplicate samples using a Varian Agilent 720-es ICP spectrometer (Agilent, Santa Clara, CA, USA), and the results were obtained by averaging the signal from two gold emission lines (242.794 nm and 267.594 nm) using the ICP Expert II software. The gold content found in each pellet was normalized to the total number of counted cells (dead and alive). With this normalization, we assume that nanoparticle internalization is homogenous across the cells.

5.2.9 Animal Model of Lung Cancer

Six-week-old female C57BL/6 mice (n = 20) were used in this study to evaluate and quantify site-specific diffusion of the GNPs as a function of their surface chemistry. The research protocol was granted Institutional Animal Care and Use Committee (IACUC) approval (protocol # IS00005178 approved 6 May 2019) at the Houston Methodist Research Institute. The animals were purchased from Taconic Biosciences (Rensselaer, NY, USA). Female mice were chosen for study because while both naive male and female C57BL/6 mice do not present lung function differences at baseline [234], tumors grow more rapidly in female C57BL/6 mice [235]. In addition, to date, worldwide statistics indicate biological sex differences in human lung cancer, with higher lung cancer incidence rates for women [236]. A Lewis lung carcinoma (LLC) cell line was used in this study as a murine model of non-small cell lung cancer (NSCLC), since it is highly tumorigenic and provides a reproducible syngeneic model for lung cancer in the C57BL mouse [237]–[239].

5.2.10 Experimental Timeline

Under sedation, all mice (n = 20, average weight of 18.8 ± 1.3 g) received manual subcutaneous injection of 2×10^6 LLC cells into their right flank. Tumors were palpable 4-5 days after cell injection, and after 10 days, tumor volumes reached an average of ~100 mm^3. 10 days post tumor cell inoculation, GNPs (citrate-GNPs: 50 μL, 10 mg/mL, n = 10 or HA-GNPs: 50 μL, 10 mg/mL, n = 10) were intratumorally injected using insulin syringes (BD U 100 Insulin Syringe Micro Fine Needle 28G, Becton, Dickinson and Company, Franklin Lakes, NJ, USA, 329461) with a syringe pump (KD Scientific Inc., Holliston, MA, USA, Model 100) set at a slow rate (0.43 μL/s) and 50 μL dispense volume. We previously demonstrated that automatic injections in small rodents can reduce the variability and error introduced by manual injections of nanoparticles [201]. In addition, we consistently injected the particles in the same region of the tumor (the core) for each animal. Mice weight and health conditions were monitored daily, ensuring adequate nutrients (food and water ad lib.) and living conditions (clean cages, enrichment). Tumor volumes were also measured daily using a digital caliper (McMaster-Carr, Elmhurst, IL, USA, 2340A11). All animal procedures involving injections were performed by anesthetizing the mice with isoflurane. The animals were sacrificed 3 days (n = 5 for each group) and 6 days (n = 5 for each group) post-intratumoral

injection of each GNP treatment. Tumors were excised, weighed ex vivo, flash frozen in liquid nitrogen, and stored at −80 °C for further analysis (see section 5.5.11.). During the necropsy, pictures of the tumor orientation and injection site were taken to keep track of the relative spatial location in reference to the mouse body, allowing for the creation of orientation maps during analysis. Blood was collected by cardiac puncture immediately after death, and the brain, heart, lung, liver, spleen, and kidneys were harvested and digested for elemental analysis. For sample digestion, each organ tissue or blood sample was immersed in 2 mL of fresh aqua regia, heated at 60 °C for 1 h until complete digestion, and resuspended in a 10 mL acid solution composed of 1% nitric acid and 10% hydrochloric acid. Each sample was filtered using 0.22 μm filters (MilliporeSigma™, Burlington, MA, USA, Z359904) prior to ICP-OES measurement. Gold concentration was determined following the same protocol as described above.

5.2.11 Site-specific Intratumoral Distribution of GNP: Elemental Analysis

Frozen tumors were sectioned using a surgical blade to divide the medial and lateral sides in reference to the mouse body. All the dissection procedures were performed by the same investigator (R.T.) for consistency. From each side (medial and lateral), the core was separated from the tumor periphery with a surgical blade. Hypothesizing the tumor volume as a sphere of radius R in a spherical coordinate system, we define the core as an internal sphere with Euclidean distance from the origin O to R/2, and the periphery as the external shell of the tumor with Euclidean distance from R/2 to R. We also established that the origin O coincides the site of injection (see section 5.2.9). Therefore, from each tumor, 4 sections were obtained, representing the i) medial peritumor (MP), ii) medial core (MC), iii) lateral core (LC), and iv) lateral peritumor (LP) as shown in Figure 5.3A. The procedure was performed while the sample remained frozen to avoid any unwanted dispersion of fluids and increase the precision of the dissection procedure. Each section was digested for elemental analysis to determine any site-specific accumulation of gold dependent on the surface chemistry. For sample digestion, tissues were immersed in 2 mL of fresh aqua regia, heated at 60 °C for 1 h until complete digestion, and resuspended in acid solution composed of 1% nitric acid and 10% hydrochloric acid. Each sample was filtered using 0.22 μm filters (MilliporeSigma™, Burlington, MA, USA, Z359904) prior to ICP-OES measurement. Gold concentration was determined following the same protocol as described above.

5.2.12 Statistical Analysis

All statistical analyses and graphs were obtained with GraphPad Prism (version 9.1.0; GraphPad Software, Inc., San Diego, CA, USA). Mean ± s.e.m. values were calculated and plotted in the results. Statistical significance was assessed by two-way analysis of variance (ANOVA) with Tukey's multiple comparisons test as the post-hoc test method, and multiple unpaired t test.

5.3 Results

5.3.1 GNP characterization

In this study, we synthesized spherical GNPs with the citrate reduction method and surface passivated them with hyaluronate-thiol. We previously demonstrated that nanoparticles produced using this synthesis protocol generate a strong surface plasmon resonance peak and prominent X-ray attenuation, useful in nanotheranostic applications [201]. Surface plasmon resonances occur in metal nanostructures at frequencies governed by the material's properties and geometry [240]–[245], and spectral shifts can be indicative of changes in the local refractive index, such as the presence of a nearby molecule [246]. The schematic in Figure 5.1A illustrates the molecular interaction and surface chemistry of GNPs stabilized with citrate or thiol-modified hyaluronic acid. Figure 5.1B shows the absorbance spectra of the citrate-GNPs and HA-GNPs in water at pH 6.0. There is an observed 2 nm red-shift in the SPR peak (from 530 nm to 532 nm) of the GNPs due to a change in refractive index when the particles are passivated with thiol-modified hyaluronic acid. When the solvent of the media is changed to either PBS (Figure 5.1C) or plasma (Figure 5.1D), both of which are at a pH of 7.4 and above the pKa values of citric acid ($pKa_1 = 3.13$, $pKa_2 = 4.76$, and $pKa_3 = 6.39$)[247], the intensity of the single particle plasmon at ~530 nm decreases, evident of signs of aggregation and particle instability. Interestingly, in both solvents (PBS and plasma), the HA-GNPs show improved stability over the nascent particles indicated by the higher absorbance values around 530 nm. Figure 1E depicts a SEM image, representative of the particles after synthesis, demonstrating their spherical morphology, as well as photographs of the prepared solutions, highlighting their uniform dark red color. The similarity in red color for both surface functionalizations in water at pH 6.0 is

indicative of their colloidal stability at this condition as no sample macro-aggregation or flocculation was observed due to passivation. To assess the anti-biofouling properties of the HA-GNPs and compare them with the citrate-GNPs in a simulated physiological environment, changes in hydrodynamic diameter as well as surface charge of the particles were measured after resuspending them in either water, PBS, or plasma. Rather than using SEM, which can only provide an estimation of the projected area of the particle, dynamic light scattering offers information of the hydrodynamic diameter of the inorganic core along with any coating material and solvent layer attached to the particle as it moves under the influence of Brownian motion. Therefore, we present dynamic light scattering measurements rather than estimate size using electron microscopy since it can be obtained in solution and provides a deeper understanding of the surface chemistry, which is crucial for optimizing GNP performance in biological assays and to predict particle migration and biodistribution [248]. As demonstrated in Figure 5.1F, the hydrodynamic diameter of the citrate-GNPs and HA-GNPs does not significantly differ when dispersed in water at pH 6.0, although the average hydrodynamic size of HA-GNPs increases slightly as a result of the HA coating. However, when immersed in a media with properties similar to that of a biological environment (either PBS for physiological pH or blood plasma as source of physiological pH and proteins), both the citrate-GNPs and HA-GNPs increase in size when compared to that obtained in Milli-Q water. Significant differences are highlighted (t test unpaired) between the citrate-GNPs and HA-GNPs dispersed in PBS and plasma (****$p < 0.0005$). Importantly, the increase in hydrodynamic diameter for the HA-GNPs in both media is significantly less than that of the nascent particles, which is consistent with the absorbance spectra in Figure 5.1C, D and indicative of particle clustering in the slightly basic media. Further, the fact that the HA-GNPs do not show such drastic changes in diameter is evidence that the HA coating is shielding the particles and providing anti-biofouling properties. For the citrate-GNPs, the average polydispersity indices were 0.32 (water), 0.23 (PBS), and 0.54 (plasma), while for the HA-GNPs, the average of polydispersity indices were 0.32 (water), 0.21 (PBS), and 0.57 (plasma). The increase in polydispersity in PBS and plasma for the nascent particles is also indicative of particle clustering due to instability. Zeta potential measurements can also provide insights into particle stability. The zeta potential of the citrate-GNPs and the HA-GNPs dispersed in Milli-Q water, PBS, and plasma are shown in Figure 5.1F. A significant increase (**$p < 0.005$) between the absolute value of the zeta potential for the citrate-GNPs and HA-GNPs in water is notable, whereby the charge on the citrate-GNPs is ~50% less negative. The zeta potential changes radically when both particle types are immersed in

slightly basic media. However, while the HA-GNP surface charge remains negative in both PBS and plasma (showing less of a change in charge of the particles), the citrate-GNP surface becomes slightly positive, corroborating the spectroscopic findings of particle instability in these media. According to our hypothesis, the molecules and proteins which populate these biologically relevant media, in the case of citrate-GNPs, displace and disrupt the citrate-shell, which charge stabilizes the particles and prevents them from aggregating. We also measured the sizes and surface charges of the particles as a function of time (after 6 h and 24 h of incubation in PBS or plasma) finding no differences compared to the measurements reported in Figure 5.1F and Figure 5.1G.

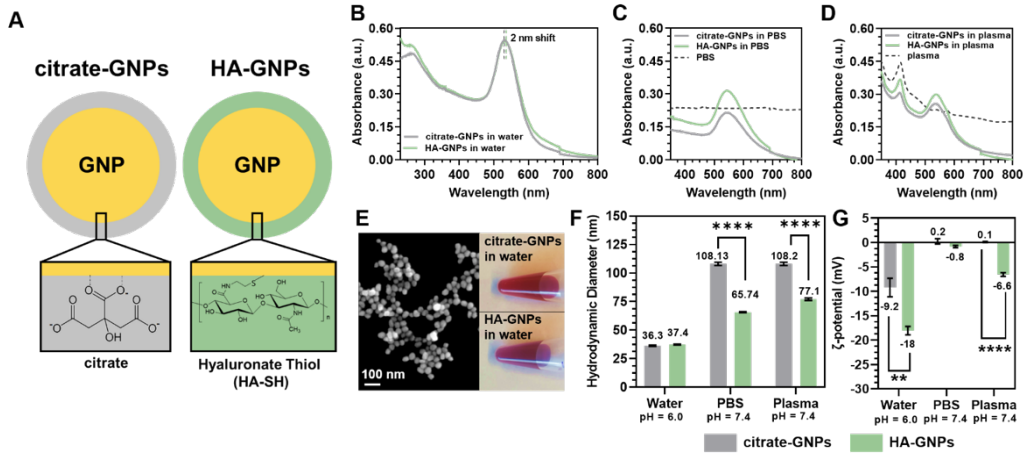

Figure 5.1 (A) Schematic diagram of GNPs stabilized with citrate or surface passivated with thiol-modified hyaluronic acid (where the number of monomers n is ~ 3). Absorbance spectra of citrate-GNPs (gray line) and HA-GNPs (green line) dispersed in (B) water, (C) PBS, and (D) plasma. (E) SEM image of the particles after synthesis (130000x) and optical photographs of citrate-GNPs and HA-GNPs. Measurements of (F) hydrodynamic diameter and (G) ζ-potential of citrate-GNPs and HA-GNPs dispersed in Milli-Q water, PBS, and porcine plasma. Significance is calculated using a multiple unpaired t test (**$p < 0.005$, ****$p < 0.0001$).

5.3.2 In Vitro Cytotoxicity Assessments

In vitro analyses involving HeLa cells were performed to assess any cytotoxic effects due to the GNP treatments. After 24 h of GNP incubation, cell viability, measured by Trypan blue assay, showed that a high dose concentration of HA-GNPs (50 μg [Au]/mL per well) significantly reduced cell viability by almost 40% (***$p < 0.0005$) when compared to no treatment or treatment with citrate-GNPs, as

shown in Figure 5.2A. However, it must be considered that despite the fact that dye exclusion assays, such as Trypan blue, offer an easy and rapid technique to selectively stain cells, viability is determined solely based on cell membrane integrity, without considering any information regarding capacity to grow or cell functionality. In fact, it has been proven that even though the cell membrane integrity has been compromised, there is a possibility for the cell to self-repair and become fully viable, affecting the results [249]. Another potential problem with this assay is related to the dye uptake and limits of signal detection which assess viability in a binary way: if a cell is partially disrupted with only a small amount of dye uptaken and the signal is below the limit of detection, the cell will be classified as viable. Therefore, the use of another complementary assay for viability is also recommended to assess cytotoxicity due to treatment. After 24 h of GNP incubation, cell viability measured by MTT assay showed that a moderate concentration (15 μg [Au]/mL per well) of citrate-GNPs and HA-GNPs were not cytotoxic for the cells. However, high dose concentration (50 μg [Au]/mL per well) reduced cell viability by 22% in case of HA-GNPs (***$p < 0.001$) and almost 28% in the case of citrate-GNPs (****$p < 0.0001$), as shown in Figure 5.2B. This data indicates that treatment dose may be a more important factor on the effects of cell viability over particle surface chemistry. Elemental analysis performed with ICP-OES is reported in Figure 5.2C. The amount of gold is normalized per cell. The amount of gold content quantified after citrate-GNP treatment was significantly higher than that of HA-GNP treatment in HeLa cells: treatment with citrate-GNPs yielded ~20% more gold content than treatment with HA-GNPs after a 24 h incubation period (**$p < 0.005$). This result suggests that the presence of the HA coating shields the particles from the formation of a protein corona which can occur on nascent particles dispersed in a biological media, mediating their interaction and uptake with cells. These results are similar to that reported by Karakocak et al. [250] where nascent GNPs <40 nm administered to retinal pigment epithelial cells (ARPE-19) showed greater cellular internalization than HA coated GNPs as evaluated with ICP-MS.

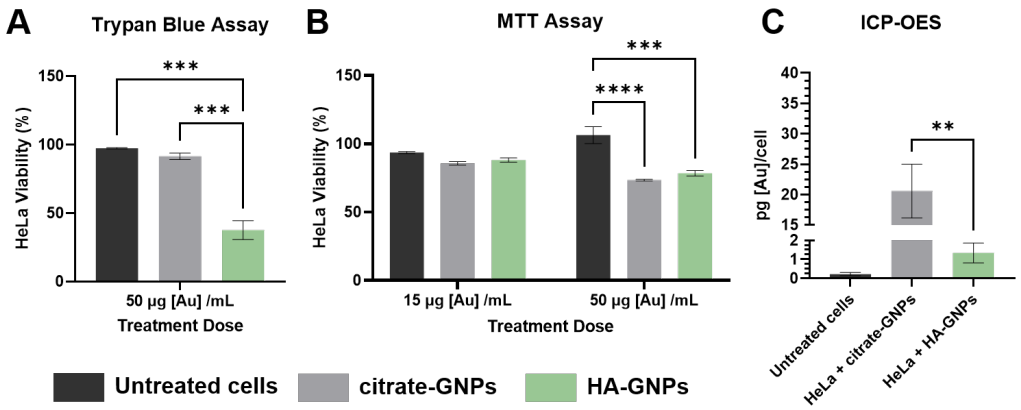

Figure 5.2 In vitro uptake of GNPs in HeLa cells after a 24h incubation. Cytotoxicity assays (where cell viability is expressed as % of living cells divided by the total cells counted) using (A) Trypan blue staining (50 µg/mL per well) and (B) MTT (15 µg/mL per well and 50 µg/mL per well) after treatment with citrate-GNPs and HA-GNPs. (C) Elemental Analysis performed with ICP-OES on HeLa cell pellets 24 h after treatment with citrate-GNPs and HA-GNPs. A two-way ANOVA test was performed to compare the interactions between each group (**p < 0.005, ***p < 0.001, ****p < 0.0001, Tukey's multiple comparisons test).

5.3.3 In Vivo Biodistribution in a Murine Lung Cancer Model

Figure 5.3A presents a schematic of the approach used in this study to investigate differences in GNP accumulation across different regions of the tumor depending on particle surface chemistry. We choose to subdivide the tumors into four different groups which include differentiating between the medial and lateral side of the tumor because we are not only consistently applying an external force to inject the particles toward the medial side but also because of differences in interstitial fluid pressure (IFP) across the tumor. In fact, Stapleton et al. previously demonstrated that the heterogeneity of the IFP across the whole tumor volume affects the intra-tumoral distribution of CT-liposomes in metastatic breast adenocarcinoma-bearing mice [251], [252]. Moreover, spatial measurements of permeability, perfusion, interstitial volume fraction, and plasma volume fraction, revealed heterogeneous changes between the medial and lateral side of the tumor, although this quantification was not thoroughly investigated. Three and six days after intratumoral treatment with either citrate or HA passivated GNPs, mice harboring lung cancer tumors were sacrificed and their tumors resected. Flash frozen tumors were then divided into medial and lateral halves (in reference to the mouse body positioning) and each half was subsequently subdivided into peritumor

and core using a surgical blade. Figure 5.3B shows example photos taken from the lateral side of the harvested ex vivo tumors. Differences in the distribution of the particles between the two GNP treatment types are macroscopically evident (particles are observed as dark spots in the tumor). The HA-GNPs distribute site-specifically along the lateral side of the tumor, while the citrate-GNPs present a low diffusion pattern, remaining close to the injection site (in the core of the tumor) for all 6 days. These observations were also confirmed by elemental analysis performed using ICP-OES on resected tumors. As shown in Figure 5.3C, 3 days post-GNP injection, almost 50% of the HA-GNPs injected remained present in the tumor, with preferential accumulation in the lateral periphery (LP). Gold quantified in this site-specific area was significantly higher (**$p < 0.005$) in the HA-GNP treated mice when compared with citrate-GNP administration. When compared with the data obtained 3 days post GNP injection, the 6-day data shows an ~10% decrease in accumulation in the LP region for both particle types, while particle accumulation in the medial periphery (MP) region increases (Figure 5.3D). This data suggests that over time and as the tumor grows, both particle types diffuse more across the tumor but are still retained intratumorally. Evaluation of the particle biodistribution using ICP-OES in other organs (liver, spleen, lung, heart, blood, kidneys, and brain) for the two different particle surface passivations are reported in Figure 5.3E-F. ANOVA test reveals that the gold content in the citrate-GNP group is significantly higher than that in the HA-GNP group in the livers examined for the data obtained 3 days post injection, and 6 days post injection (**$p < 0.005$, ***$p < 0.001$). Notably, for the 6-day timepoint, citrate-GNP accumulation in the liver was six times greater than that of the HA-GNP. These results suggest that clearance of the citrate-GNPs from the tumor to other organs is higher for both follow up timepoints, and that HA-GNPs are better retained in the TME, possibly due to receptor-mediated inter-actions or interactions with the extracellular matrix. Further, in comparing the 6 day post-injection data with the 3 day post-injection data, the majority of the organs showed an increase in citrate-GNP content and a decrease in the HA-GNP, indicative of their retention in the TME.

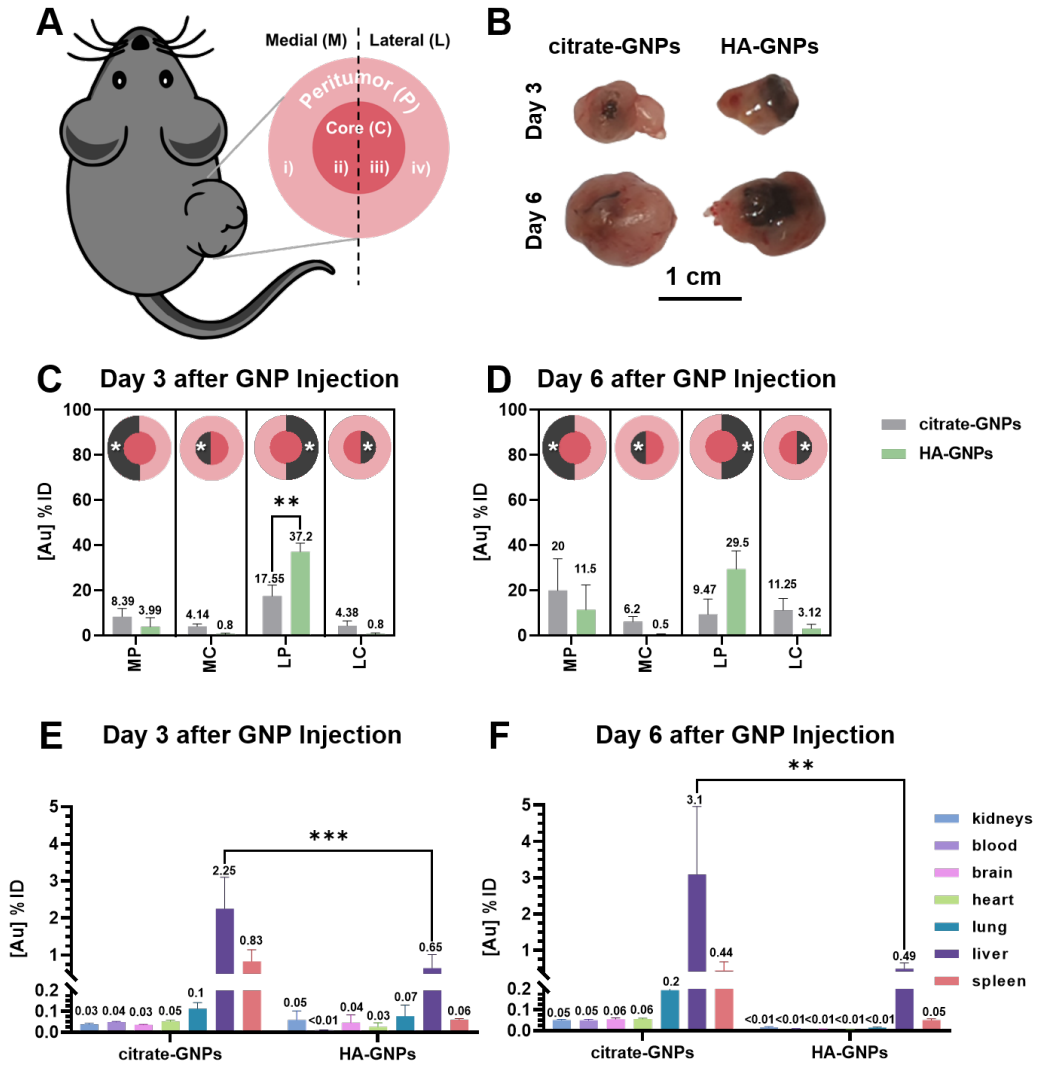

Figure 5.3 In vivo assessments and quantification of GNP distribution in a murine NSCLC model. (A) Schematic of tumor growth and atlas reference for the ex vivo analysis. Tumors were divided in medial and lateral halves (in reference to the mouse body positioning) and each half was subdivided into peritumor and core using a surgical blade. (B) Photos of ex vivo LLC tumors taken 3 and 6 days after intratumoral injection of citrate-GNPs and HA-GNPs. Tumors were photo-graphed exposing only the lateral side, which allows for better appreciation of the GNP distribution with gross inspection (black areas represent particle clusters). Under the same experimental conditions, HA-GNPs distribute site-specifically in the lateral side of the tumor, while citrate-GNPs remain close to the injection site (in the center of the tumor). Elemental analysis per-formed using ICP-OES on resected tumors (n = 4/group) allow for site-specific comparisons between the citrate-GNPs and HA-GNPs (C) 3 days or (D) 6 days post GNP injection. Biodistribution of GNPs in organs calculated using ICP-OES, where gold concentration in each organ is quantified as percentage of injected dose of GNP (% ID) (E) 3 days or (F) 6 days post GNP injection.

A two-way ANOVA test was performed to compare the interactions between each group (**$p < 0.005$, ***$p < 0.001$, Tukey's multiple comparisons test).

5.4 Discussion

We fabricated and characterized citrate-GNPs, surface passivated with hyaluronate-thiol, and assessed their in vitro cytotoxicity as well as cellular uptake in HeLa cells. We tested the colloidal stability of the particles as well as their antifouling properties using PBS and plasma to mimic biological media. We noticed that the increase in hydrodynamic diameter for the HA-GNPs in both media is significantly less than that of the nascent particles, proving that the HA coating is shielding the particles and providing anti-biofouling properties. These findings, along with optical spectroscopy and evaluations of surface charge, also suggest that the presence of HA on the surface of GNPs helps to maintain stability of the particles in biological media.

Metal nanoparticle surface modifications with HA have been used in previous studies as biosensors to measure enzymatic activity of hyaluronidase [253], [254] and to evaluate their ability to target cancer cells via HA receptors as well as their efficiency in releasing drug cargo at a target site [255]. For instance, Kumar et al. loaded metformin (an antihyperglycemic agent commonly used for the treatment of diabetes also known to reduce the risk of developing hepatocellular carcinoma) on HA capped GNPs, and the authors demonstrated that administration of this formulation exhibited increased cytotoxic activity over free drug in liver cancer cells in vitro without hindering zebrafish embryo development in vivo [256]. However, the authors did not report any information regarding biodistribution of the particles in vivo, an important parameter for the clinical translation of this nanoplatform. While a recent study by Xu et al. [257] did investigate pharmacokinetics and particle biodistribution, this was performed for hyaluronic acid-gold nanorods (HA-GNRs) administered intravenously into nude mice with xenograft MCF-7 breast cancer tumors. The authors showed that 24 h after administration, the majority of particles distributed to the liver (~50%) while <15% were present in the tumors. Such a low percent of the administrated dose reaching the tumor target not only reduces the possibility of particle retention in the tumor over time but also decreases the efficiency of light-based therapy. Our study overcomes these limitations by administering the particles locally into the tumor, where we can monitor their retention over time and quantify site-specific accumulation across different regions of the tumor. Further, in our biodistribution

study, we show that post-intratumoral injection, there is <1% particle accumulation in the off-target organs assessed and this percentage does not increase over time.

Although beyond the scope of this work, there are some other interesting aspects of HA that should be discussed for future study. In the human body, HA is typically present at a very high molecular weight (20 MDa) providing elasticity to the tissues [258]. Kuehl et al. [259] tested different molecular weights of iodine-125 labeled HA molecules in the lungs of mice, quantifying organ radioactivity over time after intratracheal instillation. The study demonstrated that molecular weights of HA between 7-67 kDa present rapid systemic distribution, while HA with molecular weights between 67-215 kDa persist longer in the lungs, and HA with molecular weights >215 kDa penetrate poorly to the lungs. Therefore, it may be possible that different molecular weights of HA have an effect on GNP distribution when HA is used as a surface coating. In our study, we used HA with a molecular weight of 10 kDa, but further investigations are necessary to clarify the role of molecular weight of HA and how it can influence diffusion of the metal nanocomplexes in cancerous tissues.

Another point of discussion is how the presence of HA influences particle uptake by cells as well as particle distribution in tissue in relation to expression of its cell surface receptors, such as CD44, hyaluronan-mediated motility receptor (HMMR), and intercellular adhesion molecule-1 (ICAM-1) [260]. Shen et al. [261] demonstrated that hyaluronic acid functionalized lipid nanoparticles loaded with paclitaxel showed more efficient uptake over lipid nanoparticles without HA in B16F10 melanoma cells, facilitating delivery of the drug into these CD44-overexpressing cancer cells. Chiesa et al. [262] observed that the uptake of hyaluronic acid-chitosan nanoparticles by human mesenchymal stem cells occurs through confinement in cytoplasmic vesicle-like regions ~1–3 μm in diameter, located near the CD44+ membrane surface, also suggesting an endocytosis mechanism for cellular uptake of these particles. However, these previous studies were conducted with non-metallic nanocomplexes. In our investigation, we evaluate the in vitro cytotoxicity as well as cellular uptake in HeLa cells, which are known to express CD44 [263], but further research is required to clarify the mechanisms of interaction between hyaluronic acid passivated gold nanoparticles and HA cell surface receptors.

5.5 Conclusions

In conclusion, in this study we fabricated GNPs and passivated their surface with hyaluronate-thiol using an easy and reproducible method. We investigated their physical characteristics and biofouling properties in biological media and examined any cytotoxic effects in vitro using HeLa cells. Finally, we quantified the site-specific distribution of nascent and HA-GNPs after intratumoral administration in a murine model of lung cancer. Our results support the hypothesis that HA enhances GNP distribution in the peritumoral region. This finding improves our knowledge regarding how changes in the surface chemistry of nanocomplexes can result in different localization of the agent across solid tumors, opening new possibilities for applications of nanomedicine in cancer theranostics.

Chapter 6

Improvements in Gold Nanorod Biocompatibility with Sodium Dodecyl Sulfate Stabilization

6.1 Introduction

As a result of their geometry-dependent, unique surface plasmon properties, gold nanorods (GNRs) have revealed great potential in applications involving imaging, therapy, and biological sensing [232]–[235], [236]. In fact, among several types of plasmonic metal nanoparticles, including spherical, pyramidal [269]–[271], symmetry breaking [272]–[275], or other types of core-shell shaped-nanoparticles, such as nanoshells, [95], [276], [277] GNRs have a higher light absorption coefficient in the near-infrared (NIR) region of the electromagnetic spectrum (600-900 nm) [278]–[280]. This characteristic permits a broad range of innovative applications where GNRs can be employed as a multifunctional NIR light-mediated platform. For instance, when the longitudinal localized surface plasmon resonance of GNRs is tuned to NIR, they are able to photothermally induce local cancer cell death after optical excitation [281], [282]. At the same time, GNRs act as excellent contrast agents for photoacoustic imaging with long-lasting photothermal stability [283], [284] during nanosecond-pulsed NIR laser illumination. This NIR-absorption property has also been investigated for single-particle level detection showing that GNRs can be used as small probes for early cancer diagnosis [285], [286].

In addition to their NIR-absorption distinctive properties, researchers have examined GNRs as contrast agents for computed tomography (CT), [287], [288] since they exhibit a higher X-ray attenuation coefficient when compared with iodinated contrast agents [289]. To date, iodine is the most commonly used CT contrast agent to enhance contrast resolution in the body tissues, but it results in short blood circulation time and rapid clearance from the kidneys [290]. Several studies demonstrated that gold nanoparticles have prolonged circulation times dependent on their surface chemistry, such that the particles can achieve a CT outcome with good efficiency with retention times in the body longer than other standard contrast agents [122], [291], [292]. Additionally, gold nanoparticles of different sizes are able to enhance the effects of radiation.[200] All of these characteristics along with the fact that the biological transparency window (~600–1000 nm) coincides with the longitudinal plasmon band of GNRs,[293] make gold nanorods suitable agents to aid in the clinical diagnosis and treatment of cancer with high accuracy and sensitivity, such as through CT-guided photothermal therapy [294], [295], photodynamic therapy [296], and cancer radiotherapy [297].

One of the main challenges that limits the clinical translation of GNRs is their controversial safety profile. There is a lack of knowledge concerning the undesired consequences of GNRs or the byproducts associated with their synthesis when they come into contact with a living organism [298]. For instance, the nature of their toxicity is still under debate. The most common approach to synthesize GNRs is to use cetyltrimethylammonium bromide (CTAB) as a growth-directing surfactant, which assembles as a bilayer structure on the GNR surface. CTAB is essential for nanorod growth because it stabilizes the particle size and permits growth into an anisotropic shape, which allows for a tunable surface plasmon mode as a function of aspect ratio. CTAB, however, is a moderately cytotoxic agent [299] which interacts with the phospholipid bilayer of the cellular membrane to inhibit the enzyme ATP-synthase by the centrimonium cation, leading to cell death [300]. Therefore, CTAB exchange, removal, or overcoating on the GNR surface is required prior to any biological application [301]. Some studies indicate that GNR cytotoxicity may be caused by impurity of surfactant, suggesting that cytotoxicity is caused by free CTAB in solution [302] and the quantity of surfactant [303]. However, other researchers have proven that GNR cytotoxicity is mainly related to the CTAB bilayer on particle surface rather than the free residual molecules in solution [304].

Since the removal of CTAB causes instability of GNR suspensions, a major challenge is to prevent GNR aggregation while maintaining a low toxicity profile [305]. To solve this issue, several researchers exchanged the CTAB layers with more biocompatible ligands, such as thiolated polyethylene glycol (PEG) [306], 1,2-dimyristoyl-sn-glycero-3-phosphocholine (DMPC) phospholipid molecules, [307] mercaptoundecanoic acid (MUA) [308], or thiolated polyamidoamine (PAMAM) [309]. Others have used multistep exchange processes, whereby CTAB was first exchanged with polystyrenesulfonate, which was then displaced with citrate [299]. An alternative strategy is to completely encapsulate the GNR surface with an additional biocompatible coating, for example bovine serum albumin (BSA) [310] or human serum albumin (HSA).

In this study, we aim to investigate the effects of the charge of the GNR surfactant on cell viability. We used sodium dodecyl sulfate (SDS) as an overcoating agent which stabilizes the GNR surface, changing the net charge from positive (CTAB) to negative. Since cationic-anionic surfactant mixtures, known as “catanionics”, such as those composed of SDS/CTAB, exhibit properties different from those of the individual surfactants, they can demonstrate improvements in stability and also be used to mimic biological membranes [311]. SDS has been used

in a recent study as anionic surfactant to replace the CTAB bilayer during the synthesis of small GNRs (28 x 7 nm), showing improved cell viability in A549 adenocarcinomic human alveolar basal epithelial cells [312]. We optimized the purification process of large GNRs (120 x 40 nm) and investigate the mechanisms of their cellular uptake as well as their cytotoxic effects in a murine model of Lewis lung carcinoma (LLC) and a human model of cervix adenocarcinoma (HeLa).

The selection of GNR dimensions for achieving efficient contrast for bioimaging, as well as for photothermal therapeutic applications, is based on the optical properties of the nanoparticles. In fact, the choice of larger nanorods derives from previous observations which report that, generally, GNRs with aspect ratio ~3 and width < 40 nm produced a stronger photoacoustic signal compared with smaller nanorods (width < 25 nm) [266]. In addition, it has been proven that GNRs with a larger effective radius and high aspect ratio produce the highest scattering contrast for imaging applications [313] as well as greater effect on X-ray attenuation [289]. This size regime allows for powerful ablation and strong imaging contrast, characteristics suitable for theranostic applications.

The outcomes presented here benefit in our understanding of the mechanisms of the biological action of surfactants and their mixtures used as nanoparticle stabilizers, and consequently, aid in the design of innovative GNR-based platforms for cancer nanotheranostics.

6.2 Materials and Methods

6.2.1 Synthesis of Gold Nanorods (GNRs)

Gold nanorods were synthesized by a binary surfactant method modified to produce sufficient quantities of gold nanorods that are approximately 40 nm in transversal dimension and 120 nm in longitudinal length [314]–[316]. In this method, gold(III) chloride is reduced to gold(I) ions in the presence of cetyltrimethylammonium bromide (CTAB) and sodium oleate (NaOL). Gold nanorod growth is then initiated by injecting separately synthesized gold nanoparticle seed solutions. The nanorod synthesis can be monitored by tracking the plasmon peak in the extinction spectrum in real time. When the peak is at the desired wavelength, the growth solution is pelleted in a centrifuge, the growth solution is removed, and the nanorods are resuspended in CTAB solution. If the synthesis is not stopped, the nanorods will grow to become large and polydisperse.

The growth solution was prepared in a round bottom flask with 50 mL of deionized water heated to 50 °C on a temperature-controlled heating mantle. 1.5 g of CTAB (Sigma Aldrich, St. Louis, MO, USA, H9151 lot 019K00241) and 0.247 g of NaOL (Sigma Aldrich, St. Louis, MO, USA, O7501 lot SLBR5187V) were added, the solution was stirred until the powder dissolved, and then allowed to cool to 30 °C. A 4 mM silver nitrate solution was prepared by adding 68 mg $AgNO_3$ (Sigma Aldrich, St. Louis, MO, USA, 209139 lot MKCK0755) to 100 mL of water at room temperature. A 20 mM gold chloride stock solution was prepared by adding 788 mg of $HAuCl_4$ (Sigma Aldrich, St. Louis, MO, USA, 520918) to 100 mL of deionized water. 2.5 mL of this stock solution was diluted into 47.5 mL of deionized water held at 30 °C in a temperature-controlled bath. Once the surfactant mixture is stable at 30 °C, 4.8 mL of the $AgNO_3$ solution is added, and the surfactant mixture is left undisturbed at 30 °C for 15 minutes. Next, the 50 mL $HAuCl_4$ solution is added to the surfactant mixture and set for medium stir at 30 °C for 90 minutes. The solution is initially a yellowish orange color and over time becomes clear. During the 90 minute incubation, 64 mM ascorbic acid (Sigma Aldrich, St. Louis, MO, USA, 95209 lot 1442630V) solution is prepared by adding 565 mg of powder to 50 mL of deionized water and letting it dissolve in the 30 °C bath. To create the seed particles, 0.125 mL of the 20 mM gold chloride stock solution is added to 4.875 mL of deionized water. This 5 mL solution is combined with 5 mL of a 200 mM stock solution of CTAB, which must be heated to completely dissolve the surfactant. Next, 10 mM $NaBH_4$ (Sigma Aldrich, St. Louis, MO, USA, 480886 lot MKCJ8009) was prepared by adding 38 mg of powder to 100 mL of deionized water. The solution was gently swirled and immediately used (between 1 and 2 minutes from the time it was dissolved as $NaBH_4$ is not a stable solution and creates hydride ions that reduce the gold ions to create the seed particles). Note that the hydride ion concentration varies over time and is sensitive to temperature and stirring conditions. The seed solution was stirred vigorously and ~1 mL of the $NaBH_4$ solution was added. Stirring of the seed solution was stopped, and the solution left to sit for 30 minutes. Since the hydride concentration is sensitive to preparation conditions, multiple seed solutions were made by adding varying amounts of $NaBH_4$ solution (e.g. 0.3 mL, 0.6 mL, 0.9 mL, and 1.2 mL) and the seed solution that appeared faint brown after 30 minutes was used. Once the surfactant growth solution had incubated for 90 minutes, 2.5 mL of a 3 M HCl (Sigma 320331 lot MKCJ5989) stock solution was added and the growth solution set to slowly stir for 15 minutes while the temperature was held to 30 °C. After this time, 0.25 mL of the ascorbic acid solution was added, and the growth solution vigorously stirred for 30 seconds. Next, 0.002 mL of the seed solution was added, the growth solution stirred

for 30 seconds, and then left still at 30 °C. The nanorod synthesis continued to proceed over several hours.

Small volumes of the growing nanorods were periodically sampled and their extinction spectra measured to monitor the plasmon resonance. A weak plasmon band is initially observed at the limit of the instrument's spectral window (~1000 nm) and it grows and shifts to shorter wavelengths. Once it reaches ~800 nm, the growth solution is transferred to glass tubes and pelleted in a centrifuge at 2000 RCF for 20 minutes. The growth solution was decanted and the nanorods pellets and resuspended in CTAB or SDS (Sigma Aldrich, St. Louis, MO, USA, 436143 lot MKBF9866V) solution at the desired concentration (2 to 10 mM). This purification process is also used to transfer nanorods initially stabilized in CTAB to SDS solution.

6.2.2 GNR Characterization

After synthesis gold nanorods optical properties and morphology were evaluated with UV-VIS spectroscopy and high contrast transmission electron microscopy (TEM). Modifications in surface chemistry were evaluated with ζ-potential and surface-enhanced Raman scattering (SERS). Physicochemical properties of the gold nanorods were also investigated with high resolution computed tomography (micro-CT) to classify the gold nanorods as potential diagnostic agents.

6.2.3 ζ-potential

Particle surface charge (ζ-potential) was measured with a Zetasizer Nano ZS (Malvern Panalytical, MA, USA). Briefly, 1 mL of the sample solution (concentration < 1 mg/mL) was placed in a four-sided cuvette capped by the universal dip cell ZEN1002. All the measurements were conducted at 25 °C with a refractive index of 1.

6.2.4 Ultraviolet-Visible (UV-VIS) Spectroscopy

For synthesis and surface chemistry modifications of gold nanorods, absorbance spectra were recorded with an Ocean Optics USB4000 fiber spectrometer in glass cuvettes. For applications in cell culture, absorbance spectra of the prepared GNR solutions were obtained on a Beckman-Coulter UV-VIS (200–1000 nm) spectrophotometer (DU 730, Beckman Coulter, Inc., Brea, CA, USA). The sample in 1 mL volume (concentration < 1 mg/mL) was stored in a four-sided cuvette and placed in the standard single cell holder of the machine. To obtain optimal results, before taking each sample measurement a blank measurement (with milli-Q water) was performed. We measured the spectra after syn-thesis and after dispersion in serum obtained from healthy porcine (Male Castrated Yucatan Minipig, ~38 kg, S&S Farms, Ramona, CA, USA) approved by the Institutional Animal Care and Use Committee (IACUC) at the Houston Methodist Research Institute (approved code: AUP-0620-0035, 2 June 2020). To obtain the serum, whole blood was collected in serum blood collection tubes (BD Vacutainer, Franklin Lakes, NJ, USA) and centrifuged for 15 min at 2000xg.

6.2.5 Transmission Electron Microscopy (TEM)

Gold nanorod solutions are deposited on 300 mesh copper grids with a lacey carbon film (Ted Pella 01890). A 5 μL drop of the solution is applied to the grid which is held in the air with tweezers until the solution dries. The grid is imaged in a JEOL 2100F transmission electron microscope with a CCD camera. The images are captured and processed by Digital Micrograph software from Gatan Inc.

6.2.6 micro-computed tomography (micro-CT)

To investigate the physicochemical properties of the gold nanorods as a promising multifunctional platform for theranostics, we imaged both CTAB-GNRs and SDS-GNRs using a Siemens Inveon High-Resolution Micro Computed Tomography (slice thickness of 105 μm, in a plane resolution of 105 μm, tube voltage at 80 kV, tube current at 500 μA, and exposure time of 240 ms). Sample dilutions were prepared in 0.2 mL individual tubes with flat cap (Thermo Fisher Scientific, Waltham, MA, USA, AB0620) in 30 μL volume, ranging from 0 to 2 mg

[Au]/mL after pelleting the particles via centrifugation (1000 xg, 5 min). Gold concentration was established by inductively coupled plasma optical emission spectrometry (ICP-OES). Digital CT images (DICOM files) were analyzed and processed using 3DSlicer and X-ray attenuation intensity was calculated in a Hounsfield unit (HU).

6.2.7 Surface-enhanced Raman scattering (SERS)

Raman and SERS spectra were recorded on a custom-built Raman microspectrometer that uses a stabilized 785 nm, 80 mW diode laser (Coherent Inc., Santa Clara, CA, USA), near-infrared corrected objective lenses, an aberration free IsoPlane SCT 320 spectrometer (Princeton Instruments Inc., Trenton, NJ, USA), and a Pixis 265E open electrode CCD camera (Princeton Instruments Inc., Trenton, NJ, USA) [317]. The sample is continuously pumped through glass capillaries to avoid any settling of the nanoparticles or heating by the laser.

6.2.8 Cell Lines and Passaging

In this present study, two cell types were treated and observed: cervix adenocarcinoma (HeLa) and murine Lewis lung carcinoma (LLC) cells. Both cell lines were purchased from ATCC® (American Type Culture Collection, Manassas, VA, USA).

Protocols for cell culture, maintenance, and sub-culturing were the same for both cell lines. Cells stored in liquid nitrogen were thawed and mixed with 10 mL of complete growth media in T-75 flask. Cell culture flasks and plates were kept in a HERAcell 150i CO2 incubator (Thermo Fisher Scientific, Waltham, MA, USA) set to 37 °C and 5% humidity, and media was changed every few days as needed to maintain cell growth. Dulbecco's modified Eagle medium (DMEM) was the basal media used to subculture LLC cells, while Eagle's Minimum Essential Medium (EMEM) was the basal media used to subculture the HeLa cells. Complete growth media of DMEM and EMEM were prepared by adding 10% fetal bovine serum (FBS, USDA approved, ATCC®, Manassas, VA, USA). Cells were passaged for subculturing using 0.25% trypsin-0.53 mM EDTA solution (Thermo Fisher Scientific, Waltham, MA, USA, 25-200-056) and then neutralized with complete

growth media. The cell suspension was then centrifuged at 130 xg for 5 min. Afterwards, the supernatant was removed, the pellet was resuspended in 1 mL of complete media, and the cells counted using a Countess™ II FL Automated Cell Counter (Invitrogen, Carlsbad, CA, USA) and plated into 6-well/96-well plates and grown until confluent (as described further in section 6.2.12).

6.2.9 Viability Assays

Viability assays were performed to compare the effects of CTAB-GNR and SDS-GNR treatments in both cancer cell lines and detect potential cytotoxicity dependent on the treatment dosage, incubation time, and surfactant type.

6.2.10 Trypan Blue Assay

Trypan blue is a diazo dye which is taken up exclusively by dead cells, while un-stained cells represent the total number of viable cells. In this assay, both cell lines were treated with CTAB-stabilized or SDS-stabilized gold nanorods, incubated for a 24-hour period, trypsinized, and stained with trypan blue. We quantified the number of viable (unstained) cells and assessed cell proliferation or cytotoxicity due treatment in comparison to untreated (control) cells.

Each cell line was seeded into 6-well plates at a concentration density of $1x10^5$ cells/mL. We treated the cells in triplicate wells by replacing the culture medium with fresh medium containing 15 μg [Au]/mL of particles and incubating the cells for 1h, 3h, 6h, 12h, and 24h at 37 °C and 5% humidity. Cells were detached from the wells using 0.25% trypsin–0.53 mM EDTA solution and resuspended with 1 mL of complete growth media. 1% of cells were aliquoted, stained with 0.4% Trypan Blue Solution (Thermo Fisher Scientific, Waltham, MA, USA, 15250061), and counted using a Countess™ II FL Automated Cell Counter (Invitrogen, Carlsbad, CA, USA). The remaining cell solution was centrifuged at 100xg for 5 min to remove the supernatant. This pellet was used for ICP-OES analysis as described in section 6.2.14.

6.2.11 MTT Assay

To evaluate treatment-related modifications in the rate of cell proliferation, we spectrophotometrically assessed reduction of 3-(4, 5-dimethylthiazolyl-2)-2, 5-diphenyltetrazolium bromide (a yellow dye known as MTT) to the blue product formazan. To perform this assay, both cell lines were first seeded separately into 96-well plates (Corning™ Costar™ 96-Well, Cell Culture-Treated, Flat-Bottom Microplate, Thermo Fisher Scientific, Waltham, MA, USA, 15250061) at a concentration density of $1x10^5$ cells/mL and incubated in a cell culture incubator for 24hrs. The following day, the media was aspirated and replaced with fresh medium containing the particles to expose the cells to the colloidally stable, homogenous dispersions of gold nanorods. Different concentrations of gold nanorod treatment were investigated: low-dose treatment at 1µg [Au]/mL, medium-dose treatment at 15µg [Au]/mL, and high-dose treatment at 50µg [Au]/mL. After an additional 24 h incubation period at 37 °C and 5% humidity, 10 µL of MTT Reagent (ATCC®, American Type Culture Collection, Manassas, VA, USA) was added to each well, and the plates incubated until a purple precipitate was visible under the microscope. All wells were then treated with 100 µL of Detergent Reagent (ATCC®, American Type Culture Collection, Manassas, VA, USA) until complete dissolution to formazan, which occurs when the dark colored solution is homogeneous under micro-scope. A Synergy™ H4 Hybrid Microplate Reader (BioTek Instruments, Inc., Winooski, VT, USA) was used to measure the absorbance of the solution in the well at 570 nm and 690 nm.

6.2.12 Optical Microscopy

Live-cell optical microscopy was conducted to evaluate cell morphology and visually assess cell conditions for all the cell culture experiments reported. Cells that do not display typical morphology is an indicative of possible toxicity due to the administered treatments. Abnormalities in cell morphology include blebbing [318], swollen mitochondria [319], and detachment from the substrate [320]. Optical microscopy images were acquired using a Nikon ECLIPSE Ts2 Inverted Microscope (Nikon Instruments Inc., Melville, NY, USA) with a 10x magnification objective and 50% brightness.

6.2.13 Electron Microscopy

To perform electron microscopy assessments, HeLa and LLC cells treated with CTAB-stabilized or SDS-stabilized gold nanorods were pelleted by centrifuging for 5 min at 100 xg, resuspended in 1 mL of 4% paraformaldehyde (Electron Microscopy Sciences, Hatfield, PA, USA), and left overnight for fixation and preservation. Following this procedure, the samples were washed three times through repeated centrifugation and resuspension with 0.1 M PBS. The PBS is then replaced with 2% osmium tetroxide (OsO_4) in cacodylate buffer (Electron Microscopy Sciences, Hatfield, PA, USA), and allowed to incubate for 2 h at room temperature, before washing three times with 0.1 M PBS. To remove water, the specimens were resuspended in a series of graded ethanol (Pharmco, Brookfield, USA) at 30%, 50%, 70%, and 90% for 10 min each, followed by a wash of 90% acetone (Sigma Aldrich, St. Louis, MO, USA) for 10 min and three washes 100% acetone for 15 min. Samples were embedded in 100% resin using flat molds after 2 h pre-inclusion in resin/100% acetone (1:1), followed by overnight pre-inclusion in resin/100% acetone (2:1), and finally 3 h pre-inclusion in 100% resin (Electron Microscopy Sciences, Hatfield, PA, USA). Polymerization was obtained by incubating the samples for 48 h at 60 °C in a laboratory oven (Quincy Lab Inc., Chicago, USA) and the hard blocks were sliced into 100 nm ultrathin sections using a diamond knife (DiATOME Diamond Knives, Hatfield, PA, USA). Sections were placed on copper grids (200 mesh) (Ted Pella, Inc., Redding, CA, USA), stained with uranyl acetate and lead citrate (Electron Microscopy Sciences, Hatfield, PA, USA). Images were obtained with a FEI Nova NanoSEM 230 (FEI Co., Hillsboro, OR, USA) using the bright field setting in STEM mode under a vacuum of 15 kV.

6.2.14 Inductively coupled plasma optical emission spectrometry (ICP-OES)

Inductively coupled plasma optical emission spectrometry (ICP-OES) measurements were performed with Varian Agilent 720-es ICP spectrometer (Agilent, Santa Clara, CA, USA) to quantify the cellular uptake of the gold nanorods. Gold calibration curves were generated by diluting a gold standard consisting of Au 1000 mg/mL in 10% hydrochloric acid (HCl) (Perkin Elmer, Waltham, MA, USA) in a solution prepared with 1% trace metal grade nitric acid (HNO_3, Thermo Fisher Scientific, Waltham, MA, USA) and 10% trace metal grade HCl (Thermo Fisher Scientific, Waltham, MA, USA). Gold emission was measured

at 242.794 nm and 267.594 nm using the ICP-OES software (ICP Expert II). After a 24h incubation period with the particles, collected cell pellets were digested in 1mL aqua-regia solution (nitric acid and hydrochloric acid in a molar ratio of 1:3) in a chemical fume hood for 1h. We then added 2 mL of standard diluent (10% HCl, 1% HNO_3) and filtered the final solution using 0.6 μm filters (MilliporeSigma™, Burlington, MA, USA, Steriflip Quick Release-GP Sterile Vacuum Filtration System). All measurements were performed in triplicate, averaging the outcomes from the two emission lines. The gold content found in each pellet was normalized to the total number of counted cells (dead and alive). With this normalization, we assume that nanorod internalization does not vary between the cells.

6.2.15 Statistical Analysis

GraphPad Prism (version 9.1.0; GraphPad Software, Inc., San Diego, CA, USA) was used for all statistical analyses and graphs. Mean ± s.e.m. values were calculated for all results. Statistical significance was assessed by one-way or two-ways analysis of variance (ANOVA) with Tukey's multiple comparisons test.

6.3 Results

6.3.1 GNR Surface chemistry modification and characterization

Figure 6.1A shows a schematic of the surface chemistry modification with SDS after synthesis and stabilization with CTAB surfactant. SDS has been chosen as anionic surfactant to overcoat the CTAB bilayer on the GNRs. After synthesis and coating, the GNR longitudinal and transversal dimensions were estimated from the TEM images (where an average of 50 particles were measured) using Matlab (v9.9.0.1467703, R2020b, The MathWorks, Inc., Natick, MA, USA). CTAB and SDS functionalized particle solutions appeared similar in color, indicative that the particles were similar in size, and upon TEM inspection, displayed low polydispersity (Figure 6.1B insets). As reported in Figure 6.1B, particle size was found to be 120 ± 2.5 nm in length and 38 ± 1 nm in width for CTAB-GNRs and 118 ± 2.4 nm in length and 36 ± 1 nm for SDS-GNRs, highlighting that there was no significant difference in shape or size between particle treatment types. Aspect ratios were 3.14 ± 0.43 for the CTAB-GNRs and 3.26 ± 0.35 for SDS-GNRs (mean

± s.e.m.). Zeta potential measurements were performed for all the samples at room temperature and pH equivalent to synthesis conditions. Figure 6.1C shows the difference in surface charge for the particle types, whereby the CTAB-GNRs have a net positive charge of 18.53 ± 5.44 mV, while the SDS-GNRs exhibit a negative charge of -14.7 ± 2.06 mV.

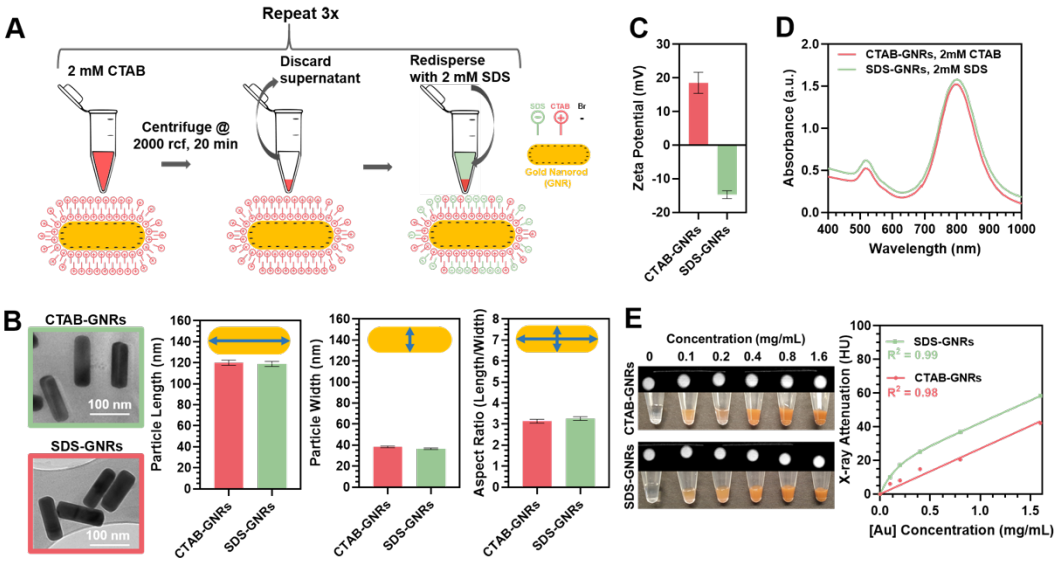

Figure 6.1 Surface chemistry modification and characterization of CTAB-GNRs and SDS-GNRs. (A) Schematic of the surface chemistry modification process of the nanorods with CTAB and SDS surfactants. (B) Transmission electron microscopy (TEM) images of the particles and quantification of particle length, width and aspect ratio. (C) Zeta potential and (D) Absorbance spectra of the nanorods stabilized with CTAB and SDS. (E) X-ray attenuation of the nanorods as a function of gold concentration obtained using a micro-CT source. CT contrast (upper view) and photos (low-er view) for each sample dilution. X-ray attenuation as a function of gold concentration is plotted. Data points are fit using linear regression (CTAB-GNRs) where y= 24.7x + 2.5 or two-phase association (SDS-GNRs) where y= 151.1*(1-exp(-6.9x) + 45658.2 *(1-exp(-6.9x).

Absorbance spectra collected in the range 200–1000 nm display two distinct plasmon resonance peaks for the GNRs arising from their anisotropic configuration (transverse and longitudinal bands), which correspond to the oscillation of electrons in the shorter (517 nm) and longer (CTAB-GNRs: 795 nm, SDS-GNRs: 800 nm) axis (Figure 6.1D). We attribute the redshift in the longitudinal band in the SDS-GNRs to changes in the refractive index of the local environment and interparticle distance which depends on the dispersion status altered by the presence of the anionic surfactant. No evidence of macro-aggregation or flocculation phenomena is visible from the spectra or upon physical inspection of the particles.

X-ray attenuation of GNRs measured using micro-CT are reported in Figure 6.1E. The inset on the left represents optical photos of the gold nanorods dilutions as well as their CT contrast in the coronal plane. All data points were normalized to the attenuation of water (0 mg/mL particle concentration). An increase in attenuation from low to high concentration was observed for both the CTAB-GNRs and SDS-GNRs. Interestingly, the SDS-GNRs attenuate slightly more than CTAB-GNRs at the same concentrations and experimental conditions. However, we also observed that in the case of the SDS-GNRs, when plotted as a function of gold concentration, the CT attenuation values deviate slightly from linearity ($R^2 = 0.96$ when fit with a linear regression versus $R^2 = 0.99$ when fit with two-phase association). Further investigations are necessary to clarify this behavior. Overall, the increase in x-ray attenuation as the gold mass increases indicates that GNRs can act as CT contrast agents and are suitable for theranostic applications.

The ability of gold nanostructures to focus light onto a presence of nearby molecule due to their surface plasmons can be exploited with SERS, a spectroscopic technique that enhances the Raman scattering of adsorbed molecules. Changes in surface chemistry such as the length [321], angle [322], or conformation [323] of a small molecule attached to gold nanoparticle surface, lipid transfer from the surface, [324] as well as the presence and interactions of intercalants or biomolecules [325], [326] can all be structurally identified using SERS. Figure 6.2A displays the SERS spectra of CTAB-GNR and SDS-GNR solutions as well as SERS spectra of SDS-GNRs redispersed in serum. Figure 6.2B contains unenhanced Raman spectra of pure CTAB and SDS solutions for reference. CTAB has an isolated peak at 760 cm^{-1} that corresponds to the symmetric stretching vibration of the trimethylammonium headgroup. SDS has a band of peaks at 800 – 900 cm^{-1} that represents various headgroup and alkane chain modes. These regions of interest are highlighted in Figure 6.2A-B. The SERS spectra from CTAB-GNR solution contains a strong peak at 760 cm^{-1} as expected since the surfactant forms a bilayer on the GNR, with the headgroup positioned near the gold surface and strongly enhanced. SERS from SDS-GNRs has a reduced peak at 760 cm^{-1}, as well as a strong, isolated peak at 870 cm^{-1} that is within the band that corresponds to SDS. The SERS enhancement of a specific peak within the band is not uncommon in SERS since the signal depends on the orientation of the SDS molecule within the near field of the gold nanorod. This data supports the hypothesis that the CTAB is not completely dissociated from the GNR surface and rather that the SDS is acting as an additional coating agent. The SERS spectrum of SDS-GNRs in serum is weaker than SDS-GNRs in their native solution. However, the presence of a peak at 760 cm^{-1} is preliminary evidence that the SDS functionalization allowed the nanorods to incorporate into the serum

and are still stable. Figure 6.2C-D show the absorption spectra of SDS-GNRs and CTAB-GNRs respectively after preparation and after resuspension in porcine serum. Both absorption measurements (Figure 6.2D) and visual inspection (Figure 6.2E) confirm that CTAB-GNRs are not stable in serum, while the SDS-GNRs absorption spectrum shows well-defined peaks after particle redispersion in serum (Figure 6.2C). For the SDS-GNRs sample in serum, no macro-aggregation is visible in solution (Figure 6.2E).

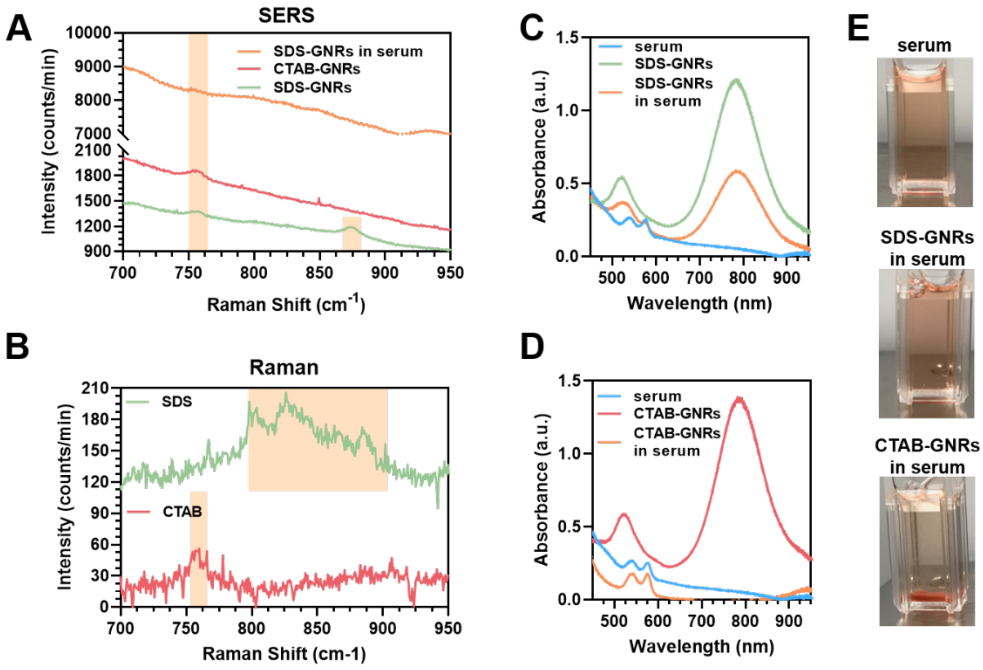

Figure 6.2 (A) SERS spectra of CTAB-GNRs and SDS-GNRs and tentative band assignments. (B) unenhanced Raman spectra of pure CTAB and SDS solutions for reference. Absorption spectra of (C) SDS-GNRs and SDS-GNRs in serum, and (D) CTAB-GNRs and CTAB-GNRs in serum. (E) Optical photos of the functionalized GNRs in serum showing instability of CTAB-GNRs.

6.3.2 Dose-dependent cytotoxicity effects of CTAB-GNRs and SDS-GNRs

In this section we report our results on the viability, proliferation, and morphology of cancer cells after GNR exposure. We studied these effects after incubation of the cells with the particles for 24h, using a low, medium, and high dose treatments. Figure 6.3A and Figure 6.3B show optical microscopy images of

a monolayer of HeLa and LLC cells treated and incubated for 24h at 37 °C and 5% humidity with 15 µg [Au] /mL CTAB-GNRs or SDS-GNRs. After the 24h incubation with CTAB-GNRs, the typical epithelial cell morphology of the HeLa cells, and the rounded, loosely attached morphology of the LLC cells (untreated controls), changed to destroyed or floating for both cell lines. This is not surprising as the cationic surfactant, CTAB, is able diffuse across the cell membrane directly and target the mitochondria causing apoptosis. Conversely, GNRs stabilized with the anionic surfactant, SDS, were able to enter the cells directly by endocytosis without destruction of the cell membrane. Macro-accumulation of the SDS-GNRs in the HeLa cytoplasm is visible with optical microscopy. Macro-traces of the SDS-GNRs are also visible in LLC cytoplasm. In order to provide the most reliable results, we assessed cell viability with two different assays: Trypan blue and MTT. Trypan blue results are reported for the HeLa cells in Figure 6.3C and LLC cells in Figure 6.3D, and MTT results are reported for the HeLa cells in Figure 6.3E and LLC cells in Figure 6.3F. All the treatment doses result in significant cytotoxicity for CTAB-GNRs in both cell lines, while the SDS-GNRs were cytotoxic only at high dosage (50 µg/mL). The differences obtained by comparing the two viability assays in the case of 15 µg [Au] /mL indicates that the in-creased cytotoxicity observed in the MTT assay is mainly influenced by mitochondrial metabolism. Despite the huge difference in cell viability between the CTAB and SDS stabilized GNR treatments, viability decreased in both cases in a concentration-dependent manner.

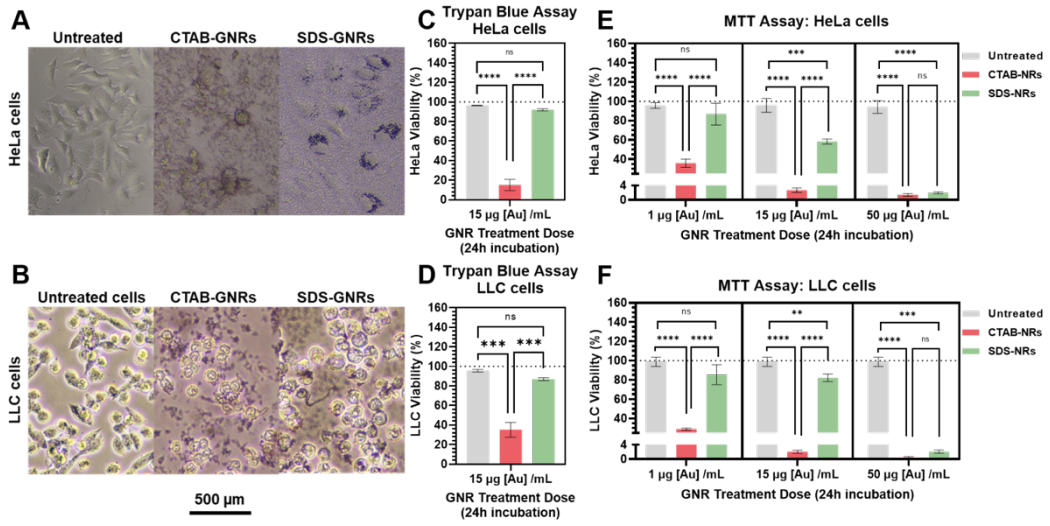

Figure 6.3 Effects of CTAB-GNRs and SDS-GNRs treatment on cell viability. Optical microscopy images of (A) HeLa and (B) LLC cells treated and incubated for 24h with 15

μg [Au] /mL CTAB-GNRs and SDS-GNRs. Trypan blue assay for (A) HeLa and (B) LLC cells treated and incubated for 24h with CTAB-GNRs and SDS-GNRs. Significant difference between groups (***$p < 0.0005$, ****$p < 0.0001$). MTT assay for (A) HeLa and (B) LLC cells treated and incubated for 24h with CTAB-GNRs and SDS-GNRs. Significant difference between groups (*$p < 0.05$, ***$p < 0.0005$, ****$p < 0.0001$) for all treatment doses. SDS-GNRs are significantly cytotoxic at higher doses in both cell lines. All data in the figure are reported as mean ± s.e.m in triplicate.

6.3.3 Time-dependent cytotoxicity effects of CTAB-GNRs and SDS-GNRs

In this section we report time dependent results on the cell viability, proliferation, and morphology, along with the levels of cellular uptake for each GNR treatment type. We noticed under microscopic gross inspection that after administration, the CTAB-GNRs had an immediate cytotoxic effect on both cell lines, while the SDS-GNRs remained unaltered. We hypothesized that cytotoxicity could be a function of time in the case of GNR administration. We tested this hypothesis by measuring cell viability over time using the Trypan blue assay in HeLa (Figure 6.4A) and LLC cells (Figure 6.4B) incubated with the nanorods. The CTAB-GNR treatment killed the cells after just 1 hour of particle incubation, while the cells treated with SDS-GNRs remained viable over time. We then quantified the gold internalized by the cells over time using ICP-OES (Figure 6.4C-D). Interestingly, it seems that the mechanisms of SDS-GNR uptake were cell line dependent: the LLC cells exponentially encapsulate the particles over time, while internalization of the SDS-GNRs in the HeLa cells occurred mostly within the first hour of incubation and increased slightly over time. To assess the toxicology of the GNR particles after 24 h of treatment, we acquired SEM images of the HeLa (Figure 6.4E) and LLC cells (Figure 6.4F) in STEM mode. Another scientific concern regarding internalization of a nanomaterial is related to the possibility of ultrastructural changes of the particles. SEM images revealed that the SDS-GNRs are internalized in vesicles and that their shape is unaltered after cell internalization in both cell lines.

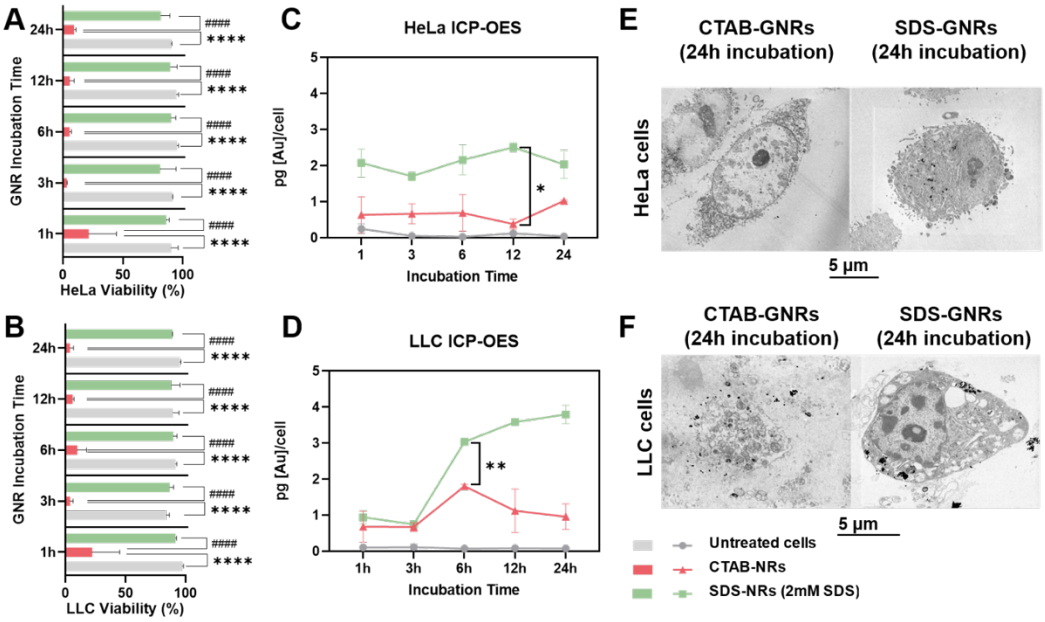

Figure 6.4 Effects of CTAB-GNRs and SDS-GNRs treatment on cell viability as function of incubation time and cell line. (A, B) Viability determined by Trypan blue assay and (C, D) intracellular uptake determined by ICP-OES plotted as function of incubation time for (A, C) HeLa and (B, D) LLC cells. Significant cytotoxicity for CTAB-GNPs (****$p < 0.0001$). All data in the figure are reported as mean ± s.e.m in triplicate. STEM images of fixed (E) HeLa and (F) LLC cells treated and incubated for 24h with CTAB-GNRs and SDS-GNRs.

6.4 Discussion

In this study we demonstrate that the charge of the surface coating agent modulates the cytotoxicity of GNRs in mammalian cells. We confirmed surface modification of the nanorods with SDS using SERS and notably, this improves their stability when applied to a biological environment, such as serum. Further, at the same concentration (2mM), CTAB and SDS surfactants have a radically different impact on cell viability. According to our results, exposure time is an impact factor for cytotoxicity. In fact, after 1 h of CTAB-GNR incubation, only 20% of the cells were viable, indicating that the toxic effects are immediate for particles stabilized with cationic surfactant, even though the longer incubation time (24 h) resulted in greater cell death.

Intracellular gold uptake over time was quantified using ICP-OES and presented differences in the particle uptake kinetics depending on the cell line. Both quantification analysis and optical microscopy confirmed the presence of the particles in the cellular cytoplasm. However, while ICP-OES is an excellent quantitative tool for gold content, it cannot differentiate between GNRs adsorbed on the surface of the cell and those internalized within the cell. As reported in literature [302], treatment of cells with heparin sulfate prior to analysis can be used to desorb surface-adsorbed nanoparticles, since the heparin sulfate polymer has a higher binding affinity to the cellular surface and can displace any surface-bound GNRs. Moreover, for a better understanding of the mechanism of CTAB/SDS-stabilized GNR cytotoxicity, the amount of surfactant that is effectively inside the cell should be measured.

Finally, we measured the X-ray absorption properties of the GNRs using a micro-CT source. The increase in CT attenuation as the gold mass increases indicates that GNRs can be used as CT contrast agents, opening the door to a vast range of theranostic applications.

6.5 Conclusions

In this study, we tested the effects of charge of the surfactant agent used to stabilize GNRs on cell viability. We synthesized GNRs with a positive surface charge through a seed-mediated approach using CTAB as cationic surfactant, and then used SDS, an anionic surfactant, to alter the GNR surface charge to negative values. We evaluated any cytotoxic effects due to GNR treatment type, as well as the mechanisms of cellular uptake in two different mammalian cancer cell lines. Our results suggest a significant dose-dependency effect on cell viability and a time-dependent cytotoxicity effect as a function of surfactant charge for both cell lines. As strategies and technologies to improve local delivery of agents for cancer treatment are emerging, [327]–[330] there is a greater need to better characterize nanoparticles to understand their interactions with cancerous cells. The results of this study can aid in the design of future theranostic applications for oncological translation.

Chapter 7

Near-Infrared Sensitive Nanoparticle Mediated Photothermal Ablation of Ventricular Myocardium

7.1 Introduction

Radiofrequency (RF) catheter ablation is the current standard of care for patients with medically refractory ventricular tachycardia [331]. Despite improvements in catheter technology, higher density mapping, and ablation techniques, outcomes remain plateaued. One shortcoming of RF ablation is the inability to consistently create transmural lesions in regions of scar due to limitations of RF depth, and the inability for RF to penetrate regions of scar and/or fat [332]. Further, RF requires continuous tissue contact, irrigated RF can lead to excessive fluid accumulation in patients with compromised LV function, and extreme tissue temperatures can lead to "steam pops" and cardiac perforation. Near-Infrared Sensitive (NIRS) nanoparticles may have the ability to overcome current RF ablation limitations by creating deeper, transmural lesions in a precise region of interest. Near-infrared (NIR) light can penetrate tissue depths >1 cm which is applicable to ventricular wall thickness. Once exposed to NIR light, NIRS nanoparticles could create cardiac ablation lesions via photothermal heating.

Biocompatible plasmonic gold nanoparticles, known as nanoshells, can be engineered by changing their core and shell dimensions to be sensitive to specific wavelengths [93] in the NIR range, thereby generating heat. Selective light absorption at particular wavelengths is advantageous for applications such as particle optical trapping [333], [334] sensing of nearby small molecules, and conversion of light energy-to-local heat through a phenomenon known as the photothermal effect [338]. Use of gold as the thin metallic shell layer covering the silica core as opposed to other metals is due to the ability to produce strong optical absorption at longer wavelengths (>800 nm) while maintaining resistance to oxidation and biocompatibility [339]. The aim of this study is to assess the feasibility of NIRS gold nanoshells to create ventricular myocardium photothermal ablation lesions.

7.2 Methods

7.2.1 Near-Infrared Nanoparticle Preparation and Characterization

PEGylated (mPEG, 5kDa) silica-gold nanoshells (GNS) (nanoComposix, San Diego, CA, USA, GSGN800) were used as received or concentrated from a 0.05 mg/ml initial stock solution via centrifugation (Eppendorf, Hamburg, Germany) at 1000xg for 30 minutes at room temperature. The supernatant was saved and used to redisperse the particles to generate samples with gold concentrations ranging from 0.05 to 4.00 mg/ml. Sample concentrations were confirmed by inductively coupled plasma optical emission spectrometry (ICP-OES) and measurements performed on a Varian Agilent 720-es ICP spectrometer (Agilent, Santa Clara, CA, USA) using the ICP-OES software (ICP Expert II, v1.1.3.b263, Sydney, Australia, Pty, Ltd 1997-2009). The peak resonance of the nanoshells was ~800 nm. Optical properties of the particles were examined (200-1000 nm) using ultraviolet-visible spectroscopy (UV/Vis) (DU 730, Beckman Coulter, Brea, CA, USA). Nanoshell core and total diameter were 120±9 and 151±8 nm, respectively. Particles were stored at 4 °C and bath sonicated before use.

7.2.2 Nanoparticle temperature measurements in gel formulation

Calcium alginate gels formulated with or without GNS were tested for evidence of photothermal heating under light illumination at different powers (4.0, 5.0, or 5.5 W). Calcium alginate gels were created using equal parts 3% (w/v) calcium chloride (Acros Organics, Geel, Belgium, #349615000) in MilliQ water and 1% (w/v) sodium alginate (50-100 mPa*s) (NovaMatrix, Sandvika, Norway, #4200001) in MilliQ water. To formulate gels containing GNS, GNS were first concentrated in a range of 0.05 – 4.00 mg/ml via centrifugation and resuspended in 1% sodium alginate. Gel samples were each prepared in a 10 ml Pyrex glass beaker. Samples were immediately subjected to illumination from a continuous wave 808 nm diode laser (Laserglow Technologies, Toronto, Canada) connected to fiber optic that was positioned directly over the sample.[340] The beam spot was adjusted to 1 cm in diameter. A Forward-Looking Infrared (FLIR) Camera (Teledyne FLIR, Wilsonville, OR, USA) was placed on a lab jack horizontal to the beaker. The laser,

set to the desired power settings, was turned on. FLIR video recordings were taken using FLIR tools+ (Teledyne FLIR, Wilsonville, OR, USA) to monitor changes in sample temperature. Following sample illumination, the laser emission and beam spot were turned off. FLIR video recordings were taken as the sample cooled for 1000 seconds. The sample was removed from the beaker, and the mass documented.

7.2.3 Quantification of Gold Concentration

To quantify gold concentrations with ICP-OES, 3 µl of GNS in sodium alginate or ~1.3 g of gel + GNS treated tissue post-staining were digested in 1 or 4 ml, respectively, of freshly prepared aqua regia solution using trace metal grade nitric and hydrochloric acid (1:3, Thermo Fisher Scientific, Waltham, MA, USA). After complete digestion (30 min for GNS samples and 12 hrs for tissue), 2 or 9 ml of standard diluent (10% hydrochloric acid and 1% nitric acid in MilliQ water) was added, respectively, and the sample analyzed. Yttrium (Sigma Aldrich, St. Louis, MO, USA, 01357) was included as an internal standard for all measurements. Exact sample concentrations were extrapolated from gold (Au) calibration curves obtained using a 1000 µg/ml Au calibration standard in 10% hydrochloric acid (Perkin Elmer, Waltham, MA, USA, N9303759). Gold emission was measured at wavelengths of 242.794 nm and 267.594 nm, and the data averaged.

7.2.4 Tissue temperature measurements with nanoparticles in porcine left ventricular tissue

The photothermal heating ability of gel containing GNS was tested in porcine cardiac tissue. The left ventricle of a fresh frozen porcine heart (Animal Technologies, Inc., Tyler, TX, USA) was dissected from the epicardium to the endocardium into approximately 2x2x2 cm pieces. Each piece of tissue was positioned with the endocardium facing upwards. The fiber optic cable, extending from the 808 nm diode laser, was then positioned over the center of the tissue to produce a 1 cm beam spot. Using a syringe pump (Legato111, Kd Scientific, Holliston, MA, USA) placed parallel to the tissue sample, gel alone or gel containing GNS was inserted in the tissue with an 18G needle placed centrally from the side. A thermocouple probe (Allied Electronics, Fort Worth, Texas, USA, 4437973) was placed within the tissue horizontally parallel to the needle. The laser

was turned on directly to the desired power setting (5.0W) along with simultaneous injection of gel or gel containing GNS into the tissue using a syringe pump set at a 500 µl/min flow rate. A circulating bath of normal saline heated to 37 °C was maintained throughout the illumination period (Figure 7.1). Temperature measurements were recorded every 10 s using a thermocouple for a 1000 s illumination period. Subsequently, laser emission was turned off while temperature measurements remained ongoing for an additional 1000 s to monitor heat dissipation.

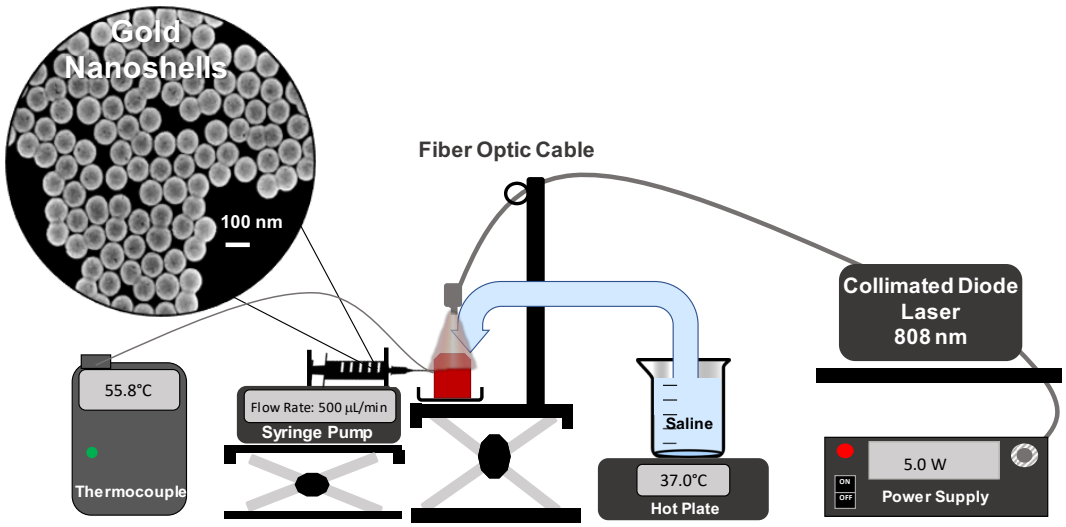

Figure 7.1 Experimental setup of samples excited with NIR light.

7.2.5 Tissue Staining and Lesion Assessment

2,3,5-Triphenyltetrazolium chloride (TTC) (Sigma-Aldrich, St. Louis, Missouri, USA, T8877) solution was used to show macroscopic damage and lesion generation due to photothermal ablation. The staining solution was prepared as described by Bhaskaran *et al.*[341] by dissolving 2% (w/v) TTC in MilliQ water, protected from light, and placed on a stir plate at room temperature for at least 30 minutes before use.

Following ex vivo ablation, the tissue was dissected from the endocardium to the epicardium along the needle tract using a blade, to expose embedded gel and any lesion formation. Both tissue sections (labeled left or right) were then submerged in 2% TTC staining solution and incubated for 1 hour at 37 ˚C. Each sample was then blotted dry to remove any excess stain. Samples were

photographed and either immediately imaged with micro-computed tomography, stored in 10% neutral buffered formalin (StatLab, McKinney, TX, USA, Cat# 28600-1) for histochemical analysis, or frozen at -80 ˚C for gold quantification with ICP-OES.

7.2.6 Measurements of ablation lesion

Ablation lesions were manually traced on each sample in ImageJ (https://imagej.nih.gov). Measurements of maximal depth, width, diameter of surface lesion, and area of myocardium lesion were measured. Volume (cm^3) was calculated following the work of Eick and Bierbaum [342] using an ellipsoid assumption where V=1/6 π*depth*width*surface diameter.

7.2.7 Micro-computed tomography imaging of tissue

To confirm retention of the calcium alginate gel containing GNS within tissue and assess particle distribution, ex vivo porcine myocardium infused with calcium alginate gel + GNS were imaged using a Siemens Inveon High-Resolution Micro-Computed Tomography (μCT) imaging system (Siemens, Munich, Germany). The tissue was imaged at baseline and after gel + GNS infusion with NIR light illumination following the parameters described by Terracciano *et al* [343]. The images were exported as Digital CT images (DICOM files) for analysis and 3D reconstructed using 3Dslicer (https://www.slicer.org/).

7.2.8 Statistical Analysis

GraphPad Prism 9 (Version 9.1.1: GraphPad software, Inc., San Diego, California, USA) was used for statistical analyses. Comparison of lesion dimensions and volumes were analyzed via unpaired t-test.

7.3 Results

7.3.1 Nanoparticle Photothermal Kinetics

NIR light illumination (808 nm) as described above was performed on gel alone and gel + GNS samples in order to determine peak temperature rise and time to 50 ºC (temperature needed for permanent cell death) (Figure 7.2).

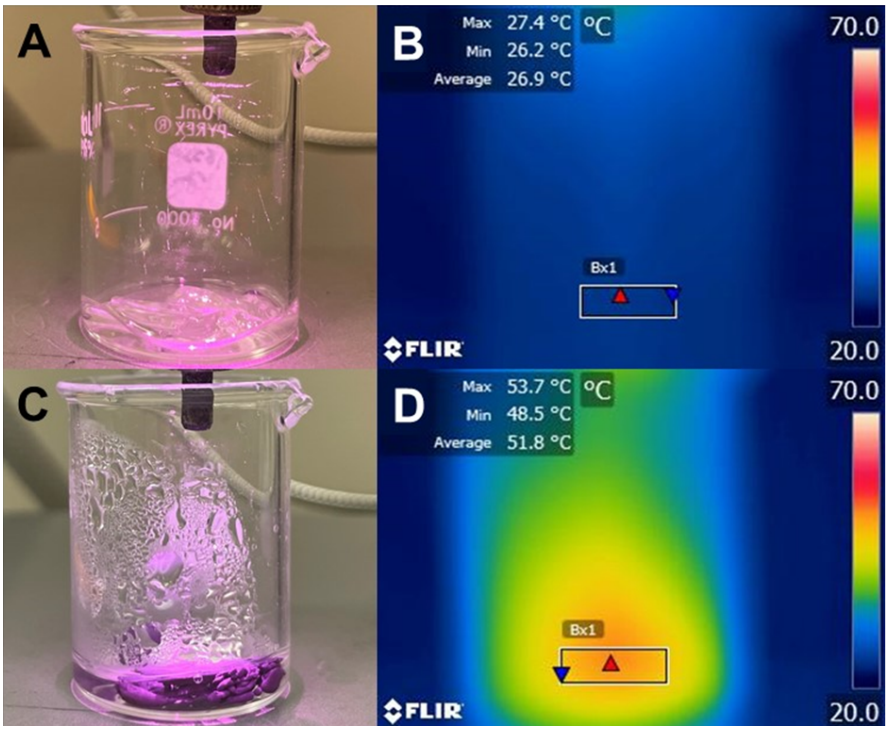

Figure 7.2 GNS in gel required to reach 50 ºC with NIR light. Images taken under illumination (A, C) and FLIR (B, D) at 1000 s (5.0W) for (A, B) gel and (C, D) gel + GNS 4 mg [Au]/ml.

When compared to gel alone, gel + GNS reached temperatures >50 ºC with ≥0.375 mg/ml GNS concentration at 5.0W (Figure 7.3B). Power of 4.0W (Figure 7.3A) did not lead to temperatures >50ºC at any of the GNS concentrations. Time to 50ºC at 5.0W was 88.2±17.7 s at 3.00 mg/ml and 48.5±4.4 s at 4.00 mg/ml. Further, peak temperatures with 5.0W power were 54.5±2.0 ºC and 57.4±2.9 ºC at 3.00 mg/ml and 4.00 mg/ml GNS concentrations, respectively. Over the 1000 s duration, the temperature remained >50 ºC, highlighting a potential property of maintaining temperatures >50 ºC without further marked temperature rises. Temperatures returned to baseline (Figure 7.3C,D) with 4.00 mg/ml GNS concentration at 5.0W after 246.4±25.7s. To determine which conditions (GNS

concentration and power) resulted in a time to reach 50 ºC in under 60 s, gel infusion with GNS and NIR light illumination was performed. It was found that concentrations ≥3.00 mg/ml at 5.5W and ≥4.00 mg/ml at 5.0W were needed to achieve rapid heating within 60 s. Importantly, it was noted that modifying concentration had a greater effect on time to 50 ºC than changing the power.

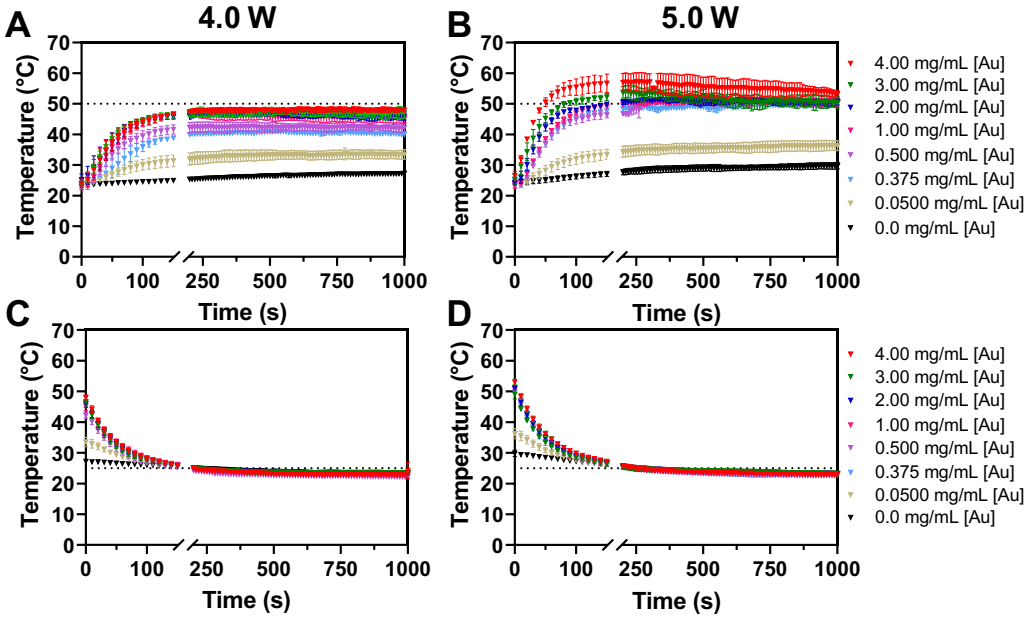

Figure 7.3 Temperature as a function of time for gel + GNS with NIR light illumination for over 1000 s at (A) 4.0W and (B) 5.0W and return to ambient post-illumination at (C) 4.0W and (D) 5.0W. Dashed lines represent 50 ºC and 25 ºC, respectively.

7.3.2 Ex Vivo Porcine Photothermal Ablation

To assess the photothermal heating properties of the gel + GNS within ventricular myocardial tissue, tissue samples underwent simultaneous photothermal ablation and gel + GNS infusion. When compared to gel alone, gel + GNS samples (n=12) resulted in consistent tissue temperatures >50 ºC (Figure 7.4A). Time to 50 ºC was 287.5±63.9 s with an average peak temperature of 57.8±3.7 ºC, which remained plateaued throughout illumination. Conversely, gel solution alone had a peak temp of 45.7±4.5 ºC over the same light exposure and reached 50 ºC transiently in only one sample.

Once light exposure ceased, the tissue temperature in samples containing gel and gel + GNS decreased back to baseline in roughly 300 s (Figure 7.4B). Despite initial higher temperatures in the gel + GNS tissue samples, there was a marked reduction in tissue temperatures compared to gel alone in the first 120 s, implying temperature reduction was a result of particle cooling aside from just passive cooling after light exposure. To assess GNS retention and distribution in treated tissue, μCT was performed at baseline and after GNS infusion with light illumination (Figure 7.4D).

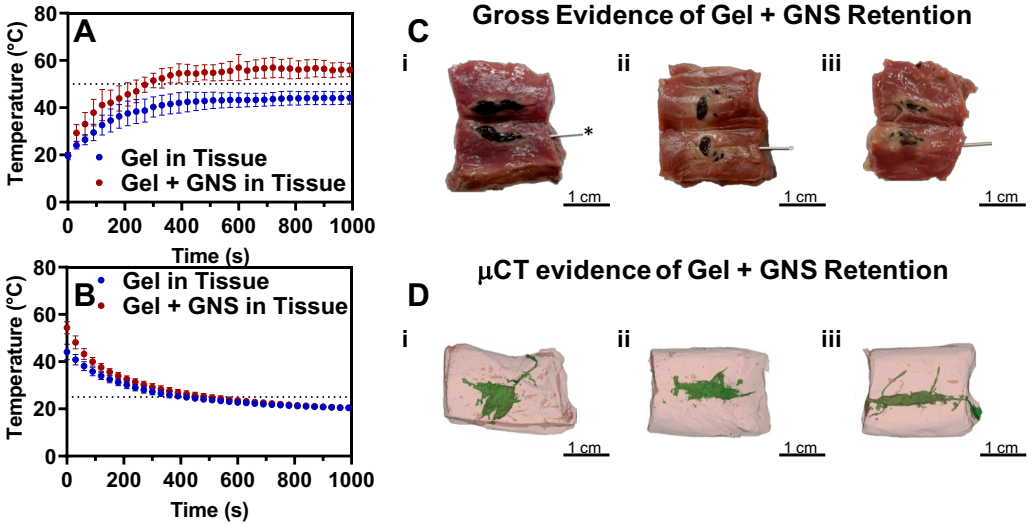

Figure 7.4 Intramyocardial gel + GNS heating and retention. Temperature measurements (A) during and (B) post-illumination (5.0W) in tissue infused via needle (*) with gel alone (blue) or gel + GNS (red). Data plotted as mean±SD. Dashed lines represent 50 ºC and 25 ºC, respectively. (C) Photographs of gel + GNS penetration (dark area) and (D) 3D tissue reconstructions (top view) (i-iii) post-treatment with gel + GNS (green).

There is evidence of GNS retention (dark green regions) within the ventricular myocardium. Unlike hollow gold nanoshells which change their morphology under NIR light and can be used to release therapeutics,[344], [345] silica-gold nanoshells remain stable. Total gold concentration by mass of gold per weight of tissue (n=3, samples without TTC staining) was 245.5±37.8 μg [Au]/g tissue. Based on GNS concentration and total volume infused, this represents 79.3±15.4% of GNS retention within the myocardium samples. Figure 7.5 represents sampling (n=3) of photothermal ablation lesions with gel alone versus gel + GNS with NIR light exposure.

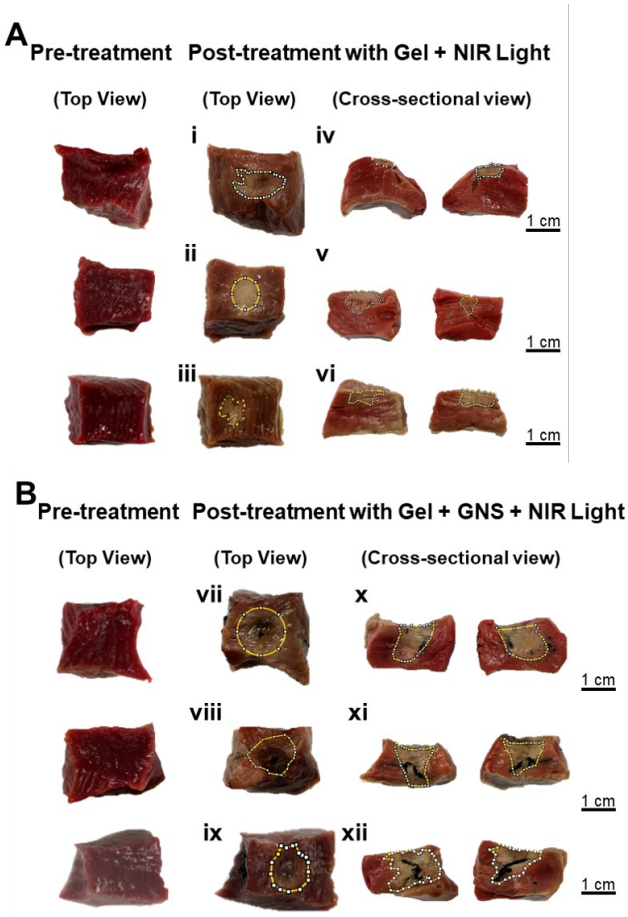

Figure 7.5 Cardiac lesions with NIR light-mediated gel + GNS photothermal heating (808 nm). Photographs pre-treatment and post-treatment with (A) gel or (B) gel + GNS and light. Endocardial view following treatment with illumination and infusion with (i-iii) gel or (vii-ix) gel + GNS. Following treatment, tissue was bisected and stained with 2% TTC. Cross-sectional view of tissue treated with illumination and (iv-vi) gel alone with larger lesions produced in (x-xii) gel + GNS samples.

With TTC staining, there is gross evidence of larger ablation lesions with gel + GNS compared to gel alone and all samples (n=12) treated with gel + GNS and NIR light resulted in lesion formation. Lesion dimensions were measured from all samples treated with gel + GNS and NIR light. When compared to gel alone, treatment with gel + GNS resulted in greater lesion depth (0.86±0.3 vs. 0.50±0.3 cm, $p<0.0001$), width (1.21±0.2 vs. 0.59±0.1 cm, $p<0.0001$), and diameter (1.19±0.3 vs. 0.82±0.1 cm, $p<0.0001$). Further, calculated lesion volumes were also larger with gel + GNS treatment compared to gel alone (0.68±0.4 vs. 0.13±0.1 cm3, $p<0.0001$) (Figure 7.6).

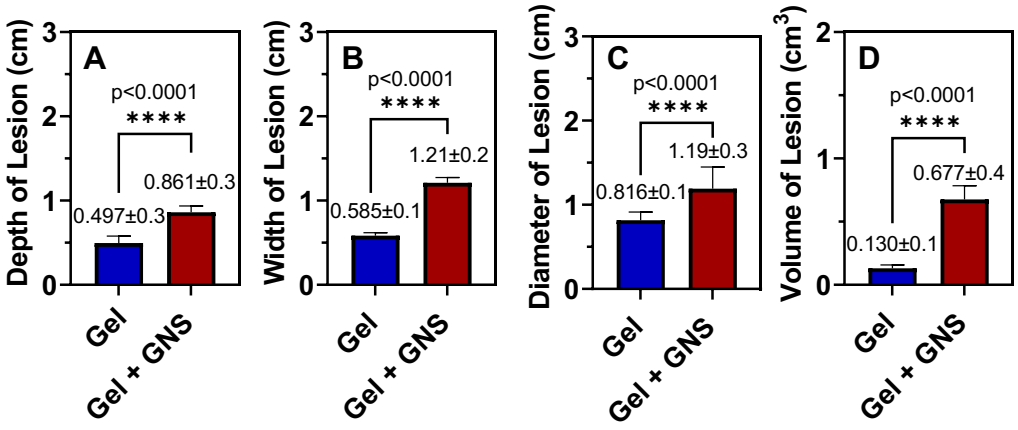

Figure 7.6 Measurements of maximal depth, width, and surface diameter and calculated volume of lesions. Lesion measurements (mean±s.e.m.) were obtained via ImageJ (n=12). Tissues treated with illumination and gel + GNS showed significant increases in lesion depth (A), width (B), diameter (C), and volume (D) compared to tissue treated with illumination and gel alone.

7.4 Discussion

The major findings of this study are 1) NIRS gold nanoshells exposed to light at their resonant wavelength (808 nm) induced particle heating at temperatures >50 ºC and 2) *ex vivo* myocardial ventricular tissue infused with resonant nanoshells and exposed to NIR light led to significantly greater photothermal ablation compared to tissue exposed to NIR light alone.

Photothermal ablation via NIRS nanoparticles has already shown early promise in the treatment of various forms of solid tumors, such as head and neck and prostate cancers [338], [346], [347]. PEGylated gold-silica nanoshells have been well-tolerated in both pre-clinical [346] and clinical [348] studies with no indication of toxicities or bioincompatibilities and PEGylated solid gold nanoparticles have specifically no toxicities on primary neonatal rat cardiomyocytes [349]. Further, the calcium-alginate hydrogel used is also biocompatible and shows degradation in soft tissue within 4-6 weeks, [350] allowing for prolonged retention yet subsequent removal. Using the concept of conversion of NIR light-to-thermal energy leading to cancer cell death, NIRS nanoparticles when exposed to their resonant wavelength can create a thermal effect to ablate abnormal myocardium causing cardiac arrhythmias. Within the realm of cardiac arrhythmia management, various studies

have suggested nanoparticle properties may have a therapeutic role. Prior work by Nguyen *et al*. [351] showed magnetic nanoparticles could increase RF ablation lesions in both *ex vivo* and *in vivo* models. In this study, iron nanoparticles were infused into myocardium and with RF, led to increased lesions compared to RF alone. Further, *in vivo* magnetic attraction of iron nanoparticles within heat-sensitive liposomes were able to guide particles to a region of interest with increased lesion size [351]. Given the underlying limitations of RF, including lesion depth within scar and need for continuous contact, the exact role of nanoparticle-aided RF remains unclear.

Our study assessed the role of NIRS nanoparticles for direct photothermal ablation of cardiac myocardium. The potential advantage of this approach is that NIR light can penetrate tissue >1 cm *without* direct contact with tissue, potentially leading to nanoparticle-guided tissue cell death at depths beyond current RF ablation. Our results showed significant increase in lesion depth/volume compared to light exposure alone, confirming the effect is due to nanoparticle-mediated photothermal ablation as opposed to light alone.

As seen in our study, NIR light alone can lead to direct tissue heating and ultimately cell death. Photon absorption of light in tissue leads to tissue heating. Prior work by D'Avila *et al.*[352] have shown the role of direct ventricular tissue ablation using a 1064 nm laser light source led to transmural ventricular lesions [352], [353]. Further, a slower rate of volumetric heating and/or inclusion of a diffused tip has been shown to create deeper ventricular ablation lesions [354]. The concern, however, is that the continuous light source illuminated for long duration could lead to "steam pops" and/or cardiac perforation, and depth is difficult to control. Given that photon absorption is dependent on tissue constituents, infarcted myocardium may have different absorption properties. Collagen within myocardial scar can scatter and absorb NIR light, which could lead to even larger lesions as photothermal heating could occur more broadly. With NIRS nanoparticles present, theoretically lower power and/or duration of light exposure would result in significant cardiac lesions in a region of interest with an improved safety profile.

Aside from lesion creation, another promising finding during photothermal ablation was the tissue temperature profile. There were consistent tissue temperatures >50 ºC. This is a critical temperature to achieve a durable ablation lesion. More importantly, this temperature was maintained in a range of roughly 50-60 ºC without continued rise over 1000 seconds (>16 minutes).

The *ex vivo* data set presented here will now provide the framework for future *in vivo* evaluation of parameters, such as 1) light delivery to a beating heart through tissue and blood; 2) nanoshell delivery (including guidance with electroanatomic mapping) and retention in the region of interest; 3) risks of collateral damage; and 4) nanoshell perfusion to infarcted tissues.

7.5 Clinical Applications of Near-Infrared Sensitive Nanoshell Photothermal Ablation

The use of adjunctive ablation techniques highlights the current limitations of RF in various forms of VT ablation. For instance, patients with a known septal and/or epicardial substrate often have lower success rates due to the inability of RF lesions to penetrate ventricular tissue. In this patient population, the ability to deliver photothermal ablation lesions to deeper regions from the endocardial surface could potentially improve outcomes and reduce complications. Further, the light source would be from a fiber optic cable which could be inserted into the heart like standard catheters and also directed to a region of interest. Additionally, the light source would not need continuous tissue contact as required by RF. This *directed* photothermal ablation could overcome the limitations of bipolar ablation which requires multiple catheters in a region of interest as well as chemical ablation that can only be achieved if a suitable coronary venous branch is present. Aside from a directed light source, nanoparticle myocardial retention remains a key hurdle to overcome. Further studies using either known cardiac targets in an infarcted heart [355], such as angiotensin II type 1 receptor [356], myosin [357], or phosphatidylserine [358], or novel site-specific ligands may better allow for future clinical studies as immunotargeting with nanoshells has been demonstrated for overexpression of HER2, a clinically relevant cancer biomarker [359], [360].

7.6 Limitations

Several limitations should be noted of the presented data. First, we chose an 808 nm wavelength light source, however the isosbestic point (maximal absorption) of total hemoglobin lies in this range which could make in vivo applications more difficult. Second, it is unknown if this would be an optimal wavelength for ventricular scar, warranting future investigation of different NIR light properties

and settings. Longer wavelengths (1064 nm) would have greater absorption in collagen (i.e. myocardial scar) and therefore, it is unknown which specific wavelength is optimal. Third, the exact depth of light and particle heating in myocardial scar is unknown and warrants further study. Fourth, the role of tissue impedance and its correlation with lesion formation with this ablation technology is unknown and would need to be investigated. Fifth, the dissipation of heat beyond the zone of illumination and particle delivery site needs to be studied and correlated with particle diffusion. Finally, although NIRS nanoparticle ablation is being used clinically to treat various cancers and pre-clinical studies have shown that intravenous administration of PEG-coated nanoshells (same as our study) are excreted or scavenged by the liver, spleen, and kidneys [346], [361], [362], metal retention within the heart and other organs would need to be studied in vivo to ensure no toxicity.

7.7 Conclusions

Near-infrared sensitive nanoparticle photothermal ablation is feasible in ex vivo ventricular myocardium. Further studies are warranted for a potential clinical role in the treatment of cardiac arrhythmias.

Chapter 8

Discussion and Conclusion

8.1 Clinical Translation of GNPs

Clinical translation of gold nanoparticles depends on several factors. Of the current clinical trials being performed for surface modified nanoparticles used in drug delivery [363], many are failing to complete phase II for mainly two reasons: (1) high immune clearance rates that compromise targeting, (2) the nanoparticle surface and resulting protein corona, which may alter drug release. While laboratory-scale surface modified gold nanoparticles have led to promising results in drug delivery applications, some of these studies have failed their intention to mitigate the rapid clearance as well as understanding the pathological interactions of the particle with the biological system [364]. In fact, pervasive interactions of the particles with a vastly complex immunological system have resulted in the rapid clearance of nanoparticles, representing the primary obstacle for the clinical translation of nanoparticle drug-delivery systems. Surface modifications and functionalization of GNPs are engineered to manipulate biological interactions with the particle as well as to increase retention and circulation time, target a desired tissue, as we demonstrated in our papers using surface passivated GNP in a mouse model of lung cancer. We demonstrated that surface functionalizations such as surface protein addition, and pH or ion sensitivity (Chapter 3), PEGylation (Chapter 4), overall charge (Chapter 6) significantly improve cancer cell targeting as well as particle's retention time within the tumor.

The other issue related with clinical translation of GNPs is the protein corona around the particle surface which masks the bulk nanoparticle material, de-stabilizes the particle, and ultimately directs the biological response to the nanoparticle. In fact, without any surface modification, nanoparticles immersed in a biological media attract body proteins almost immediately (<0.5 min) which cover their surface forming a layer or multi-layers. With this protein corona shielding their surface, GNP are recognized by phagocytes through a process called opsonization. Therefore, protein corona contributes to a lack of clinical translatability, limiting their applications in cancer drug delivery. In this thesis, protein corona is well investigated in Chapter 3, in which an adsorption model of proteins on the particle surface is evaluated and tested on biological media. We discovered that protein corona is altered from the media pH of the solution. In fact, when pH varies from 4.7 to 8.5, we observed an increase in the maximum amount of adsorbed protein molecules on a GNP surface, possibly due to the transition from monolayer to multilayer protein immobilization. The interaction with the cationic nebula is the likely reason for the rapid growth in BSA accumulation at pH 8.5. In addition, our

results indicate that GNPs are highly stable within a pH range 4.7 - 7, which is suitable for in vivo administration in a clinical setting. These findings will help clinical translation of gold nanoparticles in clinical settings.

To date, many types of cancer are detected at an advanced stage, when treatment options are limited, and prognosis is unfortunate. Being able to detect cancers at their early stages can substantially improve survival rates other than improving the quality of life of these patients. However, this approach is clinically challenging, encountering the possibility of harmful overdiagnosis and overtreatment. As early detections and precise diagnoses are urgently needed in oncology, imaging modalities such as computed tomography (CT), magnetic resonance imaging (MRI), and positron emission tomography (PET) are currently the fasted and least invasive methodologies employed to detect cancer diseases. Unfortunately, conventional contrast agents are often small molecules that are quickly metabolized and sometimes exert potentially toxic effects. To overcome drawbacks risen from the use of traditional contrast agents, we investigated GNP as innovative imaging contrast agents to support early diagnosis, which can be tracked over time due to their high X-ray absorption. Although additional research is needed to clarify the clearance time of the particles and potential side effects over a long period of time, this work contributed to the scientific knowledge of particle distribution depending on their surface passivation on different areas of the tumor and making progressing toward clinical translation of nanomedicine.

Finally, another factor to be considered toward GNP clinical translation is the unpredictable high cost of the gold. In fact, the optical properties of gold are highly dependent on expensive and complicated surface chemistry and their clinical use is discouraged by their rising costs. Additionally, to accelerate the clinical translation the commercial and practical feasibility, the clinical development feasibility, as well as the bridging of preclinical toxicology to patient safety and lastly the proper management of chemistry, manufacturing and quality control are other key points that need to be addressed.

8.2 Summary and Future Prospective

GNPs have proven to be promising candidates for biomedical applications, such as imaging, diagnostics, and therapeutics, because of their relative ease of synthesis and surface modification as well as their physicochemical properties. Spherical gold nanoparticles, gold nanorods, and gold nanoshells were selected and studied in this thesis to further investigate different approaches of surface passivation in more detail as a means to overcome the limitations that have hampered the clinical translation of gold-based nanomedicine.

Further knowledge is provided regarding the interactions between nanomaterials comprised of gold and the tumor microenvironment as well as innovative strategies to overcome solid tumor heterogeneity through theranostic platforms. We have shown that gold-based systems are trackable inside the body using imaging techniques and these materials can be modified to distribute site-specifically in areas of interest within and surrounding the tumor. The studies presented here demonstrate that various chemical moieties can be conjugated to the surface of GNPs which results in differences in the nanoparticle tissue distribution patterns. Information about how surface functionalization affects nanoparticle intratumoral distribution as described in this thesis provides important evidence on directing GNPs to specific zones locally, such as the tumor stroma, which has a critical role in tumorigenesis, cancer progression, metastasis, and chemotherapy resistance. Engineering the surface chemistry of GNPs to direct their transport behavior within the tumor microenvironment would be highly advantageous for directing anticancer therapies, as GNPs could carry such cargo to specific regions of the tumor where biomarkers are overexpressed. Directed cargo delivery within a tumor offers a future medical approach for drug administration to distinct areas of the tumor where major cancer targets reside.

In addition to studies on isotropic gold substrates, we also explored the effects of surface modifications for anisotropic particles, such as gold nanorods (GNRs). Surface modifications of GNRs were performed by reducing the presence of the cationic surfactant, CTAB, and increasing the presence of the anionic surfactant, SDS, as an alternative means to stabilize the particles. It was shown that this modification decreases the cytotoxic effects resulting from surfactant stabilization during particle synthesis. It was also shown that both lung and cervical cancer cells not only tolerated the presence of GNRs but also maintained their cell viability.

These results demonstrate that control over nanoparticle surface functionality can accelerate the utilization of GNRs and other anisotropic particles in clinical research. Although removing the presence of cationic surfactants such as CTAB as much as possible by switching to other nontoxic surfactants is an excellent way to reduce the toxicity of GNRs, developing alternative simple and convenient protocols to reduce toxicity without affecting particle shape is still worthy of further studies. Other challenging issues that current and future research need to address include developing a better understanding of the exact mechanisms that govern growth-directing surfactants towards the fabrication of nanoparticles with different morphologies as well as size control in the growth process, since issues with control over aspect ratio and polydispersity have decelerated large scale nanorod production hampering their clinical translatability [365].

Finally, in this thesis silica-core gold-shell nanoparticles passivated with PEG are exploited as photothermal conversion materials. We demonstrate their use in generating local heat in cardiac tissue within a clinically relevant duration of time (<60 seconds) as well as their ability to create lesions in myocardial tissue. Localized delivery of metal nano-complexes to abnormal tissue for lesion generation may reduce complications in patients undergoing cardiac ablation procedures while improving outcomes in clinical applications. Additionally, the presence of a gold shell increases the possibility of adding cargo molecules or probes to the surface of the particles for an added diagnostic or therapeutic benefit. These colloids are highly suitable for biomedical therapies, sensing applications, remote actuation, and other technological applications [366].

However, this study presents some limitations that it's worth mentioning in this section. For instance, it would have been interesting to compare BSA-GNP behavior to HA-GNP distribution in vivo. However, since the scope of the two investigations was to deepen the knowledge into the surface GNP characteristics when injected intratumorally and how they affect particle distribution, we used two different experimental/analytical approaches to share the obtained results. For BSA-GNP investigation, we focused on protein adsorption on GNP surface depending on the pH of the solution and finding a more suitable experimental approach to visualize and track the particles using CT imaging and how make the experimental setup reproducible and reduce as much as possible the human biases. Once assessed a protocol that minimized the error and biases, in the HA-GNP study we focalized the attention on particle localization in specific areas of the tumor after intratumoral injection, localizing and identifying the preferential areas of particle

accumulation due to the HA passivation. However, differences between protein coating and HA coating must be assessed in future investigations.

Another limitation is the size of the spherical GNPs, which must be increased from 40 nm to 100 nm to resonate at NIR and used for deep tissue illumination as show in Chapter 7 with the nanoshells. Further work must be done to gain more knowledge from particle distribution on different size in cancer applications. In vivo imaging in mice as well as ex vivo analysis with inductively coupled plasma optical emission spectroscopy (ICP-OES) have previously demonstrated the effect of gold nanoparticle size on animal biodistribution indicating that 15 nm diameters or smaller have long blood circulation times, while larger diameters accumulated in the liver and spleen more rapidly [28]. However, no previous study has investigated particle size effect on intratumoral distribution.

Moreover, non-orthotopic tumor masses can significantly differ from orthotopic models in terms of cell density and organization, immune cell infiltration, and overall tumor perfusion. While local administration of nanoparticles in tumor areas is the key point of this study, local delivery is not available in all clinical scenarios. Further experimental studies must keep in mind these differences and keep into account those variables when designing pre-clinical experiments. Indeed, this work is a proof-of-principle, which eventually will be extended to other nanoparticles and tumor models.

Overall, the work presented in this thesis further demonstrates that engineering the GNP surface as well as exploiting the physicochemical properties of GNPs can enhance their biodistribution in heterogeneous tissues, enabling them as valuable tools for different applications. The desire for researchers to fundamentally understand and characterize the interactions between molecules and nanostructures as well as nanomaterials and biological environments will fuel advancement of their applications in the scientific and medical fields, ranging from new protocols for pre-clinical research to specific drug products undergoing clinical trials.

References

[1] C. Contado, "Nanomaterials in consumer products: a challenging analytical problem," *Front Chem*, vol. 3, p. 48, Aug. 2015, doi: 10.3389/fchem.2015.00048.

[2] S. H. Lee and B.-H. Jun, "Silver Nanoparticles: Synthesis and Application for Nanomedicine," *Int J Mol Sci*, vol. 20, no. 4, p. E865, Feb. 2019, doi: 10.3390/ijms20040865.

[3] M. Mabrouk, S. H. Kenawy, G. E.-T. El-bassyouni, A. A. E.-F. Ibrahim Soliman, and E. M. Aly Hamzawy, "Cancer Cells Treated by Clusters of Copper Oxide Doped Calcium Silicate," *Adv Pharm Bull*, vol. 9, no. 1, pp. 102–109, Feb. 2019, doi: 10.15171/apb.2019.013.

[4] R. K. Kawassaki, M. Romano, N. Dietrich, and K. Araki, "Titanium and Iron Oxide Nanoparticles for Cancer Therapy: Surface Chemistry and Biological Implications," *Frontiers in Nanotechnology*, vol. 3, 2021, Accessed: Aug. 31, 2022. [Online]. Available: https://www.frontiersin.org/articles/10.3389/fnano.2021.735434

[5] K. Sztandera, M. Gorzkiewicz, and B. Klajnert-Maculewicz, "Gold Nanoparticles in Cancer Treatment," *Mol. Pharmaceutics*, vol. 16, no. 1, pp. 1–23, Jan. 2019, doi: 10.1021/acs.molpharmaceut.8b00810.

[6] V. Amendola, R. Pilot, M. Frasconi, O. M. Maragò, and M. A. Iatì, "Surface plasmon resonance in gold nanoparticles: a review," *J. Phys.: Condens. Matter*, vol. 29, no. 20, p. 203002, Apr. 2017, doi: 10.1088/1361-648X/aa60f3.

[7] A. Liang, Q. Liu, G. Wen, and Z. Jiang, "The surface-plasmon-resonance effect of nanogold/silver and its analytical applications," *TrAC Trends in Analytical Chemistry*, vol. 37, pp. 32–47, Jul. 2012, doi: 10.1016/j.trac.2012.03.015.

[8] S. Link and M. A. El-Sayed, "Optical Properties and Ultrafast Dynamics of Metallic Nanocrystals," *Annual Review of Physical Chemistry*, vol. 54, no. 1, pp. 331–366, 2003, doi: 10.1146/annurev.physchem.54.011002.103759.

[9] C. J. Murphy *et al.*, "Chemical sensing and imaging with metallic nanorods," *Chem. Commun.*, no. 5, pp. 544–557, Jan. 2008, doi: 10.1039/B711069C.

[10] X. Fan, W. Zheng, and D. J. Singh, "Light scattering and surface plasmons on small spherical particles," *Light Sci Appl*, vol. 3, no. 6, Art. no. 6, Jun. 2014, doi: 10.1038/lsa.2014.60.

[11] M. Sharifi *et al.*, "Plasmonic gold nanoparticles: Optical manipulation, imaging, drug delivery and therapy," *Journal of Controlled Release*, vol. 311–312, pp. 170–189, Oct. 2019, doi: 10.1016/j.jconrel.2019.08.032.

[12] K. Yue, J. Nan, X. Zhang, J. Tang, and X. Zhang, "Photothermal effects of gold nanoparticles induced by light emitting diodes," *Applied Thermal Engineering*, vol. 99, pp. 1093–1100, Apr. 2016, doi: 10.1016/j.applthermaleng.2016.01.077.

[13] R. Meir *et al.*, "Nanomedicine for Cancer Immunotherapy: Tracking Cancer-Specific T-Cells in Vivo with Gold Nanoparticles and CT Imaging," *ACS Nano*, vol. 9, no. 6, pp. 6363–6372, Jun. 2015, doi: 10.1021/acsnano.5b01939.

[14] S. Svenson, "Theranostics: Are We There Yet?," *Mol. Pharmaceutics*, vol. 10, no. 3, pp. 848–856, Mar. 2013, doi: 10.1021/mp300644n.

[15] R. Terracciano, D. Demarchi, M. Ruo Roch, S. Aiassa, and G. Pagana, "Nanomaterials to Fight Cancer: An Overview on Their Multifunctional Exploitability," *J Nanosci Nanotechnol*, vol. 21, no. 5, pp. 2760–2777, May 2021, doi: 10.1166/jnn.2021.19061.

[16] D. F. Jackson and D. J. Hawkes, "X-ray attenuation coefficients of elements and mixtures," *Physics Reports*, vol. 70, no. 3, pp. 169–233, Apr. 1981, doi: 10.1016/0370-1573(81)90014-4.

[17] A. M. Bucher *et al.*, "Is Contrast Medium Osmolality a Causal Factor for Contrast-Induced Nephropathy?," *Biomed Res Int*, vol. 2014, p. 931413, 2014, doi: 10.1155/2014/931413.

[18] B. M. Yeh *et al.*, "Opportunities for new CT contrast agents to maximize the diagnostic potential of emerging spectral CT technologies," *Adv Drug Deliv Rev*, vol. 113, pp. 201–222, Apr. 2017, doi: 10.1016/j.addr.2016.09.001.

[19] S. Ahn, S. Y. Jung, and S. J. Lee, "Gold Nanoparticle Contrast Agents in Advanced X-ray Imaging Technologies," *Molecules*, vol. 18, no. 5, pp. 5858–5890, May 2013, doi: 10.3390/molecules18055858.

[20] J. Beik *et al.*, "Gold nanoparticles in combinatorial cancer therapy strategies," *Coordination Chemistry Reviews*, vol. 387, pp. 299–324, May 2019, doi: 10.1016/j.ccr.2019.02.025.

[21] T. Vo-Dinh *et al.*, "Shining Gold Nanostars: From Cancer Diagnostics to Photothermal Treatment and Immunotherapy," *Journal of Immunological Sciences*, vol. 2, no. 1, Jan. 2018, Accessed: Sep. 02, 2022. [Online]. Available: https://www.immunologyresearchjournal.com/articles/shining-gold-nanostars-from-cancer-diagnostics-to-photothermal-treatment-and-immunotherapy.html

[22] J. R. Ashton, E. B. Gottlin, E. F. Patz, J. L. West, and C. T. Badea, "A comparative analysis of EGFR-targeting antibodies for gold nanoparticle CT

imaging of lung cancer," *PLoS One*, vol. 13, no. 11, p. e0206950, 2018, doi: 10.1371/journal.pone.0206950.

[23] D. Rand *et al.*, "Nanomaterials for X-ray Imaging: Gold Nanoparticle Enhancement of X-ray Scatter Imaging of Hepatocellular Carcinoma," *Nano Lett.*, vol. 11, no. 7, pp. 2678–2683, Jul. 2011, doi: 10.1021/nl200858y.

[24] J. F. Hainfeld, D. N. Slatkin, T. M. Focella, and H. M. Smilowitz, "Gold nanoparticles: a new X-ray contrast agent," *Br J Radiol*, vol. 79, no. 939, pp. 248–253, Mar. 2006, doi: 10.1259/bjr/13169882.

[25] D. Kim, S. Park, J. H. Lee, Y. Y. Jeong, and S. Jon, "Antibiofouling Polymer-Coated Gold Nanoparticles as a Contrast Agent for in Vivo X-ray Computed Tomography Imaging," *J. Am. Chem. Soc.*, vol. 129, no. 24, pp. 7661–7665, Jun. 2007, doi: 10.1021/ja071471p.

[26] C. Xu, G. A. Tung, and S. Sun, "Size and Concentration Effect of Gold Nanoparticles on X-ray Attenuation As Measured on Computed Tomography," *Chem. Mater.*, vol. 20, no. 13, pp. 4167–4169, Jul. 2008, doi: 10.1021/cm8008418.

[27] P. Jackson, S. Periasamy, V. Bansal, and M. Geso, "Evaluation of the effects of gold nanoparticle shape and size on contrast enhancement in radiological imaging," *Australas Phys Eng Sci Med*, vol. 34, no. 2, pp. 243–249, Jun. 2011, doi: 10.1007/s13246-011-0071-7.

[28] Y. C. Dong *et al.*, "Effect of Gold Nanoparticle Size on Their Properties as Contrast Agents for Computed Tomography," *Scientific Reports*, vol. 9, no. 1, pp. 1–13, Oct. 2019, doi: 10.1038/s41598-019-50332-8.

[29] K. Shamalov, R. Meir, M. Motiei, R. Popovtzer, and C. J. Cohen, "Noninvasive Tracking of Natural Killer Cells Using Gold Nanoparticles," *ACS Omega*, vol. 6, no. 43, pp. 28507–28514, Nov. 2021, doi: 10.1021/acsomega.1c02143.

[30] C. Yu *et al.*, "Enhanced and long-term CT imaging tracking of transplanted stem cells labeled with temperature-responsive gold nanoparticles," *J. Mater. Chem. B*, vol. 9, no. 12, pp. 2854–2865, Apr. 2021, doi: 10.1039/D0TB02997A.

[31] J. R. Nicol, D. Dixon, and J. A. Coulter, "Gold nanoparticle surface functionalization: a necessary requirement in the development of novel nanotherapeutics," *Nanomedicine (Lond)*, vol. 10, no. 8, pp. 1315–1326, 2015, doi: 10.2217/nnm.14.219.

[32] M. Yu, C. Zhou, J. Liu, J. D. Hankins, and J. Zheng, "Luminescent Gold Nanoparticles with pH-Dependent Membrane Adsorption," *J. Am. Chem. Soc.*, vol. 133, no. 29, pp. 11014–11017, Jul. 2011, doi: 10.1021/ja201930p.

[33] A. Sani, C. Cao, and D. Cui, “Toxicity of gold nanoparticles (AuNPs): A review,” *Biochem Biophys Rep*, vol. 26, p. 100991, Apr. 2021, doi: 10.1016/j.bbrep.2021.100991.

[34] S. Nie, “Understanding and overcoming major barriers in cancer nanomedicine,” *Nanomedicine (Lond)*, vol. 5, no. 4, pp. 523–528, Jun. 2010, doi: 10.2217/nnm.10.23.

[35] S. Christau, T. Möller, F. Brose, J. Genzer, O. Soltwedel, and R. von Klitzing, “Effect of gold nanoparticle hydrophobicity on thermally induced color change of PNIPAM brush/gold nanoparticle hybrids,” *Polymer*, vol. 98, pp. 454–463, Aug. 2016, doi: 10.1016/j.polymer.2016.03.088.

[36] F. Ahmad *et al.*, “Unique Properties of Surface-Functionalized Nanoparticles for Bio-Application: Functionalization Mechanisms and Importance in Application,” *Nanomaterials*, vol. 12, no. 8, Art. no. 8, Jan. 2022, doi: 10.3390/nano12081333.

[37] S. J. Amina and B. Guo, “A Review on the Synthesis and Functionalization of Gold Nanoparticles as a Drug Delivery Vehicle,” *Int J Nanomedicine*, vol. 15, pp. 9823–9857, 2020, doi: 10.2147/IJN.S279094.

[38] A. M. E. Badawy, T. P. Luxton, R. G. Silva, K. G. Scheckel, M. T. Suidan, and T. M. Tolaymat, “Impact of Environmental Conditions (pH, Ionic Strength, and Electrolyte Type) on the Surface Charge and Aggregation of Silver Nanoparticles Suspensions,” *Environ. Sci. Technol.*, vol. 44, no. 4, pp. 1260–1266, Feb. 2010, doi: 10.1021/es902240k.

[39] Y. Chen, Y. Xianyu, and X. Jiang, “Surface Modification of Gold Nanoparticles with Small Molecules for Biochemical Analysis,” *Acc. Chem. Res.*, vol. 50, no. 2, pp. 310–319, Feb. 2017, doi: 10.1021/acs.accounts.6b00506.

[40] K. Mahato *et al.*, “Gold nanoparticle surface engineering strategies and their applications in biomedicine and diagnostics,” *3 Biotech*, vol. 9, no. 2, p. 57, Jan. 2019, doi: 10.1007/s13205-019-1577-z.

[41] J. Zhang, L. Mou, and X. Jiang, “Surface chemistry of gold nanoparticles for health-related applications,” *Chemical Science*, vol. 11, no. 4, pp. 923–936, 2020, doi: 10.1039/C9SC06497D.

[42] R. A. Sperling and W. J. Parak, “Surface modification, functionalization and bioconjugation of colloidal inorganic nanoparticles,” *Philos Trans A Math Phys Eng Sci*, vol. 368, no. 1915, pp. 1333–1383, Mar. 2010, doi: 10.1098/rsta.2009.0273.

[43] J. Gao, X. Huang, H. Liu, F. Zan, and J. Ren, “Colloidal Stability of Gold Nanoparticles Modified with Thiol Compounds: Bioconjugation and Application in Cancer Cell Imaging,” *Langmuir*, vol. 28, no. 9, pp. 4464–4471, Mar. 2012, doi: 10.1021/la204289k.

[44] Z. Zhang, J. Jia, Y. Lai, Y. Ma, J. Weng, and L. Sun, “Conjugating folic acid to gold nanoparticles through glutathione for targeting and detecting cancer cells,” *Bioorganic & Medicinal Chemistry*, vol. 18, no. 15, pp. 5528–5534, Aug. 2010, doi: 10.1016/j.bmc.2010.06.045.

[45] L. Ye and Q. Song, “Promising potency of retinoic acid-poly(ethylene glycol)-thiol gold nanoparticle conjugates for cervical cancer treatment,” *Int J Clin Exp Med*, vol. 8, no. 7, pp. 10501–10507, Jul. 2015.

[46] N. S. Elbialy, M. M. Fathy, and W. M. Khalil, “Doxorubicin loaded magnetic gold nanoparticles for in vivo targeted drug delivery,” *International Journal of Pharmaceutics*, vol. 490, no. 1, pp. 190–199, Jul. 2015, doi: 10.1016/j.ijpharm.2015.05.032.

[47] W.-H. Chen *et al.*, “Therapeutic nanomedicine based on dual-intelligent functionalized gold nanoparticles for cancer imaging and therapy in vivo,” *Biomaterials*, vol. 34, no. 34, pp. 8798–8807, Nov. 2013, doi: 10.1016/j.biomaterials.2013.07.084.

[48] Y. Ding *et al.*, “The performance of thiol-terminated PEG-paclitaxel-conjugated gold nanoparticles,” *Biomaterials*, vol. 34, no. 38, pp. 10217–10227, Dec. 2013, doi: 10.1016/j.biomaterials.2013.09.008.

[49] J. K. Lee *et al.*, “Organ-specific distribution of gold nanoparticles by their surface functionalization,” *Journal of Applied Toxicology*, vol. 35, no. 6, pp. 573–580, Jun. 2015, doi: 10.1002/jat.3075.

[50] W. H. De Jong, W. I. Hagens, P. Krystek, M. C. Burger, A. J. A. M. Sips, and R. E. Geertsma, “Particle size-dependent organ distribution of gold nanoparticles after intravenous administration,” *Biomaterials*, vol. 29, no. 12, pp. 1912–1919, Apr. 2008, doi: 10.1016/j.biomaterials.2007.12.037.

[51] V. Kattumuri *et al.*, “Gum Arabic as a Phytochemical Construct for the Stabilization of Gold Nanoparticles: In Vivo Pharmacokinetics and X-ray-Contrast-Imaging Studies,” *Small*, vol. 3, no. 2, pp. 333–341, 2007, doi: 10.1002/smll.200600427.

[52] X.-D. Zhang *et al.*, “Size-dependent in vivo toxicity of PEG-coated gold nanoparticles,” *IJN*, vol. 6, pp. 2071–2081, Sep. 2011, doi: 10.2147/IJN.S21657.

[53] S. T. Kim, K. Saha, C. Kim, and V. M. Rotello, “The Role of Surface Functionality in Determining Nanoparticle Cytotoxicity,” *Acc. Chem. Res.*, vol. 46, no. 3, pp. 681–691, Mar. 2013, doi: 10.1021/ar3000647.

[54] R. Terracciano *et al.*, “Effects of Surface Protein Adsorption on the Distribution and Retention of Intratumorally Administered Gold Nanoparticles,” *Pharmaceutics*, vol. 13, no. 2, Art. no. 2, Feb. 2021, doi: 10.3390/pharmaceutics13020216.

[55] R. Terracciano, Y. Carcamo-Bahena, E. B. Butler, D. Demarchi, A. Grattoni, and C. S. Filgueira, “Hyaluronate-Thiol Passivation Enhances Gold Nanoparticle Peritumoral Distribution When Administered Intratumorally in Lung Cancer,” *Biomedicines*, vol. 9, no. 11, Art. no. 11, Nov. 2021, doi: 10.3390/biomedicines9111561.

[56] R. Terracciano, A. Zhang, M. L. Simeral, D. Demarchi, J. H. Hafner, and C. S. Filgueira, “Improvements in Gold Nanorod Biocompatibility with Sodium Dodecyl Sulfate Stabilization,” *J Nanotheranostics*, vol. 2, no. 3, Art. no. 3, Sep. 2021, doi: 10.3390/jnt2030010.

[57] N. Mathuria *et al.*, “Near-infrared sensitive nanoparticle-mediated photothermal ablation of ventricular myocardium,” *Heart Rhythm*, pp. S1547-5271(22)01962–2, May 2022, doi: 10.1016/j.hrthm.2022.05.006.

[58] C. J. Miller *et al.*, “Predictors of Distant Failure After Stereotactic Body Radiation Therapy for Stages I to IIA Non–Small-Cell Lung Cancer,” *Clinical Lung Cancer*, vol. 20, no. 1, pp. 37–42, Jan. 2019, doi: 10.1016/j.cllc.2018.09.002.

[59] S. Her, D. A. Jaffray, and C. Allen, “Gold nanoparticles for applications in cancer radiotherapy: Mechanisms and recent advancements,” *Advanced Drug Delivery Reviews*, vol. 109, pp. 84–101, Jan. 2017, doi: 10.1016/j.addr.2015.12.012.

[60] Y. Chen *et al.*, “Gold nanoparticles coated with polysarcosine brushes to enhance their colloidal stability and circulation time in vivo,” *Journal of Colloid and Interface Science*, vol. 483, pp. 201–210, Dec. 2016, doi: 10.1016/j.jcis.2016.08.038.

[61] S. Rosa, C. Connolly, G. Schettino, K. T. Butterworth, and K. M. Prise, “Biological mechanisms of gold nanoparticle radiosensitization,” *Cancer Nano*, vol. 8, no. 1, p. 2, Dec. 2017, doi: 10.1186/s12645-017-0026-0.

[62] D. Kim *et al.*, “Label-free high-resolution 3-D imaging of gold nanoparticles inside live cells using optical diffraction tomography,” *Methods*, vol. 136, pp. 160–167, Mar. 2018, doi: 10.1016/j.ymeth.2017.07.008.

[63] R. Meir *et al.*, “Nanomedicine for Cancer Immunotherapy: Tracking Cancer-Specific T-Cells in Vivo with Gold Nanoparticles and CT Imaging,” *ACS Nano*, vol. 9, no. 6, pp. 6363–6372, Jun. 2015, doi: 10.1021/acsnano.5b01939.

[64] M. M. Mahan and A. L. Doiron, “Gold Nanoparticles as X-Ray, CT, and Multimodal Imaging Contrast Agents: Formulation, Targeting, and Methodology,” *Journal of Nanomaterials*, 2018. https://www.hindawi.com/journals/jnm/2018/5837276/ (accessed Mar. 23, 2020).

[65] R. Cheheltani *et al.*, “Tunable, biodegradable gold nanoparticles as contrast agents for computed tomography and photoacoustic imaging,” *Biomaterials*, vol. 102, pp. 87–97, Sep. 2016, doi: 10.1016/j.biomaterials.2016.06.015.

[66] M. F. Ghaziyani *et al.*, “Anti-CD24 bio Modified PEGylated Gold Nanoparticles as Targeted Computed Tomography Contrast Agent,” *Adv Pharm Bull*, vol. 8, no. 4, pp. 599–607, Nov. 2018, doi: 10.15171/apb.2018.068.

[67] J. Turkevich, P. C. Stevenson, and J. Hillier, “The Formation of Colloidal Gold,” *The Journal of Physical Chemistry*, vol. 57, no. 7, pp. 670–673, Jul. 1953, doi: 10.1021/j150508a015.

[68] B. Sumer and J. Gao, “Theranostic nanomedicine for cancer,” *Nanomedicine*, vol. 3, no. 2, pp. 137–140, Mar. 2008, doi: 10.2217/17435889.3.2.137.

[69] C. Y. X. Chua, J. Ho, S. Demaria, M. Ferrari, and A. Grattoni, “Emerging Technologies for Local Cancer Treatment,” *Adv. Therap.*, vol. 3, no. 9, p. 2000027, Sep. 2020, doi: 10.1002/adtp.202000027.

[70] D. Singh, F. Dilnawaz, and S. K. Sahoo, “Challenges of moving theranostic nanomedicine into the clinic,” *Nanomedicine*, vol. 15, no. 2, pp. 111–114, Jan. 2020, doi: 10.2217/nnm-2019-0401.

[71] C. Auría-Soro *et al.*, “Interactions of Nanoparticles and Biosystems: Microenvironment of Nanoparticles and Biomolecules in Nanomedicine,” *Nanomaterials (Basel)*, vol. 9, no. 10, Sep. 2019, doi: 10.3390/nano9101365.

[72] C. Vasti, D. A. Bedoya, R. Rojas, and C. E. Giacomelli, “Effect of the protein corona on the colloidal stability and reactivity of LDH-based nanocarriers,” *J. Mater. Chem. B*, vol. 4, no. 11, pp. 2008–2016, Mar. 2016, doi: 10.1039/C5TB02698A.

[73] J. S. Gebauer *et al.*, “Impact of the Nanoparticle–Protein Corona on Colloidal Stability and Protein Structure,” *Langmuir*, vol. 28, no. 25, pp. 9673–9679, Jun. 2012, doi: 10.1021/la301104a.

[74] K. Strojan, A. Leonardi, V. B. Bregar, I. Križaj, J. Svete, and M. Pavlin, “Dispersion of Nanoparticles in Different Media Importantly Determines the Composition of Their Protein Corona,” *PLOS ONE*, vol. 12, no. 1, p. e0169552, gen 2017, doi: 10.1371/journal.pone.0169552.

[75] L. Böhmert, L. Voß, V. Stock, A. Braeuning, A. Lampen, and H. Sieg, “Isolation methods for particle protein corona complexes from protein-rich matrices,” *Nanoscale Adv.*, vol. 2, no. 2, pp. 563–582, Feb. 2020, doi: 10.1039/C9NA00537D.

[76] R. Barbir *et al.*, “Protein Corona Modulates Distribution and Toxicological Effects of Silver Nanoparticles In Vivo,” *Particle & Particle Systems*

Characterization, vol. 36, no. 8, p. 1900174, 2019, doi: https://doi.org/10.1002/ppsc.201900174.

[77] N. Bertrand *et al.*, "Mechanistic understanding of in vivo protein corona formation on polymeric nanoparticles and impact on pharmacokinetics," *Nature Communications*, vol. 8, no. 1, p. 777, Oct. 2017, doi: 10.1038/s41467-017-00600-w.

[78] K. Giri, I. Kuschnerus, J. Ruan, and A. E. Garcia-Bennett, "Influence of a Protein Corona on the Oral Pharmacokinetics of Testosterone Released from Mesoporous Silica," *Advanced Therapeutics*, vol. 3, no. 5, p. 1900110, 2020, doi: https://doi.org/10.1002/adtp.201900110.

[79] S. Tavakoli *et al.*, "Diffusion and Protein Corona Formation of Lipid-Based Nanoparticles in the Vitreous Humor: Profiling and Pharmacokinetic Considerations," *Mol Pharm*, Jul. 2020, doi: 10.1021/acs.molpharmaceut.0c00411.

[80] C. Corbo, R. Molinaro, A. Parodi, N. E. Toledano Furman, F. Salvatore, and E. Tasciotti, "The impact of nanoparticle protein corona on cytotoxicity, immunotoxicity and target drug delivery," *Nanomedicine (Lond)*, vol. 11, no. 1, pp. 81–100, Jan. 2016, doi: 10.2217/nnm.15.188.

[81] H. Mohammad-Beigi *et al.*, "Mapping and identification of soft corona proteins at nanoparticles and their impact on cellular association," *Nature Communications*, vol. 11, no. 1, p. 4535, Sep. 2020, doi: 10.1038/s41467-020-18237-7.

[82] D. Westmeier, C. Chen, R. H. Stauber, and D. Docter, "The bio-corona and its impact on nanomaterial toxicity," *European Journal of Nanomedicine*, vol. 7, no. 3, pp. 153–168, Jun. 2015, doi: 10.1515/ejnm-2015-0018.

[83] X. Huang and M. A. El-Sayed, "Gold nanoparticles: Optical properties and implementations in cancer diagnosis and photothermal therapy," *Journal of Advanced Research*, vol. 1, no. 1, pp. 13–28, Jan. 2010, doi: 10.1016/j.jare.2010.02.002.

[84] X. Huang, P. K. Jain, I. H. El-Sayed, and M. A. El-Sayed, "Gold nanoparticles: interesting optical properties and recent applications in cancer diagnostics and therapy," *Nanomedicine*, vol. 2, no. 5, pp. 681–693, Oct. 2007, doi: 10.2217/17435889.2.5.681.

[85] M. O. Stetsenko, S. P. Rudenko, L. S. Maksimenko, B. K. Serdega, O. Pluchery, and S. V. Snegir, "Optical Properties of Gold Nanoparticle Assemblies on a Glass Surface," *Nanoscale Research Letters*, vol. 12, no. 1, p. 348, May 2017, doi: 10.1186/s11671-017-2107-8.

[86] R. Shukla, V. Bansal, M. Chaudhary, A. Basu, R. R. Bhonde, and M. Sastry, "Biocompatibility of gold nanoparticles and their endocytotic fate inside the

cellular compartment: a microscopic overview," *Langmuir*, vol. 21, no. 23, pp. 10644–10654, Nov. 2005, doi: 10.1021/la0513712.

[87] X. Li, L. Wang, Y. Fan, Q. Feng, and F. Cui, "Biocompatibility and Toxicity of Nanoparticles and Nanotubes," *Journal of Nanomaterials*, Jun. 26, 2012. https://www.hindawi.com/journals/jnm/2012/548389/ (accessed Dec. 05, 2020).

[88] S. Kumar, I. Jha, N. K. Mogha, and P. Venkatesu, "Biocompatibility of surface-modified gold nanoparticles towards red blood cells and haemoglobin," *Applied Surface Science*, vol. 512, p. 145573, May 2020, doi: 10.1016/j.apsusc.2020.145573.

[89] J. Guo, K. Rahme, Y. He, L.-L. Li, J. D. Holmes, and C. M. O'Driscoll, "Gold nanoparticles enlighten the future of cancer theranostics," *Int J Nanomedicine*, vol. 12, pp. 6131–6152, 2017, doi: 10.2147/IJN.S140772.

[90] L. J. E. Anderson, C. M. Payne, Y.-R. Zhen, P. Nordlander, and J. H. Hafner, "A tunable plasmon resonance in gold nanobelts," *Nano Lett*, vol. 11, no. 11, pp. 5034–5037, Nov. 2011, doi: 10.1021/nl203085t.

[91] S. Lal, J. H. Hafner, N. J. Halas, S. Link, and P. Nordlander, "Noble metal nanowires: from plasmon waveguides to passive and active devices," *Acc Chem Res*, vol. 45, no. 11, pp. 1887–1895, Nov. 2012, doi: 10.1021/ar300133j.

[92] C. L. Nehl, H. Liao, and J. H. Hafner, "Optical properties of star-shaped gold nanoparticles," *Nano Lett*, vol. 6, no. 4, pp. 683–688, Apr. 2006, doi: 10.1021/nl052409y.

[93] B. E. Brinson, J. B. Lassiter, C. S. Levin, R. Bardhan, N. Mirin, and N. J. Halas, "Nanoshells made easy: improving Au layer growth on nanoparticle surfaces," *Langmuir*, vol. 24, no. 24, pp. 14166–14171, Dec. 2008, doi: 10.1021/la802049p.

[94] A. T. Kelly, C. S. Filgueira, D. E. Schipper, N. J. Halas, and K. H. Whitmire, "Gold coated iron phosphide core–shell structures," *RSC Adv.*, vol. 7, no. 42, pp. 25848–25854, May 2017, doi: 10.1039/C7RA01195D.

[95] C. S. Levin *et al.*, "Magnetic-plasmonic core-shell nanoparticles," *ACS Nano*, vol. 3, no. 6, pp. 1379–1388, Jun. 2009, doi: 10.1021/nn900118a.

[96] M.-R. Choi *et al.*, "A cellular Trojan Horse for delivery of therapeutic nanoparticles into tumors," *Nano Lett*, vol. 7, no. 12, pp. 3759–3765, Dec. 2007, doi: 10.1021/nl072209h.

[97] A. R. Rastinehad *et al.*, "Gold nanoshell-localized photothermal ablation of prostate tumors in a clinical pilot device study," *Proc Natl Acad Sci U S A*, vol. 116, no. 37, pp. 18590–18596, 10 2019, doi: 10.1073/pnas.1906929116.

[98] M. Bros *et al.*, “The Protein Corona as a Confounding Variable of Nanoparticle-Mediated Targeted Vaccine Delivery,” *Front. Immunol.*, vol. 9, 2018, doi: 10.3389/fimmu.2018.01760.

[99] E. Brun and C. Sicard – Roselli, “Could nanoparticle corona characterization help for biological consequence prediction?,” *Cancer Nanotechnol*, vol. 5, no. 1, 2014, doi: 10.1186/s12645-014-0007-5.

[100] Y. Ma, J. Hong, and Y. Ding, “Biological Behavior Regulation of Gold Nanoparticles via the Protein Corona,” *Adv Healthc Mater*, vol. 9, no. 6, p. e1901448, 2020, doi: 10.1002/adhm.201901448.

[101] D. Chen, S. Ganesh, W. Wang, and M. Amiji, “Protein Corona-Enabled Systemic Delivery and Targeting of Nanoparticles,” *AAPS J*, vol. 22, no. 4, p. 83, Jun. 2020, doi: 10.1208/s12248-020-00464-x.

[102] J. Piella, N. G. Bastús, and V. Puntes, “Size-Dependent Protein–Nanoparticle Interactions in Citrate-Stabilized Gold Nanoparticles: The Emergence of the Protein Corona,” *Bioconjugate Chem.*, vol. 28, no. 1, pp. 88–97, Jan. 2017, doi: 10.1021/acs.bioconjchem.6b00575.

[103] B. Li and L. A. Lane, “Probing the biological obstacles of nanomedicine with gold nanoparticles,” *Wiley Interdiscip Rev Nanomed Nanobiotechnol*, vol. 11, no. 3, 2019, doi: 10.1002/wnan.1542.

[104] J. Mosquera *et al.*, “Reversible Control of Protein Corona Formation on Gold Nanoparticles Using Host–Guest Interactions,” *ACS Nano*, vol. 14, no. 5, pp. 5382–5391, May 2020, doi: 10.1021/acsnano.9b08752.

[105] C. K. Elechalawar, Md. N. Hossen, L. McNally, R. Bhattacharya, and P. Mukherjee, “Analysing the nanoparticle-protein corona for potential molecular target identification,” *J Control Release*, vol. 322, pp. 122–136, Jun. 2020, doi: 10.1016/j.jconrel.2020.03.008.

[106] S. J. Park, “Protein–Nanoparticle Interaction: Corona Formation and Conformational Changes in Proteins on Nanoparticles,” *Int J Nanomedicine*, vol. 15, pp. 5783–5802, Aug. 2020, doi: 10.2147/IJN.S254808.

[107] D. Nierenberg, A. R. Khaled, and O. Flores, “Formation of a protein corona influences the biological identity of nanomaterials,” *Rep Pract Oncol Radiother*, vol. 23, no. 4, pp. 300–308, 2018, doi: 10.1016/j.rpor.2018.05.005.

[108] Z. Varga *et al.*, “Size Measurement of Extracellular Vesicles and Synthetic Liposomes: The Impact of the Hydration Shell and the Protein Corona,” *Colloids and Surfaces B: Biointerfaces*, vol. 192, p. 111053, Aug. 2020, doi: 10.1016/j.colsurfb.2020.111053.

[109] L. Digiacomo *et al.*, “The biomolecular corona of gold nanoparticles in a controlled microfluidic environment,” *Lab Chip*, vol. 19, no. 15, pp. 2557–2567, Jul. 2019, doi: 10.1039/C9LC00341J.

[110] X. Cheng *et al.*, "Protein Corona Influences Cellular Uptake of Gold Nanoparticles by Phagocytic and Nonphagocytic Cells in a Size-Dependent Manner," *ACS Appl. Mater. Interfaces*, vol. 7, no. 37, pp. 20568–20575, Sep. 2015, doi: 10.1021/acsami.5b04290.

[111] E. Blanco, H. Shen, and M. Ferrari, "Principles of nanoparticle design for overcoming biological barriers to drug delivery," *Nat Biotechnol*, vol. 33, no. 9, pp. 941–951, Sep. 2015, doi: 10.1038/nbt.3330.

[112] P. Chandran, J. E. Riviere, and N. A. Monteiro-Riviere, "Surface chemistry of gold nanoparticles determines the biocorona composition impacting cellular uptake, toxicity and gene expression profiles in human endothelial cells," *Nanotoxicology*, vol. 11, no. 4, pp. 507–519, Apr. 2017, doi: 10.1080/17435390.2017.1314036.

[113] M. Han *et al.*, "Protein Corona and Immune Responses of Borophene: A Comparison of Nanosheet–Plasma Interface with Graphene and Phosphorene," *ACS Appl. Bio Mater.*, vol. 3, no. 7, pp. 4220–4229, Jul. 2020, doi: 10.1021/acsabm.0c00306.

[114] M. Neagu *et al.*, "Protein bio-corona: critical issue in immune nanotoxicology," *Arch Toxicol*, vol. 91, no. 3, pp. 1031–1048, 2017, doi: 10.1007/s00204-016-1797-5.

[115] J. Y. Oh *et al.*, "Cloaking nanoparticles with protein corona shield for targeted drug delivery," *Nature Communications*, vol. 9, no. 1, p. 4548, Oct. 2018, doi: 10.1038/s41467-018-06979-4.

[116] B. Wang, X. He, Z. Zhang, Y. Zhao, and W. Feng, "Metabolism of Nanomaterials in Vivo: Blood Circulation and Organ Clearance," *Acc. Chem. Res.*, vol. 46, no. 3, pp. 761–769, Mar. 2013, doi: 10.1021/ar2003336.

[117] P. M. Gullino, S. H. Clark, and F. H. Grantham, "The Interstitial Fluid of Solid Tumors," *Cancer Res*, vol. 24, no. 5, pp. 780–797, Jun. 1964.

[118] Z. Chen, C. M. Fillmore, P. S. Hammerman, C. F. Kim, and K.-K. Wong, "Non-small-cell lung cancers: a heterogeneous set of diseases," *Nat Rev Cancer*, vol. 14, no. 8, pp. 535–546, Aug. 2014, doi: 10.1038/nrc3775.

[119] A. L. van Lamsweerde, N. Henry, and G. Vaes, "Metastatic heterogeneity of cells from Lewis lung carcinoma," *Cancer Res*, vol. 43, no. 11, pp. 5314–5320, Nov. 1983.

[120] I. Dagogo-Jack and A. T. Shaw, "Tumour heterogeneity and resistance to cancer therapies," *Nat Rev Clin Oncol*, vol. 15, no. 2, pp. 81–94, Feb. 2018, doi: 10.1038/nrclinonc.2017.166.

[121] A. Pandey *et al.*, "Gold Nanoparticles Radio-Sensitize and Reduce Cell Survival in Lewis Lung Carcinoma," *Nanomaterials*, vol. 10, no. 9, Aug. 2020, doi: 10.3390/nano10091717.

[122] R. Terracciano *et al.*, "Intratumoral Gold Nanoparticle-Enhanced CT Imaging: An in Vivo Investigation of Biodistribution and Retention," *2020 IEEE 20th International Conference on Nanotechnology (IEEE-NANO)*, vol. Montreal, QC, Canada, 2020, pp. 349–353, 2020, doi: 10.1109/NANO47656.2020.9183611.

[123] H. J. Hughes, S. M. E. Demers, A. Zhang, and J. H. Hafner, "The orientation of a membrane probe from structural analysis by enhanced Raman scattering," *Biochimica et Biophysica Acta (BBA) - Biomembranes*, vol. 1862, no. 2, p. 183109, Feb. 2020, doi: 10.1016/j.bbamem.2019.183109.

[124] A. Fedorov *et al.*, "3D Slicer as an Image Computing Platform for the Quantitative Imaging Network," *Magn Reson Imaging*, vol. 30, no. 9, pp. 1323–1341, Nov. 2012, doi: 10.1016/j.mri.2012.05.001.

[125] D. V. Sotnikov, A. N. Berlina, V. S. Ivanov, A. V. Zherdev, and B. B. Dzantiev, "Adsorption of proteins on gold nanoparticles: One or more layers?," *Colloids and Surfaces B: Biointerfaces*, vol. 173, pp. 557–563, Jan. 2019, doi: 10.1016/j.colsurfb.2018.10.025.

[126] N. Jommanee, C. Chanthad, and K. Manokruang, "Preparation of injectable hydrogels from temperature and pH responsive grafted chitosan with tuned gelation temperature suitable for tumor acidic environment," *Carbohydrate Polymers*, vol. 198, pp. 486–494, Oct. 2018, doi: 10.1016/j.carbpol.2018.06.099.

[127] S. Dominguez-Medina, S. McDonough, P. Swanglap, C. F. Landes, and S. Link, "In Situ Measurement of Bovine Serum Albumin Interaction with Gold Nanospheres," *Langmuir*, vol. 28, no. 24, pp. 9131–9139, Jun. 2012, doi: 10.1021/la3005213.

[128] C. Röcker, M. Pötzl, F. Zhang, W. J. Parak, and G. U. Nienhaus, "A quantitative fluorescence study of protein monolayer formation on colloidal nanoparticles," *Nature Nanotech*, vol. 4, no. 9, pp. 577–580, Sep. 2009, doi: 10.1038/nnano.2009.195.

[129] E. Campeau *et al.*, "A Versatile Viral System for Expression and Depletion of Proteins in Mammalian Cells," *PLoS ONE*, vol. 4, no. 8, p. e6529, Aug. 2009, doi: 10.1371/journal.pone.0006529.

[130] G. P. Szekeres and J. Kneipp, "SERS Probing of Proteins in Gold Nanoparticle Agglomerates," *Front. Chem.*, vol. 7, 2019, doi: 10.3389/fchem.2019.00030.

[131] H. Tyagi, A. Kushwaha, A. Kumar, and M. Aslam, "A Facile pH Controlled Citrate-Based Reduction Method for Gold Nanoparticle Synthesis at Room Temperature," *Nanoscale Res Lett*, vol. 11, no. 1, p. 362, Aug. 2016, doi: 10.1186/s11671-016-1576-5.

[132] S. Sutoo, T. Maeda, A. Suzuki, and Y. Kato, "Adaptation to chronic acidic extracellular pH elicits a sustained increase in lung cancer cell invasion and metastasis," *Clin Exp Metastasis*, vol. 37, no. 1, pp. 133–144, Feb. 2020, doi: 10.1007/s10585-019-09990-1.

[133] N. Oh and J.-H. Park, "Endocytosis and exocytosis of nanoparticles in mammalian cells," *Int J Nanomedicine*, vol. 9, no. Suppl 1, pp. 51–63, May 2014, doi: 10.2147/IJN.S26592.

[134] L. Mocan *et al.*, "Selective ex vivo photothermal nano-therapy of solid liver tumors mediated by albumin conjugated gold nanoparticles," *Biomaterials*, vol. 119, pp. 33–42, Mar. 2017, doi: 10.1016/j.biomaterials.2016.12.009.

[135] F. Charbgoo *et al.*, "Gold nanoparticle should understand protein corona for being a clinical nanomaterial," *Journal of Controlled Release*, vol. 272, pp. 39–53, Feb. 2018, doi: 10.1016/j.jconrel.2018.01.002.

[136] R. Rampado, S. Crotti, P. Caliceti, S. Pucciarelli, and M. Agostini, "Recent Advances in Understanding the Protein Corona of Nanoparticles and in the Formulation of 'Stealthy' Nanomaterials," *Front. Bioeng. Biotechnol.*, vol. 8, 2020, doi: 10.3389/fbioe.2020.00166.

[137] D. I. Viswanath, H.-C. Liu, D. P. Huston, C. Y. X. Chua, and A. Grattoni, "Emerging biomaterial-based strategies for personalized therapeutic in situ cancer vaccines," *Biomaterials*, vol. 280, p. 121297, Jan. 2022, doi: 10.1016/j.biomaterials.2021.121297.

[138] H.-C. Liu *et al.*, "Potentiating Antitumor Efficacy Through Radiation and Sustained Intratumoral Delivery of Anti-CD40 and Anti-PDL1," *Int. J. Radiat. Oncol. Biol. Phys.*, vol. 110, no. 2, pp. 492–506, Jun. 2021, doi: 10.1016/j.ijrobp.2020.07.2326.

[139] C. Y. X. Chua *et al.*, "Nanofluidic drug-eluting seed for sustained intratumoral immunotherapy in triple negative breast cancer," *J Control Release*, vol. 285, pp. 23–34, Sep. 2018, doi: 10.1016/j.jconrel.2018.06.035.

[140] L. Li *et al.*, "Improved intratumoral nanoparticle extravasation and penetration by mild hyperthermia," *J. Control. Release*, vol. 167, no. 2, pp. 130–137, Apr. 2013, doi: 10.1016/j.jconrel.2013.01.026.

[141] W. Li *et al.*, "Gold Nanoparticle–Mediated Targeted Delivery of Recombinant Human Endostatin Normalizes Tumour Vasculature and Improves Cancer Therapy," *Sci. Rep.*, vol. 6, no. 1, p. 30619, Jul. 2016, doi: 10.1038/srep30619.

[142] Y. Chen *et al.*, "Therapeutic Remodeling of the Tumor Microenvironment Enhances Nanoparticle Delivery," *Adv. Sci.*, vol. 6, no. 5, p. 1802070, 2019, doi: 10.1002/advs.201802070.

[143] W. Jiang, Y. Huang, Y. An, and B. Y. S. Kim, "Remodeling Tumor Vasculature to Enhance Delivery of Intermediate-Sized Nanoparticles," *ACS Nano*, vol. 9, no. 9, pp. 8689–8696, Sep. 2015, doi: 10.1021/acsnano.5b02028.

[144] T. Lammers, F. Kiessling, W. E. Hennink, and G. Storm, "Drug targeting to tumors: Principles, pitfalls and (pre-) clinical progress," *J. Control. Release*, vol. 161, no. 2, pp. 175–187, Jul. 2012, doi: 10.1016/j.jconrel.2011.09.063.

[145] A. J. Wagstaff *et al.*, "Cisplatin drug delivery using gold-coated iron oxide nanoparticles for enhanced tumour targeting with external magnetic fields," *Inorganica Chim. Acta*, vol. 393, pp. 328–333, Dec. 2012, doi: 10.1016/j.ica.2012.05.012.

[146] C. S. Levin *et al.*, "Magnetic−Plasmonic Core−Shell Nanoparticles," *ACS Nano*, vol. 3, no. 6, pp. 1379–1388, Jun. 2009, doi: 10.1021/nn900118a.

[147] S. Snipstad *et al.*, "Ultrasound Improves the Delivery and Therapeutic Effect of Nanoparticle-Stabilized Microbubbles in Breast Cancer Xenografts," *Ultrasound. Med. Biol.*, vol. 43, no. 11, pp. 2651–2669, Nov. 2017, doi: 10.1016/j.ultrasmedbio.2017.06.029.

[148] M.-R. Choi *et al.*, "A cellular Trojan Horse for delivery of therapeutic nanoparticles into tumors," *Nano Lett*, vol. 7, no. 12, pp. 3759–3765, Dec. 2007, doi: 10.1021/nl072209h.

[149] S. H. Crayton and A. Tsourkas, "pH-Titratable Superparamagnetic Iron Oxide for Improved Nanoparticle Accumulation in Acidic Tumor Microenvironments," *ACS Nano*, vol. 5, no. 12, pp. 9592–9601, Dec. 2011, doi: 10.1021/nn202863x.

[150] S. W. Bishnoi *et al.*, "All-Optical Nanoscale pH Meter," *Nano Lett.*, vol. 6, no. 8, pp. 1687–1692, Aug. 2006, doi: 10.1021/nl060865w.

[151] J. F. Liu, B. Jang, D. Issadore, and A. Tsourkas, "Use of Magnetic Fields and Nanoparticles to Trigger Drug Release and Improve Tumor Targeting," *Wiley Interdiscip. Rev. Nanomed. Nanobiotechnol.*, vol. 11, no. 6, p. e1571, Nov. 2019, doi: 10.1002/wnan.1571.

[152] C. G. England, J. S. Huang, K. T. James, G. Zhang, A. M. Gobin, and H. B. Frieboes, "Detection of Phosphatidylcholine-Coated Gold Nanoparticles in Orthotopic Pancreatic Adenocarcinoma using Hyperspectral Imaging," *PLoS One*, vol. 10, no. 6, p. e0129172, Jun. 2015, doi: 10.1371/journal.pone.0129172.

[153] S. Huo *et al.*, "Superior penetration and retention behavior of 50 nm gold nanoparticles in tumors," *Cancer Res.*, vol. 73, no. 1, pp. 319–330, Jan. 2013, doi: 10.1158/0008-5472.CAN-12-2071.

[154] G. Garrastazu Pereira, A. J. Lawson, F. Buttini, and F. Sonvico, "Loco-regional administration of nanomedicines for the treatment of lung cancer,"

Drug Delivery, vol. 23, no. 8, pp. 2881–2896, Oct. 2016, doi: 10.3109/10717544.2015.1114047.

[155] C. Y. X. Chua, J. Ho, S. Demaria, M. Ferrari, and A. Grattoni, "Emerging Technologies for Local Cancer Treatment," *Adv. Ther.*, vol. 3, no. 9, p. 2000027, 2020, doi: 10.1002/adtp.202000027.

[156] A. Marabelle *et al.*, "Starting the fight in the tumor: expert recommendations for the development of human intratumoral immunotherapy (HIT-IT)," *Ann. Oncol.*, vol. 29, no. 11, pp. 2163–2174, Nov. 2018, doi: 10.1093/annonc/mdy423.

[157] I. Melero, E. Castanon, M. Alvarez, S. Champiat, and A. Marabelle, "Intratumoural administration and tumour tissue targeting of cancer immunotherapies," *Nat. Rev. Clin. Oncol.*, vol. 18, no. 9, Art. no. 9, Sep. 2021, doi: 10.1038/s41571-021-00507-y.

[158] K. Yasuda, T. Nirei, N. H. Tsuno, H. Nagawa, and J. Kitayama, "Intratumoral injection of interleukin-2 augments the local and abscopal effects of radiotherapy in murine rectal cancer," *Cancer Sci.*, vol. 102, no. 7, pp. 1257–1263, Jul. 2011, doi: 10.1111/j.1349-7006.2011.01940.x.

[159] A. Mukhopadhyay *et al.*, "Characterization of abscopal effects of intratumoral electroporation-mediated IL-12 gene therapy," *Gene Ther.*, vol. 26, no. 1, Art. no. 1, Feb. 2019, doi: 10.1038/s41434-018-0044-5.

[160] P. Dogra *et al.*, "Establishing the effects of mesoporous silica nanoparticle properties on in vivo disposition using imaging-based pharmacokinetics," *Nat. Commun.*, vol. 9, no. 1, p. 4551, Oct. 2018, doi: 10.1038/s41467-018-06730-z.

[161] S. Goel *et al.*, "Size-Optimized Ultrasmall Porous Silica Nanoparticles Depict Vasculature-Based Differential Targeting in Triple Negative Breast Cancer," *Small*, vol. 15, no. 46, p. 1903747, 2019, doi: 10.1002/smll.201903747.

[162] S. Goel *et al.*, "Sequential deconstruction of composite drug transport in metastatic breast cancer," *Sci. Adv.*, vol. 6, no. 26, p. eaba4498, doi: 10.1126/sciadv.aba4498.

[163] S. Wilhelm *et al.*, "Analysis of nanoparticle delivery to tumours," *Nat. Rev. Mater.*, vol. 1, no. 5, pp. 1–12, Apr. 2016, doi: 10.1038/natrevmats.2016.14.

[164] R. Terracciano *et al.*, "Intratumoral Gold Nanoparticle-Enhanced CT Imaging: An in Vivo Investigation of Biodistribution and Retention," in *2020 IEEE 20th International Conference on Nanotechnology (IEEE-NANO)*, Jul. 2020, pp. 349–353. doi: 10.1109/NANO47656.2020.9183611.

[165] P. Dogra *et al.*, "Mathematical modeling in cancer nanomedicine: a review," *Biomed. Microdevices*, vol. 21, no. 2, p. 40, Apr. 2019, doi: 10.1007/s10544-019-0380-2.

[166] P. Dogra *et al.*, “Image-guided mathematical modeling for pharmacological evaluation of nanomaterials and monoclonal antibodies,” *Wiley Interdiscip. Rev. Nanomed. Nanobiotechnol. WIRES NANOMED NANOBI*, vol. 12, no. 5, p. e1628, 2020, doi: 10.1002/wnan.1628.

[167] P. Dogra *et al.*, “A mathematical model to predict nanomedicine pharmacokinetics and tumor delivery,” *Comput. Struct. Biotechnol. J.*, vol. 18, pp. 518–531, Feb. 2020, doi: 10.1016/j.csbj.2020.02.014.

[168] N. Mahesh, N. Singh, and P. Talukdar, “A mathematical model for understanding nanoparticle biodistribution after intratumoral injection in cancer tumors,” *J. Drug Deliv. Sci. Technol.*, vol. 68, p. 103048, Feb. 2022, doi: 10.1016/j.jddst.2021.103048.

[169] A. P. Klapproth, M. Shevtsov, S. Stangl, W. B. Li, and G. Multhoff, “A New Pharmacokinetic Model Describing the Biodistribution of Intravenously and Intratumorally Administered Superparamagnetic Iron Oxide Nanoparticles (SPIONs) in a GL261 Xenograft Glioblastoma Model,” *Int J Nanomedicine*, vol. 15, pp. 4677–4689, 2020, doi: 10.2147/IJN.S254745.

[170] G. Brachi *et al.*, “Intratumoral injection of hydrogel-embedded nanoparticles enhances retention in glioblastoma,” *Nanoscale*, vol. 12, no. 46, pp. 23838–23850, Dec. 2020, doi: 10.1039/D0NR05053A.

[171] J. Lu *et al.*, “A non-sacrificial method for the quantification of poly(ethylene glycol) grafting density on gold nanoparticles for applications in nanomedicine,” *Chem Sci*, vol. 10, no. 7, pp. 2067–2074, Feb. 2019, doi: 10.1039/c8sc02847h.

[172] R. Terracciano, A. Zhang, M. L. Simeral, D. Demarchi, J. H. Hafner, and C. S. Filgueira, “Improvements in Gold Nanorod Biocompatibility with Sodium Dodecyl Sulfate Stabilization,” *J. Nanotheranostics*, vol. 2, no. 3, Art. no. 3, Sep. 2021, doi: 10.3390/jnt2030010.

[173] V. Cristini, E. Koay, and Z. Wang, “An Introduction to Physical Oncology: How Mechanistic Mathematical Modeling Can Improve Cancer Therapy Outcomes,” *CRC Press*, vol. 38, no. 1, pp. 585–586, Jan. 2018.

[174] J. Turkevich, P. C. Stevenson, and J. Hillier, “A study of the nucleation and growth processes in the synthesis of colloidal gold,” *Discuss. Faraday Soc.*, vol. 11, no. 0, pp. 55–75, Jan. 1951, doi: 10.1039/DF9511100055.

[175] C. S. Levin, J. Kundu, B. G. Janesko, G. E. Scuseria, R. M. Raphael, and N. J. Halas, “Interactions of Ibuprofen with Hybrid Lipid Bilayers Probed by Complementary Surface-Enhanced Vibrational Spectroscopies,” *J. Phys. Chem. B*, vol. 112, no. 45, pp. 14168–14175, Nov. 2008, doi: 10.1021/jp804374e.

[176] J. Kundu, C. S. Levin, and N. J. Halas, “Real-time monitoring of lipid transfer between vesicles and hybrid bilayers on Au nanoshells using surface

enhanced Raman scattering (SERS)," *Nanoscale*, vol. 1, no. 1, pp. 114–117, Sep. 2009, doi: 10.1039/B9NR00063A.

[177] C. S. Levin, S. W. Bishnoi, N. K. Grady, and N. J. Halas, "Determining the conformation of thiolated poly(ethylene glycol) on Au nanoshells by surface-enhanced Raman scattering spectroscopic assay," *Anal. Chem.*, vol. 78, no. 10, pp. 3277–3281, May 2006, doi: 10.1021/ac060041z.

[178] A. Goldstein, Y. Soroka, M. Frušić-Zlotkin, I. Popov, and R. Kohen, "High resolution SEM imaging of gold nanoparticles in cells and tissues," *J. Microsc.*, vol. 256, no. 3, pp. 237–247, Dec. 2014, doi: 10.1111/jmi.12179.

[179] Y. Dou *et al.*, "Size-Tuning Ionization To Optimize Gold Nanoparticles for Simultaneous Enhanced CT Imaging and Radiotherapy," *ACS Nano*, vol. 10, no. 2, pp. 2536–2548, Feb. 2016, doi: 10.1021/acsnano.5b07473.

[180] D. Kim, S. Park, J. H. Lee, Y. Y. Jeong, and S. Jon, "Antibiofouling Polymer-Coated Gold Nanoparticles as a Contrast Agent for in Vivo X-ray Computed Tomography Imaging," *J. Am. Chem. Soc.*, vol. 129, no. 24, pp. 7661–7665, Jun. 2007, doi: 10.1021/ja071471p.

[181] A.-K. Heinrich *et al.*, "Improved Tumor-Specific Drug Accumulation by Polymer Therapeutics with pH-Sensitive Drug Release Overcomes Chemotherapy Resistance," *Mol Cancer Ther*, vol. 15, no. 5, pp. 998–1007, May 2016, doi: 10.1158/1535-7163.MCT-15-0824.

[182] C. Y. X. Chua, J. Ho, S. Demaria, M. Ferrari, and A. Grattoni, "Emerging Technologies for Local Cancer Treatment," *Adv Ther*, vol. 3, no. 9, p. 2000027, 2020, doi: 10.1002/adtp.202000027.

[183] J. Ho *et al.*, "Localizing radioimmunotherapy via nanochannel device for sustained intratumoral drug delivery for solid tumor treatment.," *JCO*, vol. 37, no. 8_suppl, pp. 37–37, Mar. 2019, doi: 10.1200/JCO.2019.37.8_suppl.37.

[184] C. G. Park, C. A. Hartl, D. Schmid, E. M. Carmona, H.-J. Kim, and M. S. Goldberg, "Extended release of perioperative immunotherapy prevents tumor recurrence and eliminates metastases," *Sci. Transl. Med.*, vol. 10, no. 433, p. eaar1916, Mar. 2018, doi: 10.1126/scitranslmed.aar1916.

[185] N. Momin *et al.*, "Anchoring of intratumorally administered cytokines to collagen safely potentiates systemic cancer immunotherapy," *Sci Transl Med*, vol. 11, no. 498, p. eaaw2614, Jun. 2019, doi: 10.1126/scitranslmed.aaw2614.

[186] H.-C. Liu *et al.*, "Potentiating Antitumor Efficacy Through Radiation and Sustained Intratumoral Delivery of Anti-CD40 and Anti-PDL1," *Int J Radiat Oncol Biol Phys*, vol. 110, no. 2, pp. 492–506, Jun. 2021, doi: 10.1016/j.ijrobp.2020.07.2326.

[187] E. Blanco, H. Shen, and M. Ferrari, “Principles of nanoparticle design for overcoming biological barriers to drug delivery,” *Nat Biotechnol*, vol. 33, no. 9, pp. 941–951, Sep. 2015, doi: 10.1038/nbt.3330.

[188] L. C. Böckelmann and U. Schumacher, “Targeting tumor interstitial fluid pressure: will it yield novel successful therapies for solid tumors?,” *Expert Opin Ther Targets*, vol. 23, no. 12, pp. 1005–1014, Dec. 2019, doi: 10.1080/14728222.2019.1702974.

[189] H. A. Maulhardt *et al.*, “Local Injection of Submicron Particle Docetaxel is Associated with Tumor Eradication, Reduced Systemic Toxicity and an Immunologic Response in Uro-Oncologic Xenografts,” *Cancers (Basel)*, vol. 11, no. 4, p. 577, Apr. 2019, doi: 10.3390/cancers11040577.

[190] C. Bernauer, Y. K. S. Man, J. C. Chisholm, E. Y. Lepicard, S. P. Robinson, and J. M. Shipley, “Hypoxia and its therapeutic possibilities in paediatric cancers,” *Br J Cancer*, vol. 124, no. 3, pp. 539–551, Feb. 2021, doi: 10.1038/s41416-020-01107-w.

[191] S. Torok *et al.*, “Limited Tumor Tissue Drug Penetration Contributes to Primary Resistance against Angiogenesis Inhibitors,” *Theranostics*, vol. 7, no. 2, pp. 400–412, Jan. 2017, doi: 10.7150/thno.16767.

[192] Y. H. Bae and K. Park, “Targeted drug delivery to tumors: Myths, reality and possibility,” *J Control Release*, vol. 153, no. 3, pp. 198–205, Aug. 2011, doi: 10.1016/j.jconrel.2011.06.001.

[193] M. U. Farooq *et al.*, “Gold Nanoparticles-enabled Efficient Dual Delivery of Anticancer Therapeutics to HeLa Cells,” *Sci Rep*, vol. 8, no. 1, p. 2907, Dec. 2018, doi: 10.1038/s41598-018-21331-y.

[194] M. Yafout, A. Ousaid, Y. Khayati, and I. S. El Otmani, “Gold nanoparticles as a drug delivery system for standard chemotherapeutics: A new lead for targeted pharmacological cancer treatments,” *Sci Afr*, vol. 11, p. e00685, Mar. 2021, doi: 10.1016/j.sciaf.2020.e00685.

[195] S.-F. Lai *et al.*, “Gold nanoparticles as multimodality imaging agents for brain gliomas,” *J Nanobiotechnol*, vol. 13, no. 1, p. 85, Dec. 2015, doi: 10.1186/s12951-015-0140-2.

[196] V. P. Nguyen *et al.*, “Chain-like gold nanoparticle clusters for multimodal photoacoustic microscopy and optical coherence tomography enhanced molecular imaging,” *Nat Commun*, vol. 12, no. 1, p. 34, Jan. 2021, doi: 10.1038/s41467-020-20276-z.

[197] M. A. Kimm *et al.*, “Gold Nanoparticle Mediated Multi-Modal CT Imaging of Hsp70 Membrane-Positive Tumors,” *Cancers*, vol. 12, no. 5, Art. no. 5, May 2020, doi: 10.3390/cancers12051331.

[198] W. Su *et al.*, “Radionuclide-labeled gold nanoparticles for nuclei-targeting internal radio-immunity therapy,” *Mater. Horiz.*, vol. 7, no. 4, pp. 1115–1125, Apr. 2020, doi: 10.1039/C9MH01725A.

[199] I. H. Bartelink *et al.*, “Tumor Drug Penetration Measurements Could Be the Neglected Piece of the Personalized Cancer Treatment Puzzle,” *Clin Pharmacol Ther*, vol. 106, no. 1, pp. 148–163, 2019, doi: 10.1002/cpt.1211.

[200] A. Pandey *et al.*, “Gold Nanoparticles Radio-Sensitize and Reduce Cell Survival in Lewis Lung Carcinoma,” *Nanomaterials*, vol. 10, no. 9, Art. no. 9, Sep. 2020, doi: 10.3390/nano10091717.

[201] R. Terracciano *et al.*, “Effects of Surface Protein Adsorption on the Distribution and Retention of Intratumorally Administered Gold Nanoparticles,” *Pharmaceutics*, vol. 13, no. 2, Art. no. 2, Feb. 2021, doi: 10.3390/pharmaceutics13020216.

[202] R. Terracciano *et al.*, “Intratumoral Gold Nanoparticle-Enhanced CT Imaging: An in Vivo Investigation of Biodistribution and Retention,” in *2020 IEEE 20th International Conference on Nanotechnology (IEEE-NANO)*, Jul. 2020, pp. 349–353. doi: 10.1109/NANO47656.2020.9183611.

[203] J. Y. Lichtenberg, Y. Ling, and S. Kim, “Non-Specific Adsorption Reduction Methods in Biosensing,” *Sensors (Basel)*, vol. 19, no. 11, p. 2488, May 2019, doi: 10.3390/s19112488.

[204] J. Yoo, C. Park, G. Yi, D. Lee, and H. Koo, “Active Targeting Strategies Using Biological Ligands for Nanoparticle Drug Delivery Systems,” *Cancers (Basel)*, vol. 11, no. 5, p. 640, May 2019, doi: 10.3390/cancers11050640.

[205] C. S. Levin, S. W. Bishnoi, N. K. Grady, and N. J. Halas, “Determining the Conformation of Thiolated Poly(ethylene glycol) on Au Nanoshells by Surface-Enhanced Raman Scattering Spectroscopic Assay,” *Anal Chem*, vol. 78, no. 10, pp. 3277–3281, May 2006, doi: 10.1021/ac060041z.

[206] Y. Li *et al.*, “Impact of Anti-Biofouling Surface Coatings on the Properties of Nanomaterials and Their Biomedical Applications,” *J Mater Chem B*, vol. 6, no. 1, pp. 9–24, Jan. 2018, doi: 10.1039/C7TB01695F.

[207] C. Sanchez-Cano and M. Carril, “Recent Developments in the Design of Non-Biofouling Coatings for Nanoparticles and Surfaces,” *Int J Mol Sci*, vol. 21, no. 3, Art. no. 3, Jan. 2020, doi: 10.3390/ijms21031007.

[208] G. Huang and H. Huang, “Application of hyaluronic acid as carriers in drug delivery,” *Drug Deliv*, vol. 25, no. 1, pp. 766–772, Mar. 2018, doi: 10.1080/10717544.2018.1450910.

[209] L. A. S. Callahan *et al.*, “ECM Production of Primary Human and Bovine Chondrocytes in Hybrid PEG Hydrogels Containing Type I Collagen and

Hyaluronic Acid," *Biomacromolecules*, vol. 13, no. 5, pp. 1625–1631, May 2012, doi: 10.1021/bm3003336.

[210] E. Papakonstantinou, M. Roth, and G. Karakiulakis, "Hyaluronic acid: A key molecule in skin aging," *Dermato-Endocrinology*, vol. 4, no. 3, pp. 253–258, Jul. 2012, doi: 10.4161/derm.21923.

[211] M. W. Holmes, M. T. Bayliss, and H. Muir, "Hyaluronic acid in human articular cartilage. Age-related changes in content and size.," *Biochem J*, vol. 250, no. 2, pp. 435–441, Mar. 1988, doi: 10.1042/bj2500435.

[212] A. A. Hegewald *et al.*, "Hyaluronic acid and autologous synovial fluid induce chondrogenic differentiation of equine mesenchymal stem cells: a preliminary study," *Tissue Cell*, vol. 36, no. 6, pp. 431–438, Dec. 2004, doi: 10.1016/j.tice.2004.07.003.

[213] A. Schmaus *et al.*, "Accumulation of small hyaluronan oligosaccharides in tumour interstitial fluid correlates with lymphatic invasion and lymph node metastasis," *Br J Cancer*, vol. 111, no. 3, pp. 559–567, Jul. 2014, doi: 10.1038/bjc.2014.332.

[214] J. A. Burdick and G. D. Prestwich, "Hyaluronic Acid Hydrogels for Biomedical Applications," *Adv Mater*, vol. 23, no. 12, pp. H41–H56, Mar. 2011, doi: 10.1002/adma.201003963.

[215] M. N. Collins and C. Birkinshaw, "Hyaluronic acid based scaffolds for tissue engineering—A review," *Carbohydrate Polymers*, vol. 92, no. 2, pp. 1262–1279, Feb. 2013, doi: 10.1016/j.carbpol.2012.10.028.

[216] A. Fakhari and C. Berkland, "Applications and emerging trends of hyaluronic acid in tissue engineering, as a dermal filler and in osteoarthritis treatment," *Acta Biomaterialia*, vol. 9, no. 7, pp. 7081–7092, Jul. 2013, doi: 10.1016/j.actbio.2013.03.005.

[217] A. R. Jordan, R. R. Racine, M. J. P. Hennig, and V. B. Lokeshwar, "The Role of CD44 in Disease Pathophysiology and Targeted Treatment," *Front Immunol*, vol. 6, p. 182, 2015, doi: 10.3389/fimmu.2015.00182.

[218] E. L.-H. Leung *et al.*, "Non-small cell lung cancer cells expressing CD44 are enriched for stem cell-like properties," *PLoS One*, vol. 5, no. 11, p. e14062, Nov. 2010, doi: 10.1371/journal.pone.0014062.

[219] A. Almalik *et al.*, "Hyaluronic Acid Coated Chitosan Nanoparticles Reduced the Immunogenicity of the Formed Protein Corona," *Sci Rep*, vol. 7, no. 1, p. 10542, Sep. 2017, doi: 10.1038/s41598-017-10836-7.

[220] H. Kim, M. Shin, S. Han, W. Kwon, and S. K. Hahn, "Hyaluronic Acid Derivatives for Translational Medicines," *Biomacromolecules*, vol. 20, no. 8, pp. 2889–2903, Aug. 2019, doi: 10.1021/acs.biomac.9b00564.

[221] W. Zhong *et al.*, "Recent advantage of hyaluronic acid for anti-cancer application: a review of '3S' transition approach," *Carbohydrate Polymers*, vol. 238, p. 116204, Jun. 2020, doi: 10.1016/j.carbpol.2020.116204.

[222] M.-T. Chiang, H.-L. Wang, T.-Y. Han, Y.-K. Hsieh, J. Wang, and D.-H. Tsai, "Assembly and Detachment of Hyaluronic Acid on a Protein-Conjugated Gold Nanoparticle," *Langmuir*, vol. 36, no. 48, pp. 14782–14792, Dec. 2020, doi: 10.1021/acs.langmuir.0c02738.

[223] H. Hosseinzadeh *et al.*, "SN38 conjugated hyaluronic acid gold nanoparticles as a novel system against metastatic colon cancer cells," *Int J Pharm*, vol. 526, no. 1, pp. 339–352, Jun. 2017, doi: 10.1016/j.ijpharm.2017.04.060.

[224] X. Liu *et al.*, "Hyaluronic Acid Stabilized Iodine-Containing Nanoparticles with Au Nanoshell Coating for X-ray CT Imaging and Photothermal Therapy of Tumors," *ACS Appl Mater Interfaces*, vol. 8, no. 41, pp. 27622–27631, Oct. 2016, doi: 10.1021/acsami.6b11918.

[225] L.-S. Li, B. Ren, X. Yang, Z.-C. Cai, X.-J. Zhao, and M.-X. Zhao, "Hyaluronic Acid-Modified and Doxorubicin-Loaded Gold Nanoparticles and Evaluation of Their Bioactivity," *Pharmaceuticals*, vol. 14, no. 2, Art. no. 2, Feb. 2021, doi: 10.3390/ph14020101.

[226] O. Gotov, G. Battogtokh, and Y. T. Ko, "Docetaxel-Loaded Hyaluronic Acid–Cathepsin B-Cleavable-Peptide–Gold Nanoparticles for the Treatment of Cancer," *Mol Pharmaceutics*, vol. 15, no. 10, pp. 4668–4676, Oct. 2018, doi: 10.1021/acs.molpharmaceut.8b00640.

[227] O. Gotov, G. Battogtokh, D. Shin, and Y. T. Ko, "Hyaluronic acid-coated cisplatin conjugated gold nanoparticles for combined cancer treatment," *J Ind Eng Chem J*, vol. 65, pp. 236–243, Sep. 2018, doi: 10.1016/j.jiec.2018.04.034.

[228] P. S. Apaolaza *et al.*, "Hyaluronic acid coating of gold nanoparticles for intraocular drug delivery: Evaluation of the surface properties and effect on their distribution," *Exp Eye Res*, vol. 198, p. 108151, Sep. 2020, doi: 10.1016/j.exer.2020.108151.

[229] T. Sonntag, F. Froemel, W. D. Stamer, A. Ohlmann, R. Fuchshofer, and M. Breunig, "Distribution of Gold Nanoparticles in the Anterior Chamber of the Eye after Intracameral Injection for Glaucoma Therapy," *Pharmaceutics*, vol. 13, no. 6, Art. no. 6, Jun. 2021, doi: 10.3390/pharmaceutics13060901.

[230] C. Mendes *et al.*, "Effects of the Association between Photobiomodulation and Hyaluronic Acid Linked Gold Nanoparticles in Wound Healing," *ACS Biomater Sci Eng*, vol. 6, no. 9, pp. 5132–5144, Sep. 2020, doi: 10.1021/acsbiomaterials.0c00294.

[231] M. Egeblad, E. S. Nakasone, and Z. Werb, “Tumors as organs: complex tissues that interface with the entire organism,” *Dev Cell*, vol. 18, no. 6, pp. 884–901, Jun. 2010, doi: 10.1016/j.devcel.2010.05.012.

[232] H. Lee *et al.*, “Hyaluronate–Gold Nanoparticle/Tocilizumab Complex for the Treatment of Rheumatoid Arthritis,” *ACS Nano*, vol. 8, no. 5, pp. 4790–4798, May 2014, doi: 10.1021/nn500685h.

[233] T. L. Moore *et al.*, “Nanoparticle administration method in cell culture alters particle-cell interaction,” *Sci Rep*, vol. 9, no. 1, p. 900, Dec. 2019, doi: 10.1038/s41598-018-36954-4.

[234] J. W. Card *et al.*, “Gender Differences in Murine Airway Responsiveness and Lipopolysaccharide-Induced Inflammation,” *J Immunol*, vol. 177, no. 1, pp. 621–630, Jul. 2006.

[235] M. G. Thompson, D. S. Peiffer, M. Larson, F. Navarro, and S. K. Watkins, “FOXO3, estrogen receptor alpha, and androgen receptor impact tumor growth rate and infiltration of dendritic cell subsets differentially between male and female mice,” *Cancer Immunol Immunother*, vol. 66, no. 5, pp. 615–625, May 2017, doi: 10.1007/s00262-017-1972-4.

[236] C. R. MacRosty and M. P. Rivera, “Lung Cancer in Women: A Modern Epidemic,” *Clin Chest Med*, vol. 41, no. 1, pp. 53–65, Mar. 2020, doi: 10.1016/j.ccm.2019.10.005.

[237] A. Kellar, C. Egan, and D. Morris, “Preclinical Murine Models for Lung Cancer: Clinical Trial Applications,” *BioMed Research International*, 2015. https://www.hindawi.com/journals/bmri/2015/621324/ (accessed Jun. 27, 2019).

[238] R. Terracciano, S. Ricchetti, E. B. Butler, D. Demarchi, A. Grattoni, and C. S. Filgueira, “Abstract PO-058: Intratumoral distribution and retention of gold nanoparticles characterized by computed tomography in a non-small cell lung cancer model,” *Cancer Res*, vol. 80, no. 21 Supplement, p. PO-PO-058, Nov. 2020, doi: 10.1158/1538-7445.TUMHET2020-PO-058.

[239] R. Terracciano, B. E. Butler, D. Demarchi, A. Grattoni, and C. S. Filgueira, “Abstract 2800: The effect of surface protein adsorption on gold nanoparticle-intratumoral distribution and retention in a pre-clinical model of non-small cell lung cancer,” *Cancer Res*, vol. 81, no. 13 Supplement, pp. 2800–2800, Jul. 2021, doi: 10.1158/1538-7445.AM2021-2800.

[240] C. S. Levin, J. Kundu, A. Barhoumi, and N. J. Halas, “Nanoshell-based substrates for surface enhanced spectroscopic detection of biomolecules,” *Analyst*, vol. 134, no. 9, pp. 1745–1750, Aug. 2009, doi: 10.1039/B909080K.

[241] B. E. Brinson, J. B. Lassiter, C. S. Levin, R. Bardhan, N. Mirin, and N. J. Halas, “Nanoshells Made Easy: Improving Au Layer Growth on Nanoparticle

Surfaces," *Langmuir*, vol. 24, no. 24, pp. 14166–14171, Dec. 2008, doi: 10.1021/la802049p.

[242] S. Lal, N. K. Grady, J. Kundu, C. S. Levin, J. B. Lassiter, and N. J. Halas, "Tailoring plasmonic substrates for surface enhanced spectroscopies," *Chem Soc Rev*, vol. 37, no. 5, pp. 898–911, Apr. 2008, doi: 10.1039/B705969H.

[243] C. S. Levin, J. Kundu, B. G. Janesko, G. E. Scuseria, R. M. Raphael, and N. J. Halas, "Interactions of Ibuprofen with Hybrid Lipid Bilayers Probed by Complementary Surface-Enhanced Vibrational Spectroscopies," *J Phys Chem B*, vol. 112, no. 45, pp. 14168–14175, Nov. 2008, doi: 10.1021/jp804374e.

[244] C. S. Levin, B. G. Janesko, R. Bardhan, G. E. Scuseria, J. D. Hartgerink, and N. J. Halas, "Chain-Length-Dependent Vibrational Resonances in Alkanethiol Self-Assembled Monolayers Observed on Plasmonic Nanoparticle Substrates," *Nano Lett*, vol. 6, no. 11, pp. 2617–2621, Nov. 2006, doi: 10.1021/nl062283k.

[245] H. Wang, C. S. Levin, and N. J. Halas, "Nanosphere Arrays with Controlled Sub-10-nm Gaps as Surface-Enhanced Raman Spectroscopy Substrates," *J Am Chem Soc*, vol. 127, no. 43, pp. 14992–14993, Nov. 2005, doi: 10.1021/ja055633y.

[246] G. R. Souza, C. S. Levin, A. Hajitou, R. Pasqualini, W. Arap, and J. H. Miller, "In Vivo Detection of Gold−Imidazole Self-Assembly Complexes: NIR-SERS Signal Reporters," *Anal Chem*, vol. 78, no. 17, pp. 6232–6237, Sep. 2006, doi: 10.1021/ac060483a.

[247] "Dissociation Constants Of Organic Acids And Bases." http://www.zirchrom.com/organic.htm (accessed Sep. 24, 2021).

[248] T. Zheng, S. Bott, and Q. Huo, "Techniques for Accurate Sizing of Gold Nanoparticles Using Dynamic Light Scattering with Particular Application to Chemical and Biological Sensing Based on Aggregate Formation," *ACS Appl Mater Interfaces*, vol. 8, no. 33, pp. 21585–21594, Aug. 2016, doi: 10.1021/acsami.6b06903.

[249] W. Strober, "Trypan Blue Exclusion Test of Cell Viability," *Curr Protoc Immunol*, vol. 111, p. A3.B.1-A3.B.3, Nov. 2015, doi: 10.1002/0471142735.ima03bs111.

[250] B. B. Karakocak, J. Liang, P. Biswas, and N. Ravi, "Hyaluronate coating enhances the delivery and biocompatibility of gold nanoparticles," *Carbohydrate Polymers*, vol. 186, pp. 243–251, Apr. 2018, doi: 10.1016/j.carbpol.2018.01.046.

[251] S. Stapleton, C. Allen, M. Pintilie, and D. A. Jaffray, "Tumor perfusion imaging predicts the intra-tumoral accumulation of liposomes," *Journal of Controlled Release*, vol. 172, no. 1, pp. 351–357, Nov. 2013, doi: 10.1016/j.jconrel.2013.08.296.

[252] S. Stapleton, M. Milosevic, I. F. Tannock, C. Allen, and D. A. Jaffray, "The intra-tumoral relationship between microcirculation, interstitial fluid pressure and liposome accumulation," *Journal of Controlled Release*, vol. 211, pp. 163–170, Aug. 2015, doi: 10.1016/j.jconrel.2015.06.008.

[253] W. Wang *et al.*, "One-pot synthesis of hyaluronic acid–coated gold nanoparticles as SERS substrate for the determination of hyaluronidase activity," *Microchim Acta*, vol. 187, no. 11, p. 604, Oct. 2020, doi: 10.1007/s00604-020-04566-3.

[254] J. Ge *et al.*, "Core–Shell HA-AuNPs@SiNPs Nanoprobe for Sensitive Fluorescence Hyaluronidase Detection and Cell Imaging," *ACS Sustainable Chem Eng*, vol. 6, no. 12, pp. 16555–16562, Dec. 2018, doi: 10.1021/acssuschemeng.8b03684.

[255] K. Kim, H. Choi, E. S. Choi, M.-H. Park, and J.-H. Ryu, "Hyaluronic Acid-Coated Nanomedicine for Targeted Cancer Therapy," *Pharmaceutics*, vol. 11, no. 7, p. E301, Jun. 2019, doi: 10.3390/pharmaceutics11070301.

[256] C. S. Kumar, M. D. Raja, D. S. Sundar, M. Gover Antoniraj, and K. Ruckmani, "Hyaluronic acid co-functionalized gold nanoparticle complex for the targeted delivery of metformin in the treatment of liver cancer (HepG2 cells)," *Carbohydrate Polymers*, vol. 128, pp. 63–74, Sep. 2015, doi: 10.1016/j.carbpol.2015.04.010.

[257] W. Xu *et al.*, "A dual-targeted hyaluronic acid-gold nanorod platform with triple-stimuli responsiveness for photodynamic/photothermal therapy of breast cancer," *Acta Biomater*, vol. 83, pp. 400–413, Jan. 2019, doi: 10.1016/j.actbio.2018.11.026.

[258] E. Jeong, W. Y. Shim, and J. H. Kim, "Metabolic engineering of Pichia pastoris for production of hyaluronic acid with high molecular weight," *J Biotechnol*, vol. 185, pp. 28–36, Sep. 2014, doi: 10.1016/j.jbiotec.2014.05.018.

[259] C. Kuehl *et al.*, "Hyaluronic Acid Molecular Weight Determines Lung Clearance and Biodistribution after Instillation," *Mol Pharmaceutics*, vol. 13, no. 6, pp. 1904–1914, Jun. 2016, doi: 10.1021/acs.molpharmaceut.6b00069.

[260] G. Guelfi *et al.*, "Gold nanoparticles approach to detect chondroitin sulphate and hyaluronic acid urothelial coating," *Sci Rep*, vol. 7, no. 1, p. 10355, Sep. 2017, doi: 10.1038/s41598-017-09872-0.

[261] H. Shen, S. Shi, Z. Zhang, T. Gong, and X. Sun, "Coating Solid Lipid Nanoparticles with Hyaluronic Acid Enhances Antitumor Activity against Melanoma Stem-like Cells," *Theranostics*, vol. 5, no. 7, pp. 755–771, Apr. 2015, doi: 10.7150/thno.10804.

[262] E. Chiesa *et al.*, "On-Chip Synthesis of Hyaluronic Acid-Based Nanoparticles for Selective Inhibition of CD44+ Human Mesenchymal Stem

Cell Proliferation," *Pharmaceutics*, vol. 12, no. 3, Art. no. 3, Mar. 2020, doi: 10.3390/pharmaceutics12030260.

[263] K. Wang *et al.*, "Identification of a cancer stem cell-like side population in the HeLa human cervical carcinoma cell line," *Oncology Letters*, vol. 6, no. 6, pp. 1673–1680, Dec. 2013, doi: 10.3892/ol.2013.1607.

[264] X. Ge *et al.*, "Light-activated gold nanorod vesicles with NIR-II fluorescence and photoacoustic imaging performances for cancer theranostics," *Theranostics*, vol. 10, no. 11, pp. 4809–4821, 2020, doi: 10.7150/thno.44376.

[265] D. Harris-Birtill *et al.*, "Gold nanorod reshaping in vitro and in vivo using a continuous wave laser," *PLoS One*, vol. 12, no. 10, p. e0185990, 2017, doi: 10.1371/journal.pone.0185990.

[266] O. B. Knights and J. R. McLaughlan, "Gold Nanorods for Light-Based Lung Cancer Theranostics," *Int. J. Mol. Sci.*, vol. 19, no. 11, Oct. 2018, doi: 10.3390/ijms19113318.

[267] J. Yin *et al.*, "Nanoassembly and Multiscale Computation of Multifunctional Optical-Magnetic Nanoprobes for Tumor-Targeted Theranostics," *ACS Appl. Mater. Interfaces*, vol. 11, no. 44, pp. 41069–41081, Nov. 2019, doi: 10.1021/acsami.9b14668.

[268] K. M. Mayer *et al.*, "A Label-Free Immunoassay Based Upon Localized Surface Plasmon Resonance of Gold Nanorods," *ACS Nano*, vol. 2, no. 4, pp. 687–692, Apr. 2008, doi: 10.1021/nn7003734.

[269] K. M. Mayer, F. Hao, S. Lee, P. Nordlander, and J. H. Hafner, "A single molecule immunoassay by localized surface plasmon resonance," *Nanotechnology*, vol. 21, no. 25, p. 255503, Jun. 2010, doi: 10.1088/0957-4484/21/25/255503.

[270] S. Lee, K. M. Mayer, and J. H. Hafner, "Improved Localized Surface Plasmon Resonance Immunoassay with Gold Bipyramid Substrates," *Anal. Chem.*, vol. 81, no. 11, pp. 4450–4455, Jun. 2009, doi: 10.1021/ac900276n.

[271] D. R. Ward *et al.*, "Electromigrated Nanoscale Gaps for Surface-Enhanced Raman Spectroscopy," *Nano Lett.*, vol. 7, no. 5, pp. 1396–1400, May 2007, doi: 10.1021/nl070625w.

[272] A. T. Kelly, C. S. Filgueira, D. E. Schipper, N. J. Halas, and K. H. Whitmire, "Gold coated iron phosphide core–shell structures," *RSC Advances*, vol. 7, no. 42, pp. 25848–25854, 2017, doi: 10.1039/C7RA01195D.

[273] C. L. Nehl, H. Liao, and J. H. Hafner, "Optical Properties of Star-Shaped Gold Nanoparticles," *Nano Lett.*, vol. 6, no. 4, pp. 683–688, Apr. 2006, doi: 10.1021/nl052409y.

[274] F. Hao, C. L. Nehl, J. H. Hafner, and P. Nordlander, “Plasmon Resonances of a Gold Nanostar,” *Nano Lett.*, vol. 7, no. 3, pp. 729–732, Mar. 2007, doi: 10.1021/nl062969c.

[275] H. Wang *et al.*, “Symmetry breaking in individual plasmonic nanoparticles,” *Proc. Natl. Acad. Sci. U.S.A.*, vol. 103, no. 29, pp. 10856–10860, Jul. 2006, doi: 10.1073/pnas.0604003103.

[276] B. E. Brinson, J. B. Lassiter, C. S. Levin, R. Bardhan, N. Mirin, and N. J. Halas, “Nanoshells Made Easy: Improving Au Layer Growth on Nanoparticle Surfaces,” *Langmuir*, vol. 24, no. 24, pp. 14166–14171, Dec. 2008, doi: 10.1021/la802049p.

[277] C. L. Nehl, N. K. Grady, G. P. Goodrich, F. Tam, N. J. Halas, and J. H. Hafner, “Scattering Spectra of Single Gold Nanoshells,” *Nano Lett.*, vol. 4, no. 12, pp. 2355–2359, Dec. 2004, doi: 10.1021/nl048610a.

[278] D. Luo, M. S. Hasan, S. Shahid, B. N. Khlebtsov, M. J. Cattell, and G. B. Sukhorukov, “Gold Nanorod Mediated Chlorhexidine Microparticle Formation and Near-Infrared Light Induced Release,” *Langmuir*, vol. 33, no. 32, pp. 7982–7993, Aug. 2017, doi: 10.1021/acs.langmuir.7b01656.

[279] Y. Kwon, Y. Choi, J. Jang, S. Yoon, and J. Choi, “NIR Laser-Responsive PNIPAM and Gold Nanorod Composites for the Engineering of Thermally Reactive Drug Delivery Nanomedicine,” *Pharmaceutics*, vol. 12, no. 3, Feb. 2020, doi: 10.3390/pharmaceutics12030204.

[280] A. T. Haine and T. Niidome, “Gold Nanorods as Nanodevices for Bioimaging, Photothermal Therapeutics, and Drug Delivery,” *Chem. Pharm. Bull.*, vol. 65, no. 7, pp. 625–628, 2017, doi: 10.1248/cpb.c17-00102.

[281] J. B. Vines, J.-H. Yoon, N.-E. Ryu, D.-J. Lim, and H. Park, “Gold Nanoparticles for Photothermal Cancer Therapy,” *Front. Chem.*, vol. 7, Apr. 2019, doi: 10.3389/fchem.2019.00167.

[282] H. S. Kim and D. Y. Lee, “Near-Infrared-Responsive Cancer Photothermal and Photodynamic Therapy Using Gold Nanoparticles,” *Polymers (Basel)*, vol. 10, no. 9, p. 961, Aug. 2018, doi: 10.3390/polym10090961.

[283] H.-C. Huang, S. Barua, D. B. Kay, and K. Rege, “Simultaneous Enhancement of Photothermal Stability and Gene Delivery Efficacy of Gold Nanorods using Polyelectrolytes,” *ACS Nano*, vol. 3, no. 10, pp. 2941–2952, Oct. 2009, doi: 10.1021/nn900947a.

[284] X. Su, B. Fu, and J. Yuan, “Gold nanocluster-coated gold nanorods for simultaneously enhanced photothermal performance and stability,” *Mater. Lett.*, vol. 188, pp. 111–114, Feb. 2017, doi: 10.1016/j.matlet.2016.11.051.

[285] S. Carozza, J. Culkin, and J. van Noort, “Accuracy of the detection of binding events using 3D single particle tracking,” *BMC Biophys.*, vol. 10, pp. 1–13, Mar. 2017, doi: 10.1186/s13628-017-0035-8.

[286] Z. Ye, X. Wang, and L. Xiao, “Single-Particle Tracking with Scattering-Based Optical Microscopy,” *Anal. Chem.*, vol. 91, no. 24, pp. 15327–15334, Dec. 2019, doi: 10.1021/acs.analchem.9b02760.

[287] C. A. Wathen *et al.*, “Selective X-ray contrast enhancement of the spleen of living mice mediated by gold nanorods,” *Contrast Media Mol. Imaging*, vol. 10, no. 3, pp. 188–193, Jun. 2015, doi: 10.1002/cmmi.1617.

[288] P. Quan, W. Bu, B. Lin, X. Jiang, and L. Wang, “Correlating Ligand Density with Cellular Uptake of Gold Nanorods Revealed by X-ray Reflectivity,” *J. Nanosci. Nanotechnol.*, vol. 19, no. 12, pp. 7557–7563, Dec. 2019, doi: 10.1166/jnn.2019.16749.

[289] S. Khademi *et al.*, “Evaluation of size, morphology, concentration, and surface effect of gold nanoparticles on X-ray attenuation in computed tomography,” *Phys. Med.*, vol. 45, pp. 127–133, Jan. 2018, doi: 10.1016/j.ejmp.2017.12.001.

[290] H. Lusic and M. W. Grinstaff, “X-Ray Computed Tomography Contrast Agents,” *Chem. Rev.*, vol. 113, no. 3, Mar. 2013, doi: 10.1021/cr200358s.

[291] X. Qu, X. Li, J. Liang, Y. Wang, M. Liu, and J. Liang, “Micro-CT Imaging of RGD-Conjugated Gold Nanorods Targeting Tumor In Vivo,” *J. Nanomater.*, vol. 2016, p. e8368154, Jul. 2016, doi: 10.1155/2016/8368154.

[292] R. Terracciano *et al.*, “Effects of Surface Protein Adsorption on the Distribution and Retention of Intratumorally Administered Gold Nanoparticles,” *Pharmaceutics*, vol. 13, no. 2, p. 216, Feb. 2021, doi: 10.3390/pharmaceutics13020216.

[293] N. Hlapisi, T. E. Motaung, L. Z. Linganiso, O. S. Oluwafemi, and S. P. Songca, “Encapsulation of Gold Nanorods with Porphyrins for the Potential Treatment of Cancer and Bacterial Diseases: A Critical Review,” *Bioinorg. Chem. Appl.*, vol. 2019, p. e7147128, Apr. 2019, doi: 10.1155/2019/7147128.

[294] L. Xia *et al.*, “Nitroxide-radicals-modified gold nanorods for in vivo CT/MRI-guided photothermal cancer therapy,” *Int J Nanomedicine*, vol. 13, pp. 7123–7134, 2018, doi: 10.2147/IJN.S171804.

[295] J. Qin *et al.*, “Gold nanorods as a theranostic platform for in vitro and in vivo imaging and photothermal therapy of inflammatory macrophages,” *Nanoscale*, vol. 7, no. 33, pp. 13991–14001, Aug. 2015, doi: 10.1039/C5NR02521D.

[296] Z. Youssef *et al.*, “New Targeted Gold Nanorods for the Treatment of Glioblastoma by Photodynamic Therapy,” *J Clin Med*, vol. 8, no. 12, p. 2205, Dec. 2019, doi: 10.3390/jcm8122205.

[297] S. Her, D. A. Jaffray, and C. Allen, “Gold nanoparticles for applications in cancer radiotherapy: Mechanisms and recent advancements,” *Adv. Drug Deliv. Rev.*, vol. 109, pp. 84–101, Jan. 2017, doi: 10.1016/j.addr.2015.12.012.

[298] L. An, Y. Wang, Q. Tian, and S. Yang, “Small Gold Nanorods: Recent Advances in Synthesis, Biological Imaging, and Cancer Therapy,” *Materials*, vol. 10, no. 12, p. 1372, Dec. 2017, doi: 10.3390/ma10121372.

[299] J. G. Mehtala, D. Y. Zemlyanov, J. P. Max, N. Kadasala, S. Zhao, and A. Wei, “Citrate-Stabilized Gold Nanorods,” *Langmuir*, vol. 30, no. 46, pp. 13727–13730, Nov. 2014, doi: 10.1021/la5029542.

[300] E. Ito *et al.*, “Potential Use of Cetrimonium Bromide as an Apoptosis-Promoting Anticancer Agent for Head and Neck Cancer,” *Mol. Pharmacol.*, vol. 76, no. 5, pp. 969–983, Nov. 2009, doi: 10.1124/mol.109.055277.

[301] J. He *et al.*, “The facile removal of CTAB from the surface of gold nanorods,” *Colloids and Surfaces B: Biointerfaces*, vol. 163, pp. 140–145, Mar. 2018, doi: 10.1016/j.colsurfb.2017.12.019.

[302] A. M. Alkilany, P. K. Nagaria, C. R. Hexel, T. J. Shaw, C. J. Murphy, and M. D. Wyatt, “Cellular Uptake and Cytotoxicity of Gold Nanorods: Molecular Origin of Cytotoxicity and Surface Effects,” *Small*, vol. 5, no. 6, pp. 701–708, 2009, doi: 10.1002/smll.200801546.

[303] H. Lee *et al.*, “Surface potential microscopy of surfactant-controlled single gold nanoparticle,” *Nanotechnology*, vol. 31, no. 21, p. 215706, Mar. 2020, doi: 10.1088/1361-6528/ab73b7.

[304] Y. Zhang, D. Xu, W. Li, J. Yu, and Y. Chen, “Effect of Size, Shape, and Surface Modification on Cytotoxicity of Gold Nanoparticles to Human HEp-2 and Canine MDCK Cells,” *J. Nanomater.*, vol. 2012, pp. 1–7, 2012, doi: 10.1155/2012/375496.

[305] X. Shi, H. L. Perry, and J. D. E. T. Wilton-Ely, “Strategies for the functionalisation of gold nanorods to reduce toxicity and aid clinical translation,” *Nanotheranostics*, vol. 5, no. 2, pp. 155–165, 2021, doi: 10.7150/ntno.56432.

[306] F. Schulz, W. Friedrich, K. Hoppe, T. Vossmeyer, H. Weller, and H. Lange, “Effective PEGylation of gold nanorods,” *Nanoscale*, vol. 8, no. 13, pp. 7296–7308, Mar. 2016, doi: 10.1039/C6NR00607H.

[307] P. B. Santhosh, N. Thomas, S. Sudhakar, A. Chadha, and E. Mani, “Phospholipid stabilized gold nanorods: towards improved colloidal stability

and biocompatibility," *Phys. Chem. Chem. Phys.*, vol. 19, no. 28, pp. 18494–18504, Jul. 2017, doi: 10.1039/C7CP03403B.

[308] L. Su *et al.*, "A Fast and Efficient Replacement of CTAB with MUA on the Surface of Gold Nanorods Assisted by a Water-Immiscible Ionic Liquid," *Small*, vol. 13, no. 11, p. 1602809, 2017, doi: 10.1002/smll.201602809.

[309] B. Pan, F. Gao, L. Ao, H. Tian, R. He, and D. Cui, "Controlled self-assembly of thiol-terminated poly(amidoamine) dendrimer and gold nanoparticles," *Colloids Surf. A Physicochem. Eng. Asp.*, vol. 259, no. 1, pp. 89–94, May 2005, doi: 10.1016/j.colsurfa.2005.02.009.

[310] E. Yasun *et al.*, "BSA modification to reduce CTAB induced nonspecificity and cytotoxicity of aptamer-conjugated gold nanorods," *Nanoscale*, vol. 7, no. 22, pp. 10240–10248, May 2015, doi: 10.1039/C5NR01704A.

[311] S. Mahiuddin, O. Zech, S. Raith, D. Touraud, and W. Kunz, "Catanionic Micelles As a Model to Mimic Biological Membranes in the Presence of Anesthetic Alcohols," *Langmuir*, vol. 25, no. 21, pp. 12516–12521, Nov. 2009, doi: 10.1021/la901771x.

[312] J. Li *et al.*, "Seedless preparation of Au nanorods by hydroquinone assistant and red blood cell membrane camouflage," *RSC Adv.*, vol. 8, no. 38, pp. 21316–21325, Jun. 2018, doi: 10.1039/C8RA03795G.

[313] P. K. Jain, K. S. Lee, I. H. El-Sayed, and M. A. El-Sayed, "Calculated Absorption and Scattering Properties of Gold Nanoparticles of Different Size, Shape, and Composition: Applications in Biological Imaging and Biomedicine," *J. Phys. Chem. B*, vol. 110, no. 14, pp. 7238–7248, Apr. 2006, doi: 10.1021/jp057170o.

[314] J. R. Matthews, C. M. Payne, and J. H. Hafner, "Analysis of Phospholipid Bilayers on Gold Nanorods by Plasmon Resonance Sensing and Surface-Enhanced Raman Scattering," *Langmuir*, vol. 31, no. 36, pp. 9893–9900, Sep. 2015, doi: 10.1021/acs.langmuir.5b01203.

[315] M. L. Simeral *et al.*, "Effects of Conformational Variation on Structural Insights from Solution-Phase Surface-Enhanced Raman Spectroscopy," *J Phys Chem B*, vol. 125, no. 8, pp. 2031–2041, Mar. 2021, doi: 10.1021/acs.jpcb.0c10576.

[316] X. Ye, C. Zheng, J. Chen, Y. Gao, and C. B. Murray, "Using binary surfactant mixtures to simultaneously improve the dimensional tunability and monodispersity in the seeded growth of gold nanorods," *Nano Lett*, vol. 13, no. 2, pp. 765–771, Feb. 2013, doi: 10.1021/nl304478h.

[317] H. J. Hughes, S. M. E. Demers, A. Zhang, and J. H. Hafner, "The orientation of a membrane probe from structural analysis by enhanced Raman scattering," *Biochim. Biophys. Acta Biomembr.*, vol. 1862, no. 2, p. 183109, Feb. 2020, doi: 10.1016/j.bbamem.2019.183109.

[318] J. M. Hillegass, A. Shukla, S. A. Lathrop, M. B. MacPherson, N. K. Fukagawa, and B. T. Mossman, "Assessing nanotoxicity in cells in vitro," *Wiley Interdiscip Rev Nanomed Nanobiotechnol*, vol. 2, no. 3, pp. 219–231, May 2010, doi: 10.1002/wnan.54.

[319] S. Hussain, "Measurement of Nanoparticle-Induced Mitochondrial Membrane Potential Alterations," *Methods Mol Biol*, vol. 1894, pp. 123–131, 2019, doi: 10.1007/978-1-4939-8916-4_7.

[320] E. Pavlovich, N. Volkova, E. Yakymchuk, O. Perepelitsyna, M. Sydorenko, and A. Goltsev, "In Vitro Study of Influence of Au Nanoparticles on HT29 and SPEV Cell Lines," *Nanoscale Res Lett*, vol. 12, pp. 1–9, Aug. 2017, doi: 10.1186/s11671-017-2264-9.

[321] C. S. Levin, B. G. Janesko, R. Bardhan, G. E. Scuseria, J. D. Hartgerink, and N. J. Halas, "Chain-Length-Dependent Vibrational Resonances in Alkanethiol Self-Assembled Monolayers Observed on Plasmonic Nanoparticle Substrates," *Nano Lett.*, vol. 6, no. 11, pp. 2617–2621, Nov. 2006, doi: 10.1021/nl062283k.

[322] J. R. Matthews, C. R. Shirazinejad, G. A. Isakson, S. M. E. Demers, and J. H. Hafner, "Structural Analysis by Enhanced Raman Scattering," *Nano Lett*, vol. 17, no. 4, pp. 2172–2177, Apr. 2017, doi: 10.1021/acs.nanolett.6b04509.

[323] C. S. Levin, S. W. Bishnoi, N. K. Grady, and N. J. Halas, "Determining the Conformation of Thiolated Poly(ethylene glycol) on Au Nanoshells by Surface-Enhanced Raman Scattering Spectroscopic Assay," *Anal. Chem.*, vol. 78, no. 10, pp. 3277–3281, May 2006, doi: 10.1021/ac060041z.

[324] J. Kundu, C. S. Levin, and N. J. Halas, "Real-time monitoring of lipid transfer between vesicles and hybrid bilayers on Au nanoshells using surface enhanced Raman scattering (SERS)," *Nanoscale*, vol. 1, no. 1, pp. 114–117, Oct. 2009, doi: 10.1039/b9nr00063a.

[325] C. S. Levin, J. Kundu, B. G. Janesko, G. E. Scuseria, R. M. Raphael, and N. J. Halas, "Interactions of Ibuprofen with Hybrid Lipid Bilayers Probed by Complementary Surface-Enhanced Vibrational Spectroscopies," *J. Phys. Chem. B*, vol. 112, no. 45, pp. 14168–14175, Nov. 2008, doi: 10.1021/jp804374e.

[326] C. S. Levin, J. Kundu, A. Barhoumi, and N. J. Halas, "Nanoshell-based substrates for surface enhanced spectroscopic detection of biomolecules," *Analyst*, vol. 134, no. 9, pp. 1745–1750, Aug. 2009, doi: 10.1039/B909080K.

[327] C. Y. X. Chua, J. Ho, S. Demaria, M. Ferrari, and A. Grattoni, "Emerging Technologies for Local Cancer Treatment," *Advanced Therapeutics*, vol. 3, no. 9, p. 2000027, 2020, doi: 10.1002/adtp.202000027.

[328] H.-C. Liu *et al.*, "Potentiating Antitumor Efficacy Through Radiation and Sustained Intratumoral Delivery of Anti-CD40 and Anti-PDL1," *Int J Radiat*

Oncol Biol Phys, vol. 110, no. 2, pp. 492–506, Jun. 2021, doi: 10.1016/j.ijrobp.2020.07.2326.

[329] C. Y. X. Chua *et al.*, "Intratumoral Nanofluidic System for Enhancing Tumor Biodistribution of Agonist CD40 Antibody," *Advanced Therapeutics*, vol. 3, no. 10, p. 2000055, 2020, doi: 10.1002/adtp.202000055.

[330] C. Y. X. Chua *et al.*, "Nanofluidic drug-eluting seed for sustained intratumoral immunotherapy in triple negative breast cancer," *J Control Release*, vol. 285, pp. 23–34, Sep. 2018, doi: 10.1016/j.jconrel.2018.06.035.

[331] E. M. Cronin *et al.*, "2019 HRS/EHRA/APHRS/LAHRS expert consensus statement on catheter ablation of ventricular arrhythmias: Executive summary," *Heart Rhythm*, vol. 17, no. 1, pp. e155–e205, Jan. 2020, doi: 10.1016/j.hrthm.2019.03.014.

[332] M. Barkagan *et al.*, "Histopathological Characterization of Radiofrequency Ablation in Ventricular Scar Tissue," *JACC Clin Electrophysiol*, vol. 5, no. 8, pp. 920–931, Aug. 2019, doi: 10.1016/j.jacep.2019.05.011.

[333] B. C. Hester, A. Crawford, R. B. Kishore, K. Helmerson, N. J. Halas, and C. Levin, "Optical trapping of nanoshells," in *Optical Trapping and Optical Micromanipulation IV*, Sep. 2007, vol. 6644, p. 66441B. doi: 10.1117/12.735276.

[334] B. Hester *et al.*, "Tunable optical tweezers for wavelength-dependent measurements," *Rev Sci Instrum*, vol. 83, no. 4, p. 043114, Apr. 2012, doi: 10.1063/1.4704373.

[335] H. Wang, C. S. Levin, and N. J. Halas, "Nanosphere Arrays with Controlled Sub-10-nm Gaps as Surface-Enhanced Raman Spectroscopy Substrates," *J. Am. Chem. Soc.*, vol. 127, no. 43, pp. 14992–14993, Nov. 2005, doi: 10.1021/ja055633y.

[336] C. S. Levin, J. Kundu, B. G. Janesko, G. E. Scuseria, R. M. Raphael, and N. J. Halas, "Interactions of Ibuprofen with Hybrid Lipid Bilayers Probed by Complementary Surface-Enhanced Vibrational Spectroscopies," *J. Phys. Chem. B*, vol. 112, no. 45, pp. 14168–14175, Nov. 2008, doi: 10.1021/jp804374e.

[337] C. S. Levin, B. G. Janesko, R. Bardhan, G. E. Scuseria, J. D. Hartgerink, and N. J. Halas, "Chain-Length-Dependent Vibrational Resonances in Alkanethiol Self-Assembled Monolayers Observed on Plasmonic Nanoparticle Substrates," *Nano Lett.*, vol. 6, no. 11, pp. 2617–2621, Nov. 2006, doi: 10.1021/nl062283k.

[338] A. R. Rastinehad *et al.*, "Gold nanoshell-localized photothermal ablation of prostate tumors in a clinical pilot device study," *PNAS*, vol. 116, no. 37, pp. 18590–18596, Sep. 2019, doi: 10.1073/pnas.1906929116.

[339] J.-H. Kim, W. W. Bryan, and T. Randall Lee, “Preparation, Characterization, and Optical Properties of Gold, Silver, and Gold−Silver Alloy Nanoshells Having Silica Cores,” *Langmuir*, vol. 24, no. 19, pp. 11147–11152, Oct. 2008, doi: 10.1021/la8016497.

[340] K. A. Court, H. Yu, D. Chan, E. Blanco, A. Ziemys, and A. M. Holder, “Gold Nanorod Hydrogel Film for Laser-Induced HIPEC to Treat Peritoneal Malignancies,” *Advanced NanoBiomed Research*, vol. n/a, no. n/a, p. 2100036, doi: 10.1002/anbr.202100036.

[341] A. Bhaskaran *et al.*, “Safety, efficacy, and monitoring of bipolar radiofrequency ablation in beating myopathic human and healthy swine hearts,” *Heart Rhythm*, vol. Volume 18, no. Issue 10, pp. 1772–1779, Oct. 2021, doi: 10.1016/j.hrthm.2021.06.1189.

[342] O. J. Eick and D. Bierbaum, “Tissue temperature-controlled radiofrequency ablation,” *Pacing Clin Electrophysiol*, vol. 26, no. 3, pp. 725–730, Mar. 2003, doi: 10.1046/j.1460-9592.2003.00123.x.

[343] R. Terracciano *et al.*, “Effects of Surface Protein Adsorption on the Distribution and Retention of Intratumorally Administered Gold Nanoparticles,” *Pharmaceutics*, vol. 13, no. 2, p. 216, Feb. 2021, doi: 10.3390/pharmaceutics13020216.

[344] J. You, G. Zhang, and C. Li, “Exceptionally High Payload of Doxorubicin in Hollow Gold Nanospheres for Near-Infrared Light-Triggered Drug Release,” *ACS Nano*, vol. 4, no. 2, pp. 1033–1041, Feb. 2010, doi: 10.1021/nn901181c.

[345] R. A. Sheth *et al.*, “Doxorubicin-loaded hollow gold nanospheres for dual photothermal ablation and chemoembolization therapy,” *Cancer Nanotechnology*, vol. 11, no. 1, p. 6, Jul. 2020, doi: 10.1186/s12645-020-00062-8.

[346] S. C. Gad, K. L. Sharp, C. Montgomery, J. D. Payne, and G. P. Goodrich, “Evaluation of the toxicity of intravenous delivery of auroshell particles (gold-silica nanoshells),” *Int J Toxicol*, vol. 31, no. 6, pp. 584–594, Dec. 2012, doi: 10.1177/1091581812465969.

[347] J. A. Schwartz, “Feasibility Study of Particle-Assisted Laser Ablation of Brain Tumors in Orthotopic Canine Model,” *Cancer Res.*, vol. 69, no. 4, pp. 1659–1667, Feb. 2009, doi: 10.1158/0008-5472.CAN-08-2535.

[348] J. M. Stern, V. V. Kibanov Solomonov, E. Sazykina, J. A. Schwartz, S. C. Gad, and G. P. Goodrich, “Initial Evaluation of the Safety of Nanoshell-Directed Photothermal Therapy in the Treatment of Prostate Disease,” *Int J Toxicol*, vol. 35, no. 1, pp. 38–46, Jan. 2016, doi: 10.1177/1091581815600170.

[349] J. Curran Henson, A. Brickell, J.-W. Kim, H. Jensen, J. L. Mehta, and M. Jensen, “PEGylated Gold Nanoparticle Toxicity in Cardiomyocytes:

Assessment of Size, Concentration, and Time Dependency," *IEEE Trans Nanobioscience*, vol. PP, Feb. 2022, doi: 10.1109/TNB.2022.3154438.

[350] L. Chen *et al.*, "Drug-Loadable Calcium Alginate Hydrogel System for Use in Oral Bone Tissue Repair," *Int J Mol Sci*, vol. 18, no. 5, p. 989, May 2017, doi: 10.3390/ijms18050989.

[351] D. T. Nguyen *et al.*, "Enhanced Radiofrequency Ablation With Magnetically Directed Metallic Nanoparticles," *Circ Arrhythm Electrophysiol*, vol. 9, no. 5, May 2016, doi: 10.1161/CIRCEP.115.003820.

[352] A. d'Avila *et al.*, "New Perspectives on Catheter-Based Ablation of Ventricular Tachycardia Complicating Chagas' Disease: Experimental Evidence of the Efficacy of Near Infrared Lasers for Catheter Ablation of Chagas' VT," *J Interv Card Electrophysiol*, vol. 7, no. 1, pp. 23–38, Aug. 2002, doi: 10.1023/A:1020811915133.

[353] G. M. Vincent, J. Fox, K. Knowlton, and J. A. Dixon, "Catheter-directed neodymium:YAG laser injury of the left ventricle for arrhythmia ablation: dosimetry and hemodynamic, hematologic, and electrophysiologic effects," *Lasers Surg Med*, vol. 9, no. 5, pp. 446–453, 1989, doi: 10.1002/lsm.1900090504.

[354] D. L. Ware, P. Boor, C. Yang, A. Gowda, J. J. Grady, and M. Motamedi, "Slow Intramural Heating With Diffused Laser Light," *Circulation*, vol. 99, no. 12, pp. 1630–1636, Mar. 1999, doi: 10.1161/01.CIR.99.12.1630.

[355] D. K. Wang, M. Rahimi, and C. S. Filgueira, "Nanotechnology applications for cardiovascular disease treatment: Current and future perspectives," *Nanomedicine*, vol. 34, p. 102387, Jun. 2021, doi: 10.1016/j.nano.2021.102387.

[356] R. A. de Boer *et al.*, "Increased expression of cardiac angiotensin II type 1 (AT(1)) receptors decreases myocardial microvessel density after experimental myocardial infarction," *Cardiovasc Res*, vol. 57, no. 2, pp. 434–442, Feb. 2003, doi: 10.1016/s0008-6363(02)00704-6.

[357] L. L. Johnson and D. W. Seldin, "The role of antimyosin antibodies in acute myocardial infarction," *Semin Nucl Med*, vol. 19, no. 3, pp. 238–246, Jul. 1989, doi: 10.1016/s0001-2998(89)80016-9.

[358] S. Lehner *et al.*, "Temporal Changes in Phosphatidylserine Expression and Glucose Metabolism after Myocardial Infarction: An in Vivo Imaging Study in Mice," *Mol Imaging*, vol. 11, no. 6, p. 7290.2012.00010, Nov. 2012, doi: 10.2310/7290.2012.00010.

[359] C. Loo, A. Lowery, N. Halas, J. West, and R. Drezek, "Immunotargeted nanoshells for integrated cancer imaging and therapy," *Nano Lett*, vol. 5, no. 4, pp. 709–711, Apr. 2005, doi: 10.1021/nl050127s.

[360] A. R. Lowery, A. M. Gobin, E. S. Day, N. J. Halas, and J. L. West, "Immunonanoshells for targeted photothermal ablation of tumor cells," *Int J Nanomedicine*, vol. 1, no. 2, pp. 149–154, 2006, doi: 10.2147/nano.2006.1.2.149.

[361] D. P. O'Neal, L. R. Hirsch, N. J. Halas, J. D. Payne, and J. L. West, "Photo-thermal tumor ablation in mice using near infrared-absorbing nanoparticles," *Cancer Lett*, vol. 209, no. 2, pp. 171–176, Jun. 2004, doi: 10.1016/j.canlet.2004.02.004.

[362] W. D. James, L. R. Hirsch, J. L. West, P. D. O'Neal, and J. D. Payne, "Application of INAA to the build-up and clearance of gold nanoshells in clinical studies in mice," *J Radioanal Nucl Chem*, vol. 271, no. 2, pp. 455–459, Feb. 2007, doi: 10.1007/s10967-007-0230-1.

[363] P. Pedrosa, R. Vinhas, A. Fernandes, and P. V. Baptista, "Gold Nanotheranostics: Proof-of-Concept or Clinical Tool?," *Nanomaterials (Basel)*, vol. 5, no. 4, pp. 1853–1879, Nov. 2015, doi: 10.3390/nano5041853.

[364] J. W. Shreffler, J. E. Pullan, K. M. Dailey, S. Mallik, and A. E. Brooks, "Overcoming Hurdles in Nanoparticle Clinical Translation: The Influence of Experimental Design and Surface Modification," *International Journal of Molecular Sciences*, vol. 20, no. 23, Art. no. 23, Jan. 2019, doi: 10.3390/ijms20236056.

[365] S. Liao *et al.*, "Improvement of Gold Nanorods in Photothermal Therapy: Recent Progress and Perspective," *Frontiers in Pharmacology*, vol. 12, 2021, Accessed: Sep. 08, 2022. [Online]. Available: https://www.frontiersin.org/articles/10.3389/fphar.2021.664123

[366] M. J. Penelas *et al.*, "Importance of the Structural and Physicochemical Properties of Silica Nanoshells in the Photothermal Effect of Silica-Coated Au Nanoparticles Suspensions," *Langmuir*, vol. 38, no. 12, pp. 3876–3886, Mar. 2022, doi: 10.1021/acs.langmuir.2c00127.

Appendix A: Article Reprinting Permissions

A.1 Intratumoral Gold Nanoparticle-Enhanced CT Imaging: An in Vivo Investigation of Biodistribution and Retention

A.2 Effects of Surface Protein Adsorption on the Distribution and Retention of Intratumorally Administered Gold Nanoparticles

From: MDPI Support support@mdpi.com
Subject: Re: Reprinting permission
Date: March 21, 2022 at 10:19 AM
To: Terracciano, Rossana rossana.terracciano@polito.it

Dear Rossana,

Thank you for your email.

No special permission is required to reuse all or part of an article published by MDPI, including figures and tables. For articles published under an open access Creative Common CC BY license, any part of the article may be reused without permission, provided that the original article is clearly cited. Reuse of an article does not imply endorsement by the authors or MDPI.

Please Note: Some articles (especially Reviews) may contain figures, tables or text taken from other publications, for which MDPI does not hold the copyright or the right to re-license the published material. Please note that you should speak with the original copyright holder (usually the original publisher or authors), to enquire about whether or not this material can be re-used.

Please let us know if you have any further questions!

Kind regards,
Milica Tosic | MDPI Support Team
Email: support@mdpi.com
Visit us: https://www.mdpi.com/

MDPI Headquarters
St. Alban-Anlage 66, 4052 Basel
Office Tel. +41 (0) 61 683 77 34
Response time: Mon-Fri (9am-5pm CET)

From Rossana Terracciano (rossana.terracciano@polito.it)
Sent: Monday, March 21, 2022 03:27 PM
To: MDPI Customer Support <support@mdpi.com>
Subject: MDPI Contact Form: PhD Thesis

To whom it may concern,

My name is Rossana Terracciano and I am a contributing author of the paper titled "Effects of Surface Protein Adsorption on the Distribution and Retention of Intratumorally Administered Gold Nanoparticles" published on Feb 2021 by MDPI on the journal Pharmaceutics at the following DOI: 10.3390/pharmaceutics13020216.

I kindly ask you for reprinting permission of the paper for my Ph.D. dissertation.

Sincerely.

-Rossana Terracciano

A.3 Zonal Intratumoral Delivery of Nanoparticles Guided by Surface Functionalization

From: Langmuir EIC <eic@langmuir.acs.org>
Subject: Re: Reprinting permission
Date: Friday, November 4, 2022 at 5:47 PM
To: Terracciano, Rossana rossana.terracciano@polito.it

Thank you for your email. Prof. Walker grants you permission to reuse your paper in your dissertation as long as the ACS guidelines are followed and the original publication is appropriately cited. **I**'ve included a link to the policies below.

https://pubs.acs.org/page/copyright/journals/posting_policies.html#policies-1

ACS Journals Policies on preprints, scholarly sharing, & posting - American Chemical Society Section I: Scholarly posting & sharing policies. Reuse/Republication of the Entire Work in Theses or Collections: Authors may reuse all or part of the Submitted, Accepted or Published Work (see definitions below) in a thesis or dissertation that the Author writes and is required to submit to satisfy the criteria of degree-granting institutions. . Appropriate citation of the Published Work

Best,

Victoria Balque-Burns**, J**ournal Office Administrator**,** Langmuir on behalf of Gilbert C. Walker**,** Editor-in-Chief**,** Langmuir

From: Terracciano Rossana rossana.terracciano@polito.it
Subject: Re: Reprinting permission
Date: Wednesday, November 2, 2022 5:22 AM
To: Langmuir EIC <eic@langmuir.acs.org>

Dear Prof. Gilbert Walker,

My name is Rossana Terracciano and I am a contributing author of the paper titled "Zonal Intratumoral Delivery of Nanoparticles Guided by Surface Functionalization" published on online November 1st 2022 by ACS on Langmuir journal at the following DOI: 10.1021/acs.langmuir.2c02319.

I kindly ask you for reprinting permission of the paper for my Ph.D. dissertation.

Sincerely.

-Rossana Terracciano

A.4 Hyaluronate-Thiol Passivation Enhances Gold Nanoparticle Peritumoral Distribution When Administered Intratumorally in Lung Cancer

From: MDPI Support support@mdpi.com
Subject: Re: Reprinting permission
Date: March 21, 2022 at 10:19 AM
To: Terracciano, Rossana rossana.terracciano@polito.it

Dear Rossana,

Thank you for your email.

No special permission is required to reuse all or part of an article published by MDPI, including figures and tables. For articles published under an open access Creative Common CC BY license, any part of the article may be reused without permission, provided that the original article is clearly cited. Reuse of an article does not imply endorsement by the authors or MDPI.

Please Note: Some articles (especially Reviews) may contain figures, tables or text taken from other publications, for which MDPI does not hold the copyright or the right to re-license the published material. Please note that you should speak with the original copyright holder (usually the original publisher or authors), to enquire about whether or not this material can be re-used.

Please let us know if you have any further questions!

Kind regards,
Milica Tosic | MDPI Support Team
Email: support@mdpi.com
Visit us: https://www.mdpi.com/

MDPI Headquarters
St. Alban-Anlage 66, 4052 Basel
Office Tel. +41 (0) 61 683 77 34
Response time: Mon-Fri (9am-5pm CET)

From Rossana Terracciano (rossana.terracciano@polito.it)
Sent: Monday, March 21, 2022 03:36 PM
To: MDPI Customer Support <support@mdpi.com>
Subject: MDPI Contact Form: PhD Thesis

To whom it may concern,

My name is Rossana Terracciano and I am a contributing author of the paper titled " Hyaluronate-Thiol Passivation Enhances Gold Nanoparticle Peritumoral Distribution When Administered Intratumorally in Lung Cancer" published on Oct 2021 by MDPI on the journal of Biomedicines at the following DOI: 10.3390/biomedicines9111561.

I kindly ask you for reprinting permission of the paper for my Ph.D. dissertation.

Sincerely.

-Rossana Terracciano

A.5 Improvements in Gold Nanorod Biocompatibility with Sodium Dodecyl Sulfate Stabilization

From: MDPI Support support@mdpi.com
Subject: Re: Reprinting permission
Date: March 21, 2022 at 10:19 AM
To: Terracciano, Rossana rossana.terracciano@polito.it

Dear Rossana,

Thank you for your email.

No special permission is required to reuse all or part of an article published by MDPI, including figures and tables. For articles published under an open access Creative Common CC BY license, any part of the article may be reused without permission, provided that the original article is clearly cited. Reuse of an article does not imply endorsement by the authors or MDPI.

Please Note: Some articles (especially Reviews) may contain figures, tables or text taken from other publications, for which MDPI does not hold the copyright or the right to re-license the published material. Please note that you should speak with the original copyright holder (usually the original publisher or authors), to enquire about whether or not this material can be re-used.

Please let us know if you have any further questions!

Kind regards,
Milica Tosic | MDPI Support Team
Email: support@mdpi.com
Visit us: https://www.mdpi.com/

MDPI Headquarters
St. Alban-Anlage 66, 4052 Basel
Office Tel. +41 (0) 61 683 77 34
Response time: Mon-Fri (9am-5pm CET)

From Rossana Terracciano (rossana.terracciano@polito.it)
Sent: Monday, March 21, 2022 03:27 PM
To: MDPI Customer Support <support@mdpi.com>
Subject: MDPI Contact Form: PhD Thesis

To whom it may concern,

My name is Rossana Terracciano and I am a contributing author of the paper titled "Improvements in Gold Nanorod Biocompatibility with Sodium Dodecyl Sulfate Stabilization" published on Aug 2021 by MDPI on the journal of Nanotheranistics at the following DOI: 10.3390/jnt2030010.

I kindly ask you for reprinting permission of the paper for my Ph.D. dissertation.

Sincerely.

-Rossana Terracciano

A.6 Near-Infrared Sensitive Nanoparticle Mediated Photothermal Ablation of Ventricular Myocardium

From: Permissions Helpdesk <permissionshelpdesk@elsevier.com>
Date: Tuesday, May 24, 2022 at 7:42 PM
To: Terracciano Rossana <rossana.terracciano@polito.it>
Subject: Re: Reprinting permission, HRTHM [220523-024388]

Dear Terracciano Rossana

As the author of the article, you are allowed to use it in your thesis and no formal permission is required.

Please go ahead and use it and ensure to give full credit to the original source.

Kind regards,

Roopa Lingayath
Senior Copyrights Coordinator
ELSEVIER | HCM - Health Content Management

Visit Elsevier Permissions

From: Terracciano Rossana <rossana.terracciano@polito.it>
Sent: Friday, May 20, 2022 12:33 PM
To: Journal <Journal@hrsonline.org>
Subject: Reprinting permission

To whom it may concern,

My name is Rossana Terracciano and I am a contributing author of the paper titled " Near-Infrared Sensitive Nanoparticle Mediated Photothermal Ablation of Ventricular Myocardium" published on online 11 May 2022 by Heart Rhythm Journal at the following DOI: 10.1016/j.hrthm.2022.05.006.

I kindly ask you for reprinting permission of the paper for my Ph.D. dissertation.

Sincerely.

-Rossana Terracciano